# Deep Dielectric-Based Water Saturation in Freshwater and Mixed Salinity Environments

*Dr. Ping Zhang, Dr. Wael Abdallah, Dr. Gong Li Wang and Dr. Shouxiang M. Ma*

**Abstract /**

A low frequency, i.e., KHz, resistivity-based method for water saturation ($S_w$) evaluation is the desired method in the industry due to its deep depth of investigation (DOI) — up to 8 ft. The method becomes unreliable if the formation water is fresh or has mixed salinity ($SAL_w$). Dielectric permittivity and conductivity dispersion have been used to estimate the $S_w$ and $SAL_w$. The current dielectric dispersion tools, however, have a shallow DOI due to their high measurement frequency up to GHz, which most likely confines the measurements within the near wellbore mud filtrate invaded zones. It is desirable to evaluate the possibility of developing a deeper dielectric permittivity-based $S_w$ measurement for various petrophysical applications.

In this study, effective medium model simulations were conducted to study different electromagnetic (EM) induced polarization effects and their relationships to rock petrophysical properties. Special attention is placed on the complex conductivity at 2 MHz due to the availability of current logging tools. It is known that the complex dielectric saturation interpretation at the MHz range is quite difficult from physics principles, especially when only a single frequency signal is used. Therefore, our study is focused on selected key parameters: water filled porosity ($\phi_w$), $SAL_w$ and grain shape, and their effects on the modeled formation conductivity and permittivity.

To simulate field logs, some of the petrophysical parameters previously mentioned are generated randomly within predefined expected ranges. Formation conductivity and permittivity are then calculated using our petrophysical model. The calculated data are mixed with random noises of 10% to make them more realistic — like downhole logs. The synthetic conductivity and permittivity logs are used as inputs in a neural network application to explore possible correlations with $\phi_w$. It was found that while the conductivity and permittivity logs are generated from randomly selected petrophysical parameters, they are highly correlated with $\phi_w$. If new conductivity and permittivity logs are generated with different petrophysical parameters, the correlations defined before can be used to predict $\phi_w$ in the new data sets.

We also found that for freshwater environments, the conductivity has much lower correlation with $\phi_w$ than the one derived from the permittivity. The correlations are always improved when both conductivity and permittivity were used. This exercise serves as a proof of concept, which opens an opportunity for field data applications.

Field logs confirm the findings in the model simulations. Two propagation resistivity logs measured at 2 MHz are processed to calculate formation conductivity and permittivity. Using independently estimated $\phi_w$, a model was trained using a neural network for one of the logs. Excellent correlation between formation conductivity, permittivity, and $\phi_w$ is observed for the trained model. This neural network generated model can be used to predict water content from other logs collected from different wells with a coefficient of correlation ($R$) up to 96%.

Best practices are provided on the performance of using conductivity and permittivity to predict $\phi_w$. These include how to effectively train the neural network correlation models, and general applications of the trained model for logs from different fields. With the established methodology, deep dielectric-based $S_w$ in freshwater and mixed $SAL_w$ environments is obtained for enhanced formation evaluation, well placement, and saturation monitoring.

## Introduction

A resistivity log was the first downhole log ever run almost 100 years ago — in 1927 — for resources evaluation. This is still the most popular and widely used measurement in formation evaluation, well placement, and reservoir saturation monitoring. To interpret resistivity logs for reservoir saturation requires detailed knowledge of formation water salinity ($SAL_w$) as well as rock electric properties. The latter is normally measured from core samples. The former, however, could be hard to know if we have a mixed $SAL_w$, a common scenario after water injection in developed reservoirs. In addition, a fundamental assumption for the underling resistivity method is based on

large resistivity contrast between oil and water. For a freshwater environment, the resistivity difference between oil and water is greatly decreased, leading to an industrywide petrophysical challenge of freshwater environment petrophysics.

Another important rock electric property is permittivity, which can be estimated from induction data[1, 2]. In an effort to incorporate permittivity into petrophysical interpretations, an approach that specially targets resistivity and permittivity dispersion properties was proposed in the high frequency range from 10 MHz to GHz[3-6]. Commercial logging devices based on this approach have been built and successfully used in freshwater environments[7]. A major limitation for such applications, due to very high frequencies, is their shallow depth of investigation (DOI), only a few inches from the wellbore into the formation.

Current electromagnetic (EM) tools are operating at vastly different frequencies. Induction-type resistivity measurements operate in the KHz range to hundreds of KHz and propagation-type resistivity measurements operate from hundreds of KHz to MHz. Both have much deeper DOI than the GHz dielectric tools. It is therefore desirable to evaluate a possibility of developing a deep dielectric permittivity-based method for petrophysical applications.

Recently, broadband petrophysical models have been developed for clean reservoirs[8] as well as shaly sand reservoirs[6]. These models allow comprehensive studies of relationships between formation permittivity and conductivity with a number of petrophysical parameters, such as water-filled porosity ($\phi_w$), $SAL_w$, and grain shape. Based on extensive simulation results, substantial knowledge regarding sensitivity and inner dependence of the permittivity on $\phi_w$, $SAL_w$, and grain geometry are achieved. Special attention is placed on the model simulations at 2 MHz due to the availability of current logging tools. The main focus of the simulations at 2 MHz is beyond understanding the inner dependence of the permittivity on other parameters, to generate field-like logs, so that a new method can be developed to explore possible solutions of using the permittivity to derive reservoir saturation.

The neural network is selected to explore a possibility of using the permittivity to predict $\phi_w$. The initial results, after extensive model calculations on different synthetic logs, are very promising. It seems that a strong correlation between permittivity and $\phi_w$ makes it possible to estimate water saturation ($S_w$) using the measured permittivity data. Testing field logs from two different wells further confirm this discovery.

## Model Simulations

The broadband EM model that accounts for two key polarization mechanisms present in oil field formations: The polarization on the interfaces between the conductive fluid and nonconductive mineral grains, and the polarization of the electrical double layer present on charged grains. As detailed by Seleznev et al. (2017)[8], the model is represented as a collection of spherical inclusions possessing surface charges and spheroidal inclusion without surface charges dispersed in a conductive brine phase, Fig. 1. In addition, the model assumes that the rock is completely water filled, $S_w = 1$; therefore, $\phi_w$ is formation porosity, $\phi$.

The model presented in Fig. 1 is most applicable to formations containing grains with a moderate amount of surface charges, e.g., quartz and kaolinite. Quartz grains often have a near-spherical shape and can be reasonably approximated by charged spheres. Variations in the rock tortuosity, or cementation exponent ($m$), is modeled via the addition of noncharged ellipsoidal inclusions[8]. The model can be used to calculate rock permittivity and conductivity from pre-defined $\phi_w$, $SAL_w$, $m$, and temperature ($T$).

### Dispersion Responses

The calculation was first focused on the dispersion effects of permittivity with $SAL_w$, $\phi_w$, $m$, and grain size. Table 1 lists the parameter values used for the calculations. The frequency used to compute dispersion responses is from $10^2$ Hz to $10^9$ Hz. Figure 2 shows the permittivity variations for different $SAL_w$ levels. Each curve represents one $SAL_w$. The values of the remaining parameters are listed on top of the figure, where $a$ is the grain size. Strong dispersions are observed for frequencies below $10^5$ Hz. Lower $SAL_w$ gives stronger dispersions than the higher $SAL_w$. At frequencies above 1 MHz, the dispersions are greatly reduced, but still clearly visible. Based on these results, it is apparent that permittivity has a strong dependence on $SAL_w$ below $10^4$ Hz, especially as freshwater can substantially impact the dispersion

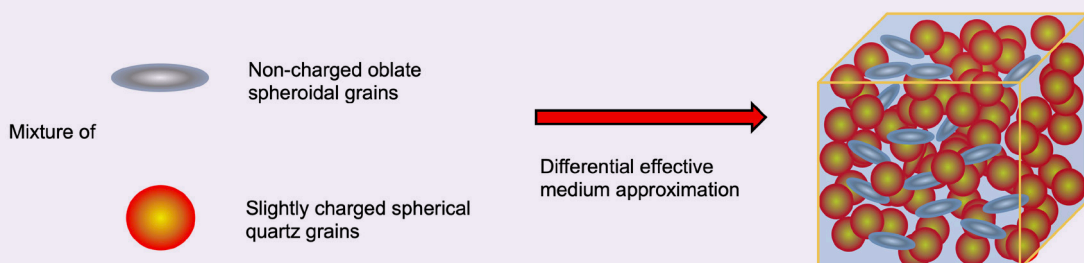**Fig. 1** *Graphical representation of the wideband model.*

**Table 1** *The parameters used for sensitivity studies of permittivity dispersion.*

| Salinity ($SAL_w$) (ppk) | Water-Filled Porosity ($\phi_w$) | Cementation Exponent ($m$) | Radius of Charged Spheres ($a$) (*um*) |
|---|---|---|---|
| 1, 5, 10, 60, 100 | 0.1, 0.2, 0.3, 0.4, 0.5 | 1.5, 1.6, 1.7, 1.8, 2.1 | 1, 5, 10, 50, 100 |

characteristic of permittivity.

The dispersion effect due to $\phi_w$ is depicted in Fig. 3. Strong dispersions are observed for frequencies less than $10^4$ Hz. In addition, the dispersion curves are clearly separated for each $\phi_w$ for the entire frequency range, meaning that permittivity has excellent sensitivity for the $\phi_w$.

Figure 4 shows the dispersions for different rock pore geometries, represented by $m$. Once again, strong dispersions are observed for frequencies less than $10^4$ Hz. At lower frequencies, larger permittivity values are observed for smaller $m$. At frequencies above $10^4$ Hz, the dependencies are reversed. It seems that the permittivity is more sensitive to $m$ at high frequencies. The last dispersion plot is related with grain sizes, Fig. 5. Although strong dispersions are shown below $10^4$ Hz,

the permittivity has no sensitivity to the grain size for frequencies above $10^4$ Hz.

### Permittivity Responses at 2 MHz

From the dispersion studies (Figs. 2 to 5), it can be observed that at frequencies above the MHz range, the permittivity has greatly reduced dispersion and relatively weak dependence on all modeled parameters except $\phi_w$. Consequently, more studies of extracting $S_w$ from permittivity were carried out at the single frequency of 2 MHz, a frequency used in all logging while drilling resistivity tools.

Figure 6 shows permittivity variations as a function of $\phi_w$ for five salinities, at two temperatures, 100 °F and 400 °F. Ideally, we would like to see strong correlations between permittivity and $\phi_w$, so that $S_w$ can be derived.

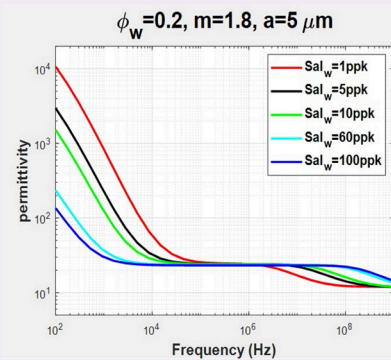**Fig. 2** *The effect of different* $SAL_w$ *levels on the permittivity dispersion.*



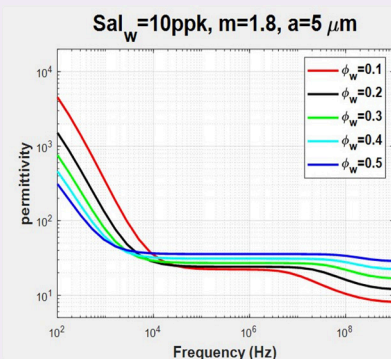**Fig. 4** *The effect of m on the permittivity dispersion.*



**Fig. 3** *The effect of* $\phi_w$ *on the permittivity dispersion.*
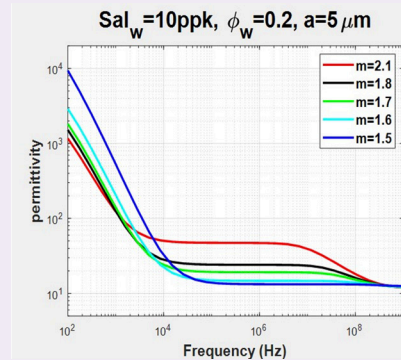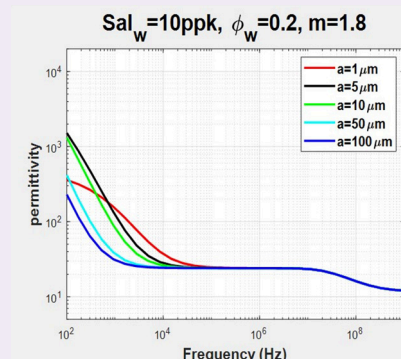


**Fig. 5** *The effect of grain size on the permittivity dispersion.*

At the high temperature, 400 °F, a very well confined relationship is observed regardless of the $SAL_w$ values. At the low temperature, 100 °F, the correlation is not confined. Different $SAL_w$ value causes noticeable deviations on the curves. In addition, the curves at 100 °F are very different from the ones at 400 °F, indicating that it is not possible to predict $\phi_w$ only from measured permittivity without a prior knowledge of $SAL_w$ and $T$.

Figure 7 shows similar plots but with different $m$ values. It is even more obvious in this case that the correlations between permittivity and $\phi_w$ are more complicated with variable $m$. Figure 8 shows impacts from grain size. Clearly, the relationship between permittivity and $\phi_w$ does not depend on grain size, although it is still affected by temperature.

## Predicting Water Filled Porosity

The simulation results of Figs. 6 to 8 clearly show that permittivity at 2 MHz has a strong sensitivity to $\phi_w$. The inter-correlations between them may provide a possibility of estimating $\phi_w$ from measured permittivity. $SAL_w$, $m$, and $T$ have huge influences on the correlations, so that a normal regression method cannot be applied to estimate $\phi_w$ unless we have prior knowledge of those reservoir parameters. While $m$ can normally be obtained through laboratory measurements on core samples, reservoir temperature can also be measured on-site. It is very difficult to obtain formation $SAL_w$[9], especially if a reservoir is under waterflooding.

This challenge may open an opportunity of using a machine learning method. In particular, using a neural network to explore the correlations between permittivity and $\phi_w$ under mixed $SAL_w$ conditions, and with different reservoir rock cementation exponents and reservoir temperatures.

### Neural Networks

Artificial neural networks, or simply neural networks, are a common technique among the machine learning tools to solve and analyze complex problems — classification and regression. The concept of a neural network, which has found useful applications in function regression, is an adaptation of interconnection of brain neurons to machine, for the nonlinear mapping of input to output[10]. The neural network architecture, consisting of an input layer, hidden layer, activation function and output layer, controls how the nonlinear mapping of input to output works. The nonlinear mapping of the predictors and target is established by training the neural network. This step is considered an optimization problem with an objective function defined by the standard least-squares method. The optimum neural network parameters to realize the best performance are evaluated with two statistic parameters: the coefficient of correlation ($R$), and mean square error (MSE):

$$R = \frac{Covariance(X_m, X_p)}{std(X_m) \times std(X_p)} \qquad 1$$

$$MSE = \frac{1}{n}\sum_1^n (X_m - X_p)^2 \qquad 2$$

The regression values, $R$, measure the correlation between model outputs, $X_p$, and targets, $X_m$. A regression

**Fig. 6** *The effect of* SAL_w *on the relationships between* $\phi_w$ *and permittivity, where T = 100 °F (left panel) and 400 °F (right panel).*
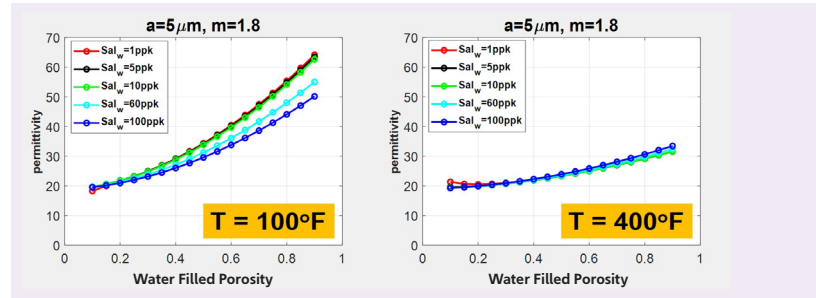
**Fig. 7** *The effect of m on relationships between* $\phi_w$ *and permittivity, where T = 100 °F (left panel) and 400 °F (right panel).*
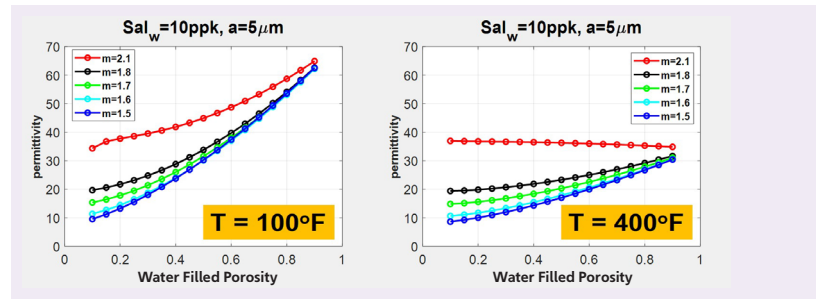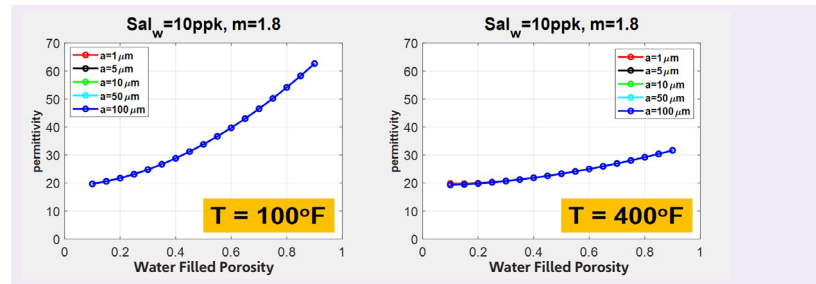
**Fig. 8** *The effect of grain size on relationships between* $\phi_w$ *and permittivity, where T = 100 °F (left panel) and 400 °F (right panel).*

value of 1 means a perfect correlation, and 0 is a random relationship. The MSE is the average squared difference between the outputs and targets. Lower values are better. Zero means perfect predictions, no errors.

### Generating Synthetic Logs

The purpose of generating synthetic logs is to explore a possibility of using measured permittivity to estimate $\phi_w$. Based on the simulation results, for a clean reservoir, formation conductivity and permittivity depend on $\phi_w$, $SAL_w$, $m$, grain size, and $T$. At 2 MHz, permittivity is not sensitive to grain size, so for all synthetic logs, the grain size is fixed at 10 micrometers. The synthetic logs are generated within a depth range of 1,000 ft to 2,000

ft, with a 0.5 ft sampling rate. To closely represent field logs, both $\phi_w$ and $SAL_w$ are generated using a random number generator within predetermined numerical ranges. The $m$ and $T$, on the other hand, are fixed at a few predefined values.

Table 2 shows the details of the parameters used to calculate the synthetic formation conductivity and permittivity logs.

An example of the synthetic logs is represented in Fig. 9. Track 1 is $\phi_w$, randomly generated within a range of 0.1 to 0.9. Track 2 is $SAL_w$, randomly generated within 1 part per thousand (ppk) to 150 ppk. Tracks 3 and 4 are the calculated formation conductivity and permittivity for $m = 2$ and $T = 100$ °F, respectively. Then, the calculated conductivity and permittivity are added with 10% random noises.

Figure 10 shows the final logs used for the neural network simulations.

### Predicting the $\phi_w$ for Different $m$

The purpose of generating synthetic logs is to explore the possibilities of using a neural network to estimate $\phi_w$ from permittivity. Considering that other parameters ($m$ and $T$) are also closely related to permittivity, it is our hope that the neural network, as a general statistic approach, can address this issue.

First, we examine how $m$ affects the neural network predictions with the following steps:

1. The $\phi_w$ and $SAL_w$ in Fig. 9, together with $m = 1.5$ and $T = 100$ °F, are used to calculate permittivity and conductivity logs. The calculated logs are used as inputs and $\phi_w$ as the target for a three-layer 15 cells' neural network to train a model. The trained model, if successful, can predict the $\phi_w$ from the input logs.

2. Calculating new permittivity and conductivity logs with the same parameter setups as step 1, except with $m = 1.7$ and $m = 2$. Then the trained model in step 1 is applied to these newly calculated logs to predict $\phi_w$. The predictions are compared with the true ones to assess how well the trained model performs on the new logs.

The regression value and MSE, given in Eqns. 1 and 2, are used to assess the quality of the model predictions. Figure 11 shows the results for the trained model and the model predictions. Figure 11a shows the trained model outlined in step 1. In this case, the permittivity and conductivity logs are able to give almost perfect



**Fig. 9** *Synthetic logs: Track 1 $\phi_w$ randomly generated within 0.1 to 0.9; track 2 $SAL_w$ randomly generated within 1 to 150 ppk; tracks 3 and 4 are the calculated formation conductivity and permittivity for m = 2 and T = 100 °F, respectively.*
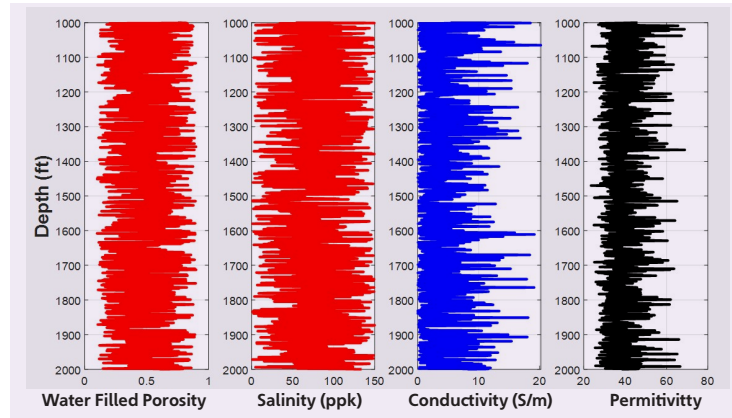
predictions of $\phi_w$ ($R = 0.99$). In other words, if a field condition can be represented by the model parameters, then the measured permittivity and conductivity logs can be used to estimate $\phi_w$, even though we do not have the knowledge of formation $SAL_w$ (randomly generated within 1 ppk to 150 ppk).

Figures 11b and 11c are the outcomes of step 2, which tries to answer whether the model defined in step 1 is still valid for different $m$ values. If $m$ is increased from 1.5 to 1.7, the estimated $\phi_w$ are mostly correct, except the slightly upward bias at the lower end of porosity, Fig. 11b. In a practical sense, the model trained with $m = 1.5$ can be used to estimate $\phi_w$ for $m = 1.7$. If a further increase of $m$ to 2, the accuracy of the prediction is greatly reduced, Fig. 11c. In this case, more than half of the $\phi_w$ are overly estimated.

### Predicting the $\phi_w$ for Different Temperatures

Reservoir temperature can also impact permittivity and conductivity measurements. Therefore, it is logical to test the influences of the temperatures on the model predictions, using the following steps:

1. The $\phi_w$ and $SAL_w$ in Fig. 9, together with $m = 1.5$ and $T = 100$ °F, are used to calculate the permittivity and conductivity logs. The calculated logs are used as inputs and the $\phi_w$ as the target for a three-layer

**Table 2** *The parameters used for calculating the synthetic conductive and permittivity logs.*

| Name | Depth (ft) | Water-Filled Porosity ($\phi_w$) | Salinity (ppk) | Cementation Exponent ($m$) | Radius of Charged Spheres ($um$) | Temperature (°F) | Frequency ($MHz$) |
|---|---|---|---|---|---|---|---|
| Range | 1,000 to 2,000 | 0.1 to 0.9 | 1 to 150 | 1.5, 1.7, 2.0 | 10 | 100, 200, 300, 400 | 2 |
| Sampling rate | 0.5 | Random | Random | Fixed | Fixed | Fixed | Fixed |

**Fig. 10**  *The 10% random noises are added on the conductivity and permittivity logs in Fig. 9. These are the final logs used in the neural network simulations.*
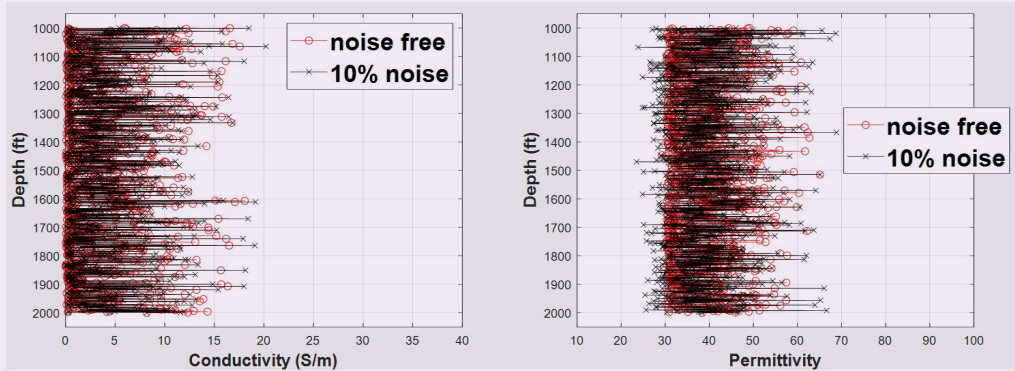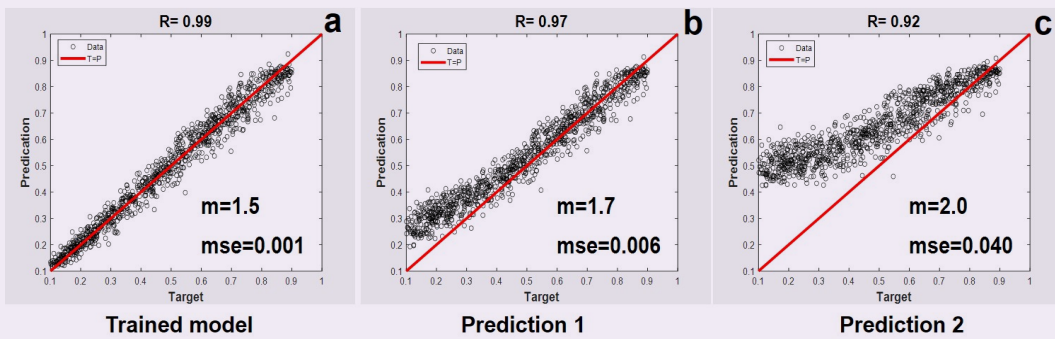


**Fig. 11**  *The model training and predictions: (a) The trained model for m = 1.5, (b) the prediction for m = 1.7 using the trained model in (a), and (c) the prediction for m = 2 using the trained model in (a).*



15 cell neural network to train a model. The trained model, if successful, can be used to predict the $\phi_w$.

2. Calculating new permittivity and conductivity logs with the same parameter setups as step 1, except with $T = 200$ °F, 300 °F, and 400 °F. Then, the trained model in step 1 is applied to these newly calculated logs to predict $\phi_w$. The predictions are compared with the true ones to assess how well the trained model performs on the new logs.

The results are presented in Fig. 12. As expected, the trained model is able to predict the $\phi_w$ accurately, Fig. 12a. Applying the same model to the permittivity and conductivity logs calculated with different temperatures do not yield satisfactory estimations. At 200 °F, the predictions are still reasonable with $R = 0.8$, Fig. 12b; however, for 300 °F and 400 °F, very poor estimations are observed, Figs. 12c and 12d.

**Predicting $\phi_w$ under Low $SAL_w$ Condition**

So far, all the model trainings and predictions are performed for salinities randomly generated between 1 ppk to 150 ppk, a very wide range. Next, we proceed to examine the performance with low $SAL_w$ or freshwater conditions.

To this end, the permittivity and conductivity logs are re-calculated with randomly picked salinities between 1 ppk to 50 ppk. The other parameters are kept the same as the previous simulations. For this exercise, we focus on the input parameters with the following steps:

1. Using both the permittivity and conductivity logs as inputs and the $\phi_w$ as a target to train a model.

2. Using the permittivity log as input and the $\phi_w$ as a target to train a model.

3. Using the conductivity log as input and the $\phi_w$ as a target to train a model.

All the permittivity and conductivity logs are calculated with $m = 1.5$ and $T = 100$ °F.

Figure 13 shows the model training results for all three steps. Figure 13a shows the trained model using both permittivity and conductivity logs. Clearly, the $\phi_w$ can be perfectly predicted in this case. Figure 13b shows the model trained with only the permittivity log. The predictions are almost similar to Fig. 13a; it seems that the permittivity log plays a critical role in the predictions. Figure 13c shows the model trained with the conductivity log only; very poor predictions are observed.

**Fig. 12** *The model training and predictions: (a) The trained model for T = 100 °F, (b) the prediction for T = 200 °F using the trained model in (a), (c) the prediction for T = 300 °F using the trained model in (a), and (d) the prediction for T = 400 °F using the trained model in (a).*
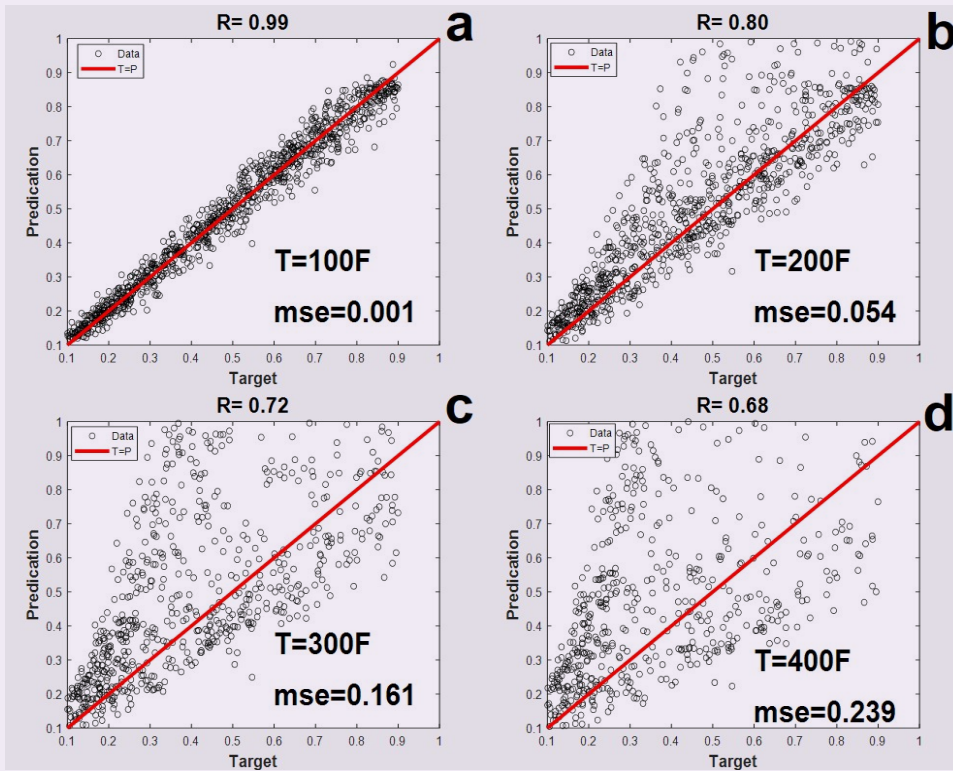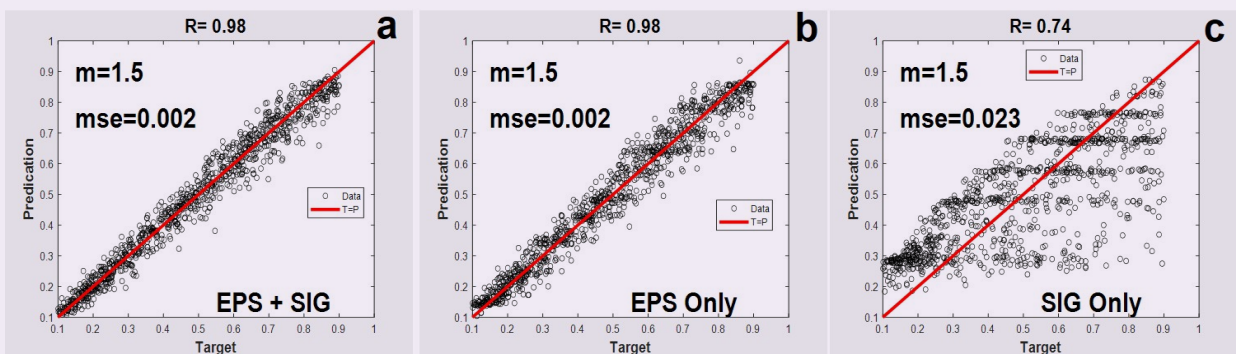


**Fig. 13** *The model training with different inputs: (a) The trained model using both the permittivity and conductivity logs, (b) the trained model using the permittivity log only, and (c) the trained model using the conductivity log only.*



This is not surprising, considering that the conductivity logs have low sensitivity for fluids with low $SAL_w$. In other words, conductive logs cannot give reliable saturation estimations for a reservoir containing mostly freshwater.

**Predicting $\phi_w$ at High $SAL_w$ Condition**

The same model training exercises are repeated with high $SAL_w$ conditions. Following the same steps as the previous section, but with randomly generated salinities within 60 ppk to 150 ppk. Figure 14 shows the results of the model trainings. As expected, excellent predictions are achieved for the first two steps. Good predictions are also observed for step 3. This is mainly due to the fact that conductivity logs are sensitive for fluids with high $SAL_w$; however, adding permittivity logs can greatly improve the predictions of the trained models.

**Field Examples**

To test the procedures previously outlined, field logs from

**Fig. 14** *The model training with different inputs: (a) The trained model using both the permittivity and conductivity logs, (b) the trained model using the permittivity log only, and (c) the trained model using the conductivity log only.*
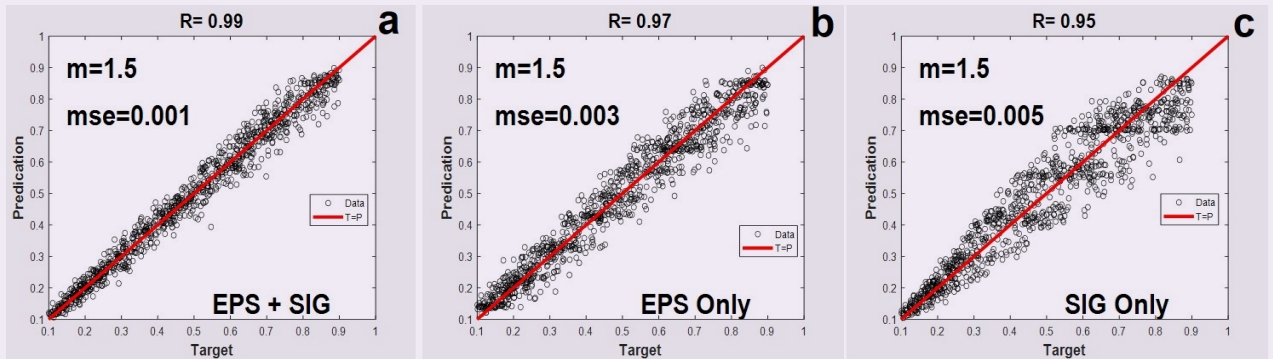
two different wells were selected. The logs from Well-A were used to train a model, and the logs from Well-B were used to validate the trained model. Conventional logs (resistivity, gamma, density, and nuclear) were collected for both wells. The resistivity logs were measured at two frequencies: 400 KHz and 2 MHz; 2 MHz logs are used for model training. The formation rocks are mostly calcite and dolomite. Conventional petrophysical interpretations were carried out to estimate the porosity and saturation.

Both formation permittivity and conductivity were calculated from the measured resistivity logs using an inversion method[2]. The model training process for logs from Well-A consists of the following steps:

1.  Use the calculated permittivity and conductivity logs as inputs and the product of porosity and saturation $\phi_w$ as a target. Both the porosity and saturation come from conventional petrophysical interpretations.

2.  Both inputs and the target are fed into a neural network to train a model. The neural network contains three layers and 15 cells.

3.  The regression and data fits are calculated to assess the trained model.

Figure 15 shows the trained model, Fig. 15a, and data fits, Fig. 15b. The model is trained exceptionally well, as evidenced by the high regression number, $R = 0.998$, and very small MSE, $MSE = 0.026$. Figure 15b presents details of the data fits. The red symbols are the $\phi_w$ from the petrophysical interpretations (denoted as true) and the black symbols are the outputs from the model training, i.e., predicted $\phi_w$. A total of 1,600 data points are used for model training, almost every data point is predicted well. It proves that the formation permittivity and conductivity can be used to predict the $\phi_w$.

The trained model from logs in Well-A are applied on logs from Well-B for validation. This time no model training is required. Instead, both the calculated permittivity and conductivity logs from Well-B are used as inputs for the trained model and the outputs (predicted $\phi_w$) are compared with the ones based on conventional

petrophysical interpretations.

Figure 16 shows both model validations, Fig. 16a, and data fits, Fig. 16b. Excellent regression is achieved, $R = 0.967$, for model validation. It means that the trained model from Well-A works almost equally well on Well-B. As a result, the predicted $\phi_w$ (black) fits very well with the ones based on petrophysical interpretations (red). In

**Fig. 15** *The trained model and data fit: (a) The trained model using both the permittivity and conductivity logs, and (b) comparing $\phi_w$ from model prediction (black) and the ones from conventional interpretation (red).*
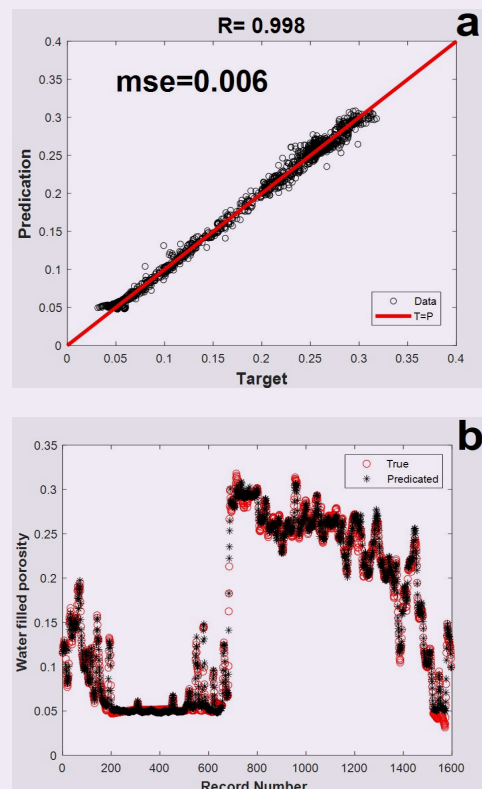
addition, there are two areas where the petrophysical interpretations give almost zero $\phi_w$ (marked by red circles in Fig. 16b). The model predicted values are around 5%, which seem more reasonable.

## Discussion and Conclusions

High frequency dielectric data (10s of MHz to GHz) have been routinely used to estimate formation $\phi_w$. Due to its shallow DOI, the applications are limited. In this article, we explore a possibility of using lower frequency permittivity and conductivity logs to accurately predict the $\phi_w$.

Extensive model simulations indicate that for a clean reservoir, the permittivity strongly depends on $\phi_w$, $SAL_w$, $m$, and $T$. At 2 MHz, the permittivity is very sensitive to the $\phi_w$, $SAL_w$, $m$, and $T$. All have an impact on the permittivity, so that it is not possible to build simple linear/nonlinear relationships between the permittivity and the $\phi_w$. As a result, a neural network is used to explore a statistic model, which can be used to predict the $\phi_w$ for different $m$ and $T$.

Synthetic logs are generated for a wide range $\phi_w$ and $SAL_w$. The $m$ and $T$ are limited to a few commonly used values. It turns out that with the knowledge of $m$ and $T$, statistic models can be built to accurately predict the $\phi_w$ from the permittivity and conductivity logs. If the models used on the logs are with different $m$ and $T$, the prediction results are not very satisfactory. In particular, if a model trained with $m = 1.5$ is used on the logs calculated with $m = 1.7$, the results are still good. For $m = 2.0$, however, the predictions are less satisfactory, with more than 50% of the data points overly predicted.

Similar trends were observed for temperature variations. If a model trained for $T = 100$ °F, a reasonable prediction can be expected for $T = 200$ °F. Very poor results are observed for $T = 300$ °F and 400 °F. It seems that to predict the $\phi_w$ using the permittivity and conductivity logs, we need to have reasonable knowledge about $m$ and the borehole temperature. In practical applications, $m$ can be acquired through laboratory measurements on core samples; where the borehole temperature is normally a routine measured parameter. That means the neural network approach may be very useful in field data interpretations.

Another interesting discovery is that the permittivity is very sensitive to the $\phi_w$ in a wide $SAL_w$ range. For a 2 MHz log, the permittivity can be used in both low (1 ppk to 50 ppk) and high (60 ppk to 150 ppk) salinities and gives excellent predictions. On the other hand, the predictions based on conductivity logs work well on a high $SAL_w$ range (60 to 150 ppk), but poorly on a low $SAL_w$ range (1 ppk to 50 ppk). These results support the observations that resistivity logs cannot estimate saturation reliably in a freshwater reservoir. It seems that combining the permittivity and conductivity logs always enhances the quality of predictions in both low and high $SAL_w$ scenarios.

The field logs from two wells were selected to test the methodology. Logs from Well-A was used to train the model. Excellent predictions of the $\phi_w$ are achieved for the trained model. In addition, very good predictions

**Fig. 16** *The model application and data fit: (a) The regression after applying the model trained in Fig. 15 on both the permittivity and conductivity logs, and (b) the comparison of $\phi_w$ values from the model prediction (black) with those from the conventional interpretation (red).*
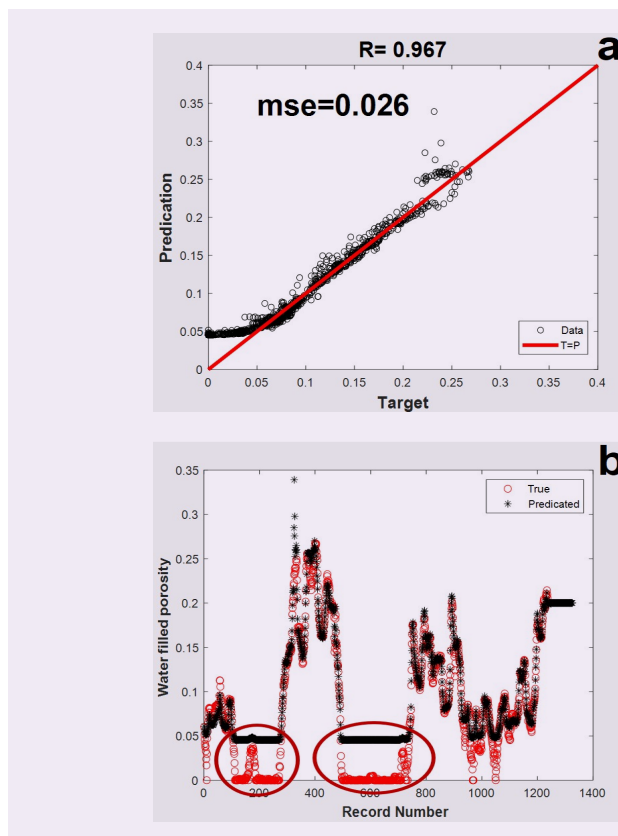
were observed when the trained model was used on the logs from Well-B. In a practical sense, it means that if a good model can be trained based on the logs from one well, then the $\phi_w$ can be predicted using the trained model in neighboring wells. Keeping that in mind, only two wells are used in the testing. Large-scale tests are needed to confirm the findings.

## Acknowledgments

## References

1. Rasmus, J.C., Homan, D., Wang, G.L. and Uschner, N.: "Observations of Induction Dielectric Measurements and their Role in Determining Thermal Maturity of Organic Mud Rocks," paper presented at the SPE/AAPG/SEG Unconventional Resources Technology Conference, Houston, Texas, July 23-25, 2018.

2. Wang, G.L., Homan, D.M., Uschner-Arroyo, N., Zhang, P., et al.: "Determining Resistivity and Low Frequency Dielectric Constant Using Induction Data in the Presence of Strong Induced Polarization," paper presented at the SPWLA 60$^{th}$ Annual Logging Symposium, The Woodlands, Texas, June 15-19, 2019.

3. Sen, P.N., Scala, C. and Cohen, M.H.: "A Self-Similar Model for Sedimentary Rocks with Application to the

Dielectric Constant of Fused Glass Beads," *Geophysics*, Vol. 46, Issue 5, May 1981, pp. 781-795.

4. Stroud, D., Milton, G.W. and De, B.R.: "Analytical Model for the Dielectric Response of Brine-Saturated Rocks," *Physical Review B*, Vol. 34, Issue 8, November 1986, pp. 5145-5153.

5. Seleznev, N.V., Habashy, T.M., Boyd A.J. and Hizem, M.: "Formation Properties Derived from Multifrequency Dielectric Measurements," paper presented at the SPWLA 47th Annual Logging Symposium, Veracruz, Mexico, June 4-7, 2006.

6. Freed, D.E., Seleznev, N., Hou, C-Y., Fellah, K., et al.: "A Physics-Based Model for the Dielectric Response of Shaly Sands," paper presented at the SPWLA 57th Annual Logging Symposium, Reykjavik, Iceland, June 25-29, 2016.

7. Hizem, M., Budan, H., Deville, B., Faivre, O., et al.: "Dielectric Dispersion: A New Wireline Petrophysical Measurement," SPE paper 116150, presented at the Annual Technical Conference and Exhibition, Denver, Colorado, September 21-24, 2008.

8. Seleznev, N.V., Hou, C-Y., Freed, D.E., Habashy, T.M., et al.: "Coherent Interpretation of Wideband Electromagnetic Measurements in the Millihertz to Gigahertz Frequency Range," paper presented at the SPWLA 58th Annual Logging Symposium, Oklahoma City, Oklahoma, June 17-21, 2017.

9. Ma, S.M., Pfutzner, H., Al-Hajari, A.A., Musharfi, N.M., et al.: "Resolving the Mixed Salinity Challenges with a Methodology Developed from Pulsed Neutron Capture Gamma Ray Spectral Measurements," SPE paper 170608, presented at the Annual Technical Conference and Exhibition, Amsterdam, the Netherlands, October 27-29, 2014.

10. Wythoff, B.J.: "Backpropagation Neural Networks: A Tutorial," *Chemometrics and Intelligent Laboratory Systems*, Vol. 18, Issue 2, February 1993, pp. 115-155.

## About the Authors

**Dr. Ping Zhang**

*Ph.D. in Geophysics,*
*Uppsala University*

Dr. Ping Zhang joined Schlumberger in 1999 as a Principal Geophysicist. He retired in 2021. Ping started his career as an Assistant Researcher at the University of Montreal, Montreal, Canada, from 1990 to 1994, and an Area Geophysicist for Inco Ltd., a mining company in Canada from 1995 to 1998.

His research focused on the application of electromagnetic (EM) technologies for geophysical exploration and characterization, with an emphasis on developing numerical techniques that are used for interpretation of EM data.

Ping worked on cross-well EM data quality control, processing, inversion and interpretation for petroleum applications. He was also actively involved in studies and development for reservoir monitoring and characterization.

Ping has published more than 50 peer-reviewed conference papers and holds 12 granted U.S. patents. He is a member of the Society of Petroleum Engineers (SPE), the Society of Petrophysicists and Well Log Analysts, and the Society of Exploration Geophysicists.

In 1989, Ping received his Ph.D. degree in Geophysics from Uppsala University, Uppsala, Sweden.

**Dr. Wael Abdallah**

*Ph.D. in Chemical Engineering,*
*University of Alberta*

Dr. Wael Abdallah joined Schlumberger in 2005 as a Research Scientist at the DBR Technology Center, Edmonton, Canada. He is currently the Managing Director of Schlumberger's Dhahran Carbonate Research Center in Saudi Arabia. Wael's research focuses on interfacial science for better downhole reservoir characterization, while also actively investigating better petrophysical reservoir characterization using multiphysics.

Prior to this assignment, he was the Program Manager for the geology, rock physics, and recovery research activities within the same center. Wael also managed commercial services related to reservoir fluids phase behavior and flow assurance. He also worked as an instructor with the NeXT technical training team on reservoir fluids.

In 2005, Wael received the Alberta Ingenuity Award.

He has published and coauthored more than 70 peer-reviewed conference papers, in addition to having 15 granted U.S. patents.

Wael is a member of the Society of Petroleum Engineers (SPE) and the Society of Petrophysicists and Well Log Analysts. He holds a professional Engineering Status in Canada.

Wael received both his B.S. and M.S. degrees in Chemical Engineering from the Jordan University of Science and Technology, Irbid, Jordan, majoring in fluid phase behavior and thermodynamics.

In 2005, he received his Ph.D. degree in Chemical Engineering from the University of Alberta, Edmonton, Canada, majoring in heterogeneous catalysis and surface science.

**Dr. Gong Li Wang**

*Ph.D. in Applied Geophysics,*
*China University of Petroleum*

Dr. Gong Li Wang is a Principal Modeling and Simulation Engineer at the Schlumberger Houston Formation Evaluation Center. He works on electromagnetic logging answering product development, and provides internal and external support on induction tools, including triaxial induction, array induction and through bit induction.

Gong was cited in the top 25 of all papers in the 2018 Society of Exploration Geophysicists (SEG) annual meeting for his work on induction logging in triaxially anisotropic formations. Prior to joining Schlumberger, he worked with the University of Illinois at Urbana-Champaign on computational electromagnetics and acoustics, and the University of Texas at Austin on electromagnetic logging and multiphysics inversion from 2002 to 2008.

Gong started his career with the China University of Petroleum, Shandong, China, where he worked on electromagnetic logging from 1993 to 2002.

In 1993, he received his B.S. degree in Borehole Geophysics, and a Ph.D. degree in Applied Geophysics in 2001 from the China University of Petroleum, Beijing, China.

**Dr. Shouxiang M. Ma**

*Ph.D. in Petroleum Engineering,*
*New Mexico Institute of Mining*
*and Technology*

Dr. Shouxiang M. "Mark" Ma is a Senior Petroleum Engineer Consultant overseeing research and development, subject matter technical support, and professional development in the Advanced Petrophysical Modeling Group of Saudi Aramco's Reservoir Description and Simulation Department. Prior to this, he was Supervisor of the Petrophysical Support & Study Unit, advisor at the Upstream Professional Development Center, and Lead Petrophysicist for logging operations.

Before joining Saudi Aramco in 2000, Mark worked at the Exxon Production Research Company, Wyoming Western Research Institute, New Mexico Petroleum Recovery Research Center, and China Yangtze University.

He served as a chairperson of the 2013 Society of Petroleum Engineers (SPE) Formation Evaluation Award Committee, the 2018 SPE Annual Technical Conference and Exhibition Formation Evaluation Committee, and on the 2019 International Petroleum Technology Conference Education Week Conference.

Mark was awarded the 2019 SPE MENA Formation Evaluation Award.

From 2015 to 2020, he served on the *JPT* Editorial Board where he was responsible for formation evaluation content. Mark is a Society of Petrophysicists and Well Log Analysts (SPWLA) Saudi Arabia Chapter vice president for technical events, and from 2018 to 2020, he was a SPWLA Director representing the Middle East and Africa region. Mark is also an Associate Editor for the *Journal of Petrophysics*, and Vice President of the SPWLA Saudi Arabia Chapter.

He received his B.S. degree from the China University of Petroleum, Shandong, China, and his M.S. and Ph.D. degrees from the New Mexico Institute of Mining and Technology, Socorro, NM, all in Petroleum Engineering.

# A Safer Dual Functional Gas Hydrate Dissolver and Inhibitor to Replace Methanol

*Dr. Mohammed A. Sayed, Dr. Rajesh K. Saini, Eyad A. Alali, Dr. Rajendra A. Kalgaonkar and Ahmed B. Al-Arnous*

**Abstract /**

In the presence of free water and under certain conditions of temperature and pressure, low molecular weight gases, such as methane and ethane, present in the fluid stream flowing in pipelines, cause gas hydrate crystals to form. These gas hydrate crystals may accumulate and cause a partial or complete plugging of pipelines in the vertical or horizontal section. Methanol has been used in the industry as an effective gas hydrate dissolver and inhibitor, and its low flash point temperature makes it unsafe to be stored and pumped in large volumes.

The objective of the current work is to develop a safer dissolver and inhibitor for gas hydrate plugs that form in pipelines. Methanol has a very low freezing point (-90 °C) and it is completely miscible with water, which can shift the hydrate phase equilibrium to lower temperatures. Solvent- and aqueous-based formulations were selected as alternatives to methanol, keeping in mind the parameters such as higher flash point, miscibility with water, freezing point, viscosity, and local availability.

The performance of these formulations was evaluated in a see-through gas hydrate reactor. Representative gas and water compositions were used in the experiments to form gas hydrate inside the reactor. Hydrate formation was detected by the change in torque or by visual inspection through the see-through window of the reactor. Methanol was able to mobilize the hydrate plug when used at 10 vol%, while complete dissolution was achieved at 30 vol%.

In comparison, the potassium (K) formate saturated solution achieved complete dissolution of the hydrate plugs after adding 10 vol% in less time compared to methanol. The tested formulations not only worked as a dissolver but also worked as an inhibitor to prevent the formation of hydrates once they are melted or dissolved. These formulations enabled safer operations in the field and improved the performance when it comes to melting gas hydrate plugs.

## Introduction

Low molecular weight hydrocarbons, such as methane, ethane, propane, butane, and iso-butane, and sometimes other gases such as carbon dioxide ($CO_2$) and hydrogen sulfide ($H_2S$), are normally present in pipelines or other conduits used in the transportation and processing of natural gas and crude oil. When a gas stream is subjected to low temperatures (< 20 °C or 68 °F) and/or elevated pressures (> 30 bar or 450 psi) in the presence of free water, gas hydrate crystals are typically formed[1, 2]. Gas hydrates are clathrates or insertion compounds in which the previously mentioned small hydrocarbon molecules are trapped in a lattice consisting of water molecules[1]. Hydrates form as a consequence of the tendency of water to reorient in the presence of a nonpolar solute (typically light hydrocarbon gases such as methane) to stabilize the lattice through, typically, Van der Waals interactions while maintaining the hydrogen bonding between the water molecules. The trapped small gas molecules are called guest molecules and they stay trapped within the water cages and strengthen it[3].

Gas hydrates are categorized rendering the number of water molecules in a crystal as:

- Structure I: Where the most commonly found gases here are $CO_2$, methane, and ethane.
- Structure II: Here the gas species are mainly nitrogen, oxygen, propane, and some higher components of natural gas.
- Structure H: Here the gas component can be any mix of the above species.

Both Structure II and Structure H gas hydrates generally occur in offshore environments because of the low temperature and high pressure encountered by produced fluid in the pipeline. If there is a continuous supply of gases, then Structure H gas hydrates can transform into type I[4, 5].

Hydrate formation inside a conduit — such as a pipeline — is undesirable because the crystals might cause plugging of flow lines, valves, and instrumentation, reducing line capacity, pipe bends and/or causing physical damage to pipelines and equipment[6, 7]. Unless the gas hydrate plug is only partially plugging the pipe, such gas hydrate plugs tend to separate a pipe into two zones: a high-pressure zone between the wellhead and the plug, and a low-pressure zone between the plug and the production facilities area. If the plug and the pipe wall are suddenly unstuck, a projectile may be generated, which can destroy the pipeline at any restriction or facilities apparatus.

The solution is to decrease the pressure both on the wellhead side and on the platform side, but there is still a potential risk for the generation of a projectile.

A gas hydrate envelope can be defined as the thermodynamic conditions (pressure and temperature) at which gas hydrate can form. The gas hydrate envelope presents a graphical relationship of pressure and temperature to show the boundaries between gas hydrate and the gas hydrate-free regions. Experimental procedures can be used to establish the thermodynamic curves (or gas hydrate envelope). The experimental data includes pressure, temperature, the gas composition, brine composition, and other elements that may be present in the fluid system flow in the pipeline[2, 8].

Figure 1 is an example of a gas hydrate envelope. The regions on the right of the curve represent the conditions at which there is no gas hydrate formation while the conditions on the left represent the conditions under which a gas hydrate may form.

There are several actions that can be considered to prevent the formation and accumulation of gas hydrate in the pipelines. Among these actions, one of the methods is to reduce the pressure to keep the overall gas mixture outside the hydrate stability zone[9]. This solution may not be practical especially when production takes place from deep-water horizons[9].

Another action is to increase the temperature of the conduit, either by insulating the conduit or by heating[10-12], above the gas hydrate equilibrium temperature. Other actions intend to either remove the free water from the gas or oil stream through a dehydration process or add another gas (such as nitrogen ($N_2$)) to modify the gas composition in a way that prevents the formation of the stable gas hydrate crystals[13, 14].

## Chemical Prevention of Gas Hydrate Plugging in Conduits

The chemical treatments that can be used to prevent the formation of hydrate plugging can be classified into three main categories: Thermodynamic hydrate inhibitors (THIs), kinetic hydrate inhibitors (KHIs), and anti-agglomerants (AAs)[2, 15]. KHIs and AAs can be summed up under one category, denoted as low dosage hydrate inhibitor (LDHI), where the concentration of the active ingredient is less than 1 wt% from the total chemical treatment[16, 17]. In many cases, a combination of, or switching between, two of the above categories can be used[16, 18].

### Thermodynamic Hydrate Inhibitors (THIs)

THIs or "hydrate antifreeze" are the most commonly used hydrate inhibitors[1]. A THI functions to shift the equilibrium conditions at which gas hydrate forms through changing the thermodynamic properties of the fluid mixture flowing in the conduit[1]. The THIs tend to either increase the hydrate formation pressure or lower the temperature so gas hydrate crystals will not form, or any already formed hydrate tends to melt. THIs are usually added in concentrations as high as two barrels of THI per one barrel of water. Glycols, such as mono-ethylene glycol (MEG), and alcohols such as methanol and



**Fig. 1** *The hydrate formation curve showing the different zones of hydrate and hydrate-free regions.*
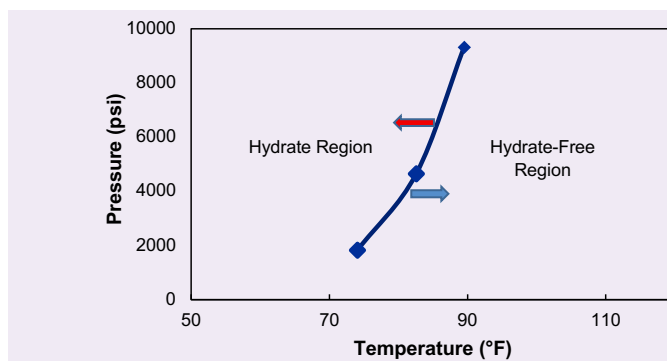
ethanol, are the commonly used THIs, and diethylene glycol and triethylene glycols are less likely to be used. They can be used to inhibit, and sometimes melt, gas hydrate plugging[19, 20].

Although both methanol and MEG are relatively cheap, adding a recovery unit to recover them and reuse in another treatment is a common practice since high volumes and dosages are usually used in the field[21]. The underestimation of the amount of a THI needed to inhibit gas hydrate may lead to partial or complete plugging as a result of the continuous buildup of gas hydrate crystals in the pipeline[22, 23].

In addition to alcohols, glycols, and salts, such as potassium chloride, K-formate, sodium and calcium chlorides, as well as sodium acetate, were found to suppress the formation of gas hydrate crystals. Other salts — nitrates and phosphates — were found effective as hydrate inhibitors[24, 25]. Bavoh et al. (2017)[26] investigated the use of amino acids as THIs to control gas hydrate. They found that inhibition of gas hydrate was possible using different types of amino acids such as glycine and alanine with glycine achieving inhibition slightly higher than that of ethylene glycol.

Although THIs are the most widely used technique to inhibit gas hydrate plugs, they have some operational challenges. These challenges may include the high cost of transportation and storage, flammability and toxicity, cost of regeneration, increased potential for scale deposition, as well as the possibility of causing downstream pollution and freezing of gas processing systems[27, 28].

### Kinetic Hydrate Inhibitors (KHIs)

Most of the KHIs are water-soluble polymers that are combined with small organic molecules. Recently, non-polymeric KHIs were developed and tested[29]. Although the polymers have little to no partitioning in liquid hydrocarbon phases, the performance may be impacted by the presence of these hydrocarbon liquids in the production stream. The KHIs are added to delay the nucleation of gas hydrate crystals so that crystal growth and accumulation can be hindered[30, 31].

One limitation of the field applications using KHIs is the maximum subcooling temperature (9 °C to 10 °C)

at which the treatment takes place. For this reason and as a guideline, KHIs may not be suitable for application in deepwater since subcooling and the pressure both will be high[32]. KHIs have been used in the field for more than two decades. They are added in low concentrations ranging from 0.1 wt% to 1 wt% of the water phase accompanying the gas stream[33], which implies huge savings in cost compared to methanol; which is used in large volumes[34].

Two structural features make polymers successful as KHIs; the presence of amide groups or similar groups that improve the hydrogen bonding between the polymer molecule and water molecule, and the presence of a hydrophobic group bonded directly to the amide group[35]. An example of an early KHI is polyvinylpyrrolidone[36, 37]. Most of the widely used KHIs belong to three classes of polymers: Vinyllactam polymers and copolymers, isopropylmethacrylamide polymers and copolymers, and hyperbranched polyesteramides[38, 39].

If the polymer has a low cloud point in water, this will help to improve the performance of the KHI, but at the same time it may make it susceptible to precipitation and dropout. The dropout of the polymer may result in plugging of injection points such as the wellhead. Another important component that may adversely impact the performance of the KHIs is the presence of sour gases such as $H_2S$ and $CO_2$ in high concentrations[40].

### Anti-Agglomerants (AAs)

AAs are another class of the low dosage hydrate inhibitor similar to KHIs. The advantage of using AAs over KHIs is that they can perform better in higher subcooling environments such as deep-water applications. AAs do not prevent hydrate formation but rather prevent the agglomeration of these hydrate crystals into larger masses that can cause plugging.

In pipelines, using AAs will cause the hydrate to form, but formed hydrate can still flow within the production stream as a slurry inside the liquid hydrocarbon phase (pipeline AAs).

In gas wells, the AAs work by dispersing the gas hydrate crystals in excess of free water using a gas well AA class of materials[4, 41, 42].

### Dissolving Gas Hydrate Plugs

Several methods can be used to dissolve a hydrate plug that is already formed in the pipeline. These methods include depressurization of the line, use of coiled tubing, heated wirelines, hot oiling, or chemical treatment. Most of the chemical treatments depend on the use of THIs or melting point depressants (antifreezes)[43]. Typical examples, include methanol and MEG. The use of MEG as a dissolver of already formed hydrate is very challenging and has not proven to be efficient in too many cases. Although, the use of methanol was proven efficient; however, the volume of methanol needed to effect dissolution of the plug may far exceed the amount required to sufficiently dilute the melted water. In addition, the low flash point temperature of methanol makes it unsafe to be stored in large volumes.

The main objective of the current study is to find a safer and efficient alternative to methanol to dissolve and mitigate the gas hydrate challenge in gas wells. But to develop the new solution, we first have to know why methanol is efficient in dissolving the hydrate plug. Some of the characteristics that make methanol work as a THI, or antifreeze agent, is its very low freezing point (-90 °C) and its complete miscibility with water that make it able to shift the equilibrium conditions for the hydrate to allow for free-gas hydrate flow conditions at lower temperatures. Methanol can be used to prevent and melt hydrate at the same time.

The criteria of success of any new treatment has been defined by field operators as follows:

- Flash point temperature must be higher than 122 °F (50 °C).
- Time to dissolve gas hydrate must be less than 2 hours.
- Wellhead temperature can be as low as 40 °F.

Here, we report the advancements made toward the development of high flash point temperature chemical treatments to dissolve and mitigate the gas hydrate plug formed in pipelines. The new treatment chemicals were selected to achieve similar characteristics to methanol that made it a successful dissolver, such as miscibility with water and low freezing point (less than -50 °C).

A list of chemicals was defined from both categories; aqueous-based and solvent-based chemicals. Three aqueous-based formulations were identified, while one of them was tested in the field and proved effective in dissolving/mitigating gas hydrate plugs. The three formulations identified are K-formate, cesium formate (Cs-formate), and a mixture of K and Cs formate (K & Cs-formate).

Two solvents were identified and tested, and proved effective in dissolving and mitigating gas hydrate plugs. The two solvents identified are diethylene glycol monoethyl ether (DEGEE) (flash point = 205 °F/96 °C) and 2-butoxyethanol (2-BE) (flash point = 149 °F/65 °C). The success of the K-formate fluid system injected at both ambient (70 °F) and high temperature (250 °F) to dissolve the already formed hydrate plug was confirmed from the analysis of the data collected from the visual cell autoclave testing where the gas hydrate was allowed to form under conditions similar to field conditions (temperature around 50 °F and pressure is around 4,000 psi to 5,000 psi).

## Experimental Study

### Materials

The gas composition, as obtained from the field, was created in the lab for testing purposes. Table 1 lists the composition of two samples of the gas fluid produced from the same well as well as the average gas composition used in the experimental work.

The second main component in creation of gas hydrate is water. The availability of free water, gas, and favorable conditions of pressure and temperature is the main drive to form gas hydrate crystals and the gas hydrate plugs. The water composition used to perform the testing experiments in the visual cell is a mixture of formation brine and freshwater in the ratio of 10/90.

The freshwater was deionized water obtained from a

| Component | Sample 1 | Sample 2 | Average |
|-----------|----------|----------|---------|
| C1 | 84.24 | 83.06 | 83.65 |
| C2 | 4.71 | 4.68 | 4.70 |
| C3 | 1.39 | 1.41 | 1.40 |
| iC4 | 0.28 | 0.29 | 0.29 |
| iC5 | 0.19 | 0.22 | 0.21 |
| C6 | 0.22 | 0.3 | 0.26 |
| C7 | 0.18 | 0.31 | 0.25 |
| C8 | 0.12 | 0.33 | 0.23 |
| C9 | 0.04 | 0.21 | 0.13 |
| $CO_2$ | 2.36 | 2.33 | 2.35 |
| $H_2S$ | 0 | 0 | 0.00 |
| $N_2$ | 5.68 | 5.59 | 5.64 |
| nC4 | 0.43 | 0.46 | 0.45 |
| nC5 | 0.16 | 0.19 | 0.18 |

thermo scientific Barnstead Smart2Pure water purification system, having a resistivity of 18.2 MΩ.cm ($DI\text{-}H_2O$). The composition of the formation brines was obtained from two main samples collected from two different wells. Synthetic brine mimicking the field brines was prepared in the lab and used for testing. Table 2 lists the composition of the samples as well as average water composition used in the experimental work.

As stated previously, methanol was efficient in dissolving the hydrate plug. Methanol works as a THI or antifreeze because of its very low freezing point as well as its ability to shift the equilibrium conditions for the hydrate to allow for free gas hydrate flow conditions at lower temperatures. Methanol can be used to prevent and melt hydrate at the same time. A list of possible alternative chemicals to methanol were collected for testing. The criteria for selecting these alternatives are:

- Low melting point: < -50 °C (-58 °F).
- High flash point temperature > 50 °C (122 °F).
- Complete miscibility with water.

For any of the selected alternatives to be successfully utilized in the field, it must fulfill the following criteria:

- Comparable performance to methanol, the only dissolver known to work.
- Locally available or can be sourced easily in the field in large volumes.
- Economically viable alternative to methanol.

Table 3 lists the chemical, boiling point, melting point, flash point temperature, density, viscosity, and miscibility with water of the chemicals that were selected.

**Visual Cell Testing Procedure**

A gas hydrate visual cell was used to study the formation and dissolution of gas hydrate under real wellhead conditions. The temperature range that the visual cell can be used is between 0 °F and 180 °F (with thermometer accuracy of ±2 °F and resolution of 0.01 °F) with a maximum pressure of 10,000 psi (with accuracy of ± 0.1% of full scale and a resolution of 0.001 psig) and maximum paddle speed of 1,200 rpm.

The cell is equipped with two cameras (side and bottom view) to record video of the occurrence of gas hydrate. Pressure, temperature, paddle speed, and torque (torque range is 0 ounce-inches (oz-in) to 80 oz-in with a resolution of ± 0.08 oz-in), and is recorded via LabView. The system is equipped with injection ports for injection of chemicals during experiments. The water used in the experiment was a mixture of 90% freshwater and 10% formation brine. The visual cell can measure the torque while mixing gas and brines as well as while injecting the dissolver/inhibitor chemical package.

In cases where there is no hydrate formation in the fluid, the torque encountered by the mixer will have normal values of the liquid solution. In cases where gas hydrate forms in the cell, the torque will start to increase until everything freezes, and the stirrer is not able to turn. The visual cell has a capacity of 875 mL and only 10% to 15% volume of the cell is filled with the water mixture for the testing. The remainder of the cell will be filled with gas having the same composition as the gas from the field until the cell pressure reaches 4,000 psi to 5,000 psi.

The testing procedure can be summarized in the following steps:

1. Prepare fluids to be used in the test, i.e., hydrate dissolver, brine mixture, and gas mixture.

|  | Na | Ca | Mg | $SO_4$ | Cl | TDS | pH | Ba | Sr |
|--|-----|-----|-----|--------|-----|-----|-----|-----|-----|
| Sample 1 | 47,000 | 31,700 | 1,220 | 236 | 132,000 | 212,156 | 3.9 | 2,239 | 2,200 |
| Sample 2 | 51,600 | 31,900 | 1,400 | 249 | 140,000 | 225,149 | 3.2 | 2,647 | 2,891 |
| Average | 49,300 | 31,800 | 1,310 | 243 | 136,000 | 218,653 | 4 | 2,443 | 2,546 |

**Table 3** *A list of chemicals that may work as a gas hydrate dissolver.*

| Chemical Name | Boiling Point (°C) | Melting Point (°C) | Flash Point (°C) | Solubility with Water | Density | Viscosity |
|---|---|---|---|---|---|---|
| Methanol | 64.4 | -98 | 12 | Soluble | 0.79 | 0.7 cP at 10 °C |
| Cs Formate (50 wt%) | > 100 | -50 | No Flash | Soluble | 1.05 - 2.5 | 1.7 to 10 cP at 25 °C |
| K Formate (50 wt%) | > 100 | -50 | No Flash | Soluble | 1.57 | 7 to 13 cP at 25 °C |
| 1:1 Cs and K Formate (each is 50 wt%) | > 100 | -50 | No Flash | Soluble | 1.44 - 2.4 | 1 to 15 cP at 25 °C |
| DEGEE | 196 | -76 | 96 | Soluble | 0.999 | 3.85 cP at 25 °C |
| 2-BE | 171 | -70 | 67 | Soluble | 0.902 | 6.4 cP at 20 °C (68 °F) |

2. Maintain the cell temperature at 100 °F.

3. Add 120 ml of brine to the cell (10:90 vol% of formation brine to freshwater).

4. Add gas until cell operating pressure is achieved (4,000 psi to 5,000 psi).

5. Start mixing and measuring the torque on the cell shaft.

6. Slowly cool-down the cell from 100 °F to a temperature around 50 °F to allow the formation of hydrates. A sudden increase in torque and drop-in pressure indicates the formation of gas hydrates.

7. In case no hydrate plug is formed (detected either visually or by an increase in the torque), then stop mixing and shut-in the cell overnight to allow the formation of a hydrate plug.

8. Try to initiate mixing to make sure hydrate is formed as indicated by either high torque or by the inability to turn the paddle.

9. Once hydrate is formed, start adding the gas hydrate dissolver. Start with 10 vol% or 2.5 vol% dosage and keep incrementally increasing the dosage (2.5 vol% or 5 vol%) and wait for two hours.

10. Start mixing, and measure torque.

11. Repeat the previous steps until the hydrate is cleared (torque goes back to normal values measured before hydrate plug formed as shown in step 4).

12. After the last step of adding the gas hydrate dissolver is completed, heat up the cell to 100 °F and make sure the cell is back to initial conditions.

## Results and Discussions

### Control Experiment (Test 1): Use of Methanol as Gas Hydrate Dissolver

The experiment was performed using the following steps:

1. Saturation Step: Add 120 ml of synthetic deionized water/brine (90:10) in the cell. Evacuate the cell and then pressurize it with gas mixture to 4,500 psi and heat it up to a temperature of 100 °F.

2. Hold for two hours while mixing at 400 rpm to fully saturate the fluids with gas. Record video every hour for a duration of two minutes from the bottom and side cameras (one minute each).

3. Stop the mixing and allow fluids to separate over 30 minutes to aid in visual observation. Record video every 15 minutes for a duration of two minutes from the bottom and side cameras (one minute each).

4. Cooling step: Restart and maintain mixing at 400 rpm. Isolate the gas reservoir from the cell (constant volume mode). Slowly cool-down the cell from 100 °F to 50 °F over a span of 10 hours.

5. First mixing step: Once the temperature is stabilized at 50 °F, keep mixing at 400 rpm and 50 °F for 10 hours. Record video every 1 hour for a duration of two minutes from the bottom and side cameras (one minute each).

6. Shut-in step: Stop mixing and hold the cell at 50 °F for 10 hours. Record video every hour for a duration of two minutes from the bottom and side cameras (one minute each).

7. First methanol addition: Add 10 vol% methanol (12 ml) and start mixing at 400 rpm for two hours. Record video every 30 minutes for a duration of two minutes from the bottom and side cameras (one minute each).

8. If the torque recorded does not decrease to normal within the two-hour window, repeat step 7 by adding methanol in 10 vol% steps.

9. After the hydrate plug has been dissolved and plugging is cleared, heat the cell from 50 °F to 100 °F over a span of five hours. Record video every hour for a

duration of two minutes from the bottom and side cameras (two minute each).

The results of methanol testing (Test 1) are shown in Fig. 2. Test 1 was performed at a constant gas volume starting at 4,500 psi with no inhibitor. During the cooling step from 100 °F to 50 °F, the pressure decreased to 3,250 psi at a constant volume. Meanwhile, the torque remained at 10 oz-in. During the following mixing steps, the torque continued to increase until it exceeded the maximum operating torque. This provides evidence that hydrate was formed. By adding 10 vol% of methanol (12 ml, with respect to the initial volume of water in the cell), there was no change observed in the torque.

After two hours, another 10 vol% of methanol was added and within a few minutes, the torque started to decrease, and a slurry of the hydrate was formed. The torque decreased to initial value when the methanol concentration was increased to around 30 vol% after adding an additional 10 vol% dosage.

This experiment shows that 30 vol% of methanol is needed to completely dissolve the formed gas hydrate within the set two-hour time period.

### Test 2: Use of K-Formate (Ambient Conditions)

Figure 3 shows the results of Test 2 using K-formate as a gas hydrate dissolver. The same procedure was followed in Test 2 as mentioned in Test 1, where K-formate was used as a dissolver instead of methanol to melt the hydrate plug. The torque recorded for the solution mixture before the formation of the hydrate was around 8 oz-in. Upon cooling down the cell, hydrates started forming at 55.7 °F and 3,826 psi. The hydrates never over torqued

the mixer during the cool-down, over a 10 hour mixing period at 50 °F. Then, the stirring process was stopped, and the cell was aged for 10 hours to allow the hydrate to accumulate and to form a hydrate plug.

After the 10-hour shut-in, the mixer was restarted and the hydrate plug over torqued the mixer indicating the formation of a hydrate plug. The mixer was restarted for a period of two hours with restart attempts every 15 minutes. A 10% by volume of K-formate (12 ml of 75% solution of K-formate) was injected, and after one hour the mixer was able to move the hydrate plug with an initial torque of 26.4 oz-in, which was recorded.

This indicated that the K-formate was able to breakdown the hydrate plug and formed a slurry of crystals distributed in the water phase. After approximately 30 minutes of mixing, the torque had dropped to pre-hydrate values of around 8 oz-in without adding any more K-formate.

In conclusion, 10 vol% K-formate is required to completely dissolve the gas hydrate in 30 minutes, whereas 30 vol% of methanol is required to dissolve the gas hydrate in two hours. Six chemical loadings starting at 10%, then in 5% increments thereafter for a total volume of 30% were injected to duplicate the experiments performed using other formulations (similar to methanol).

### Test 3: Heated K-Formate (K-Formate at 250 °F)

Figure 4 shows the results of Test 3 performed using K-formate (at 250 °F) as a gas hydrate dissolver. The same procedure as described previously in Tests 1 and 2 were followed in Test 3. K-formate was heated to 250 °F before injecting into the cell — K-formate has a very high heat capacity. The main purpose of this experiment

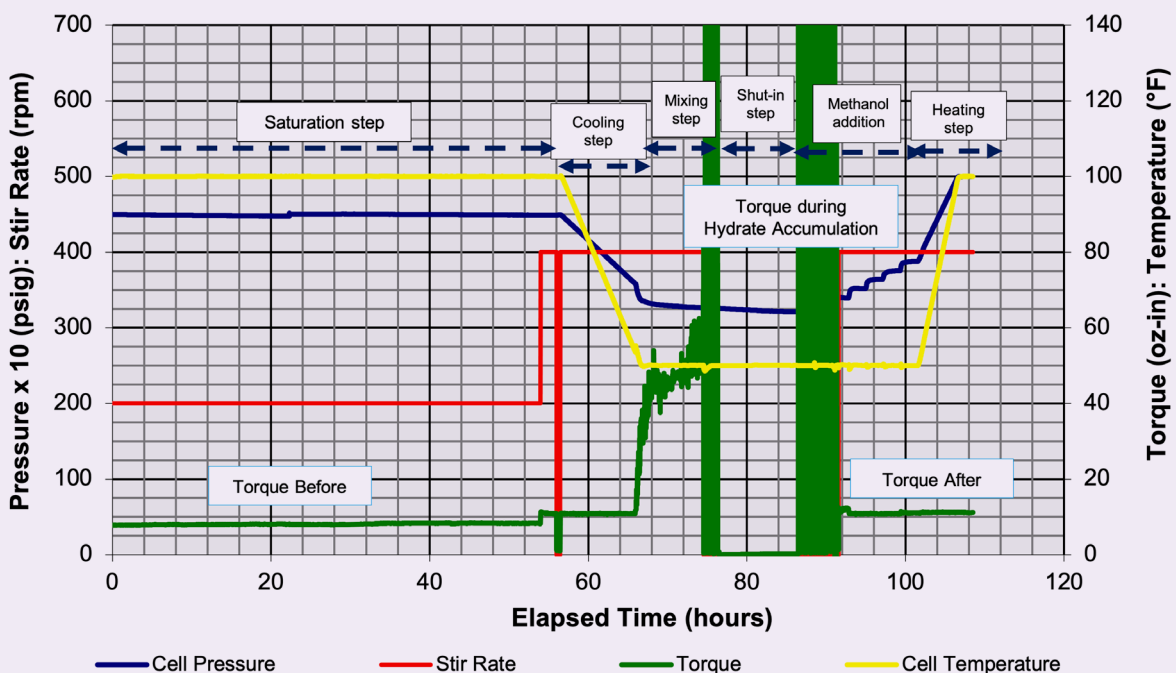**Fig. 2** *The results of Test 1 performed using methanol as a gas hydrate dissolver.*

**Fig. 3** *The results of Test 2 performed using K-formate as a gas hydrate dissolver.*
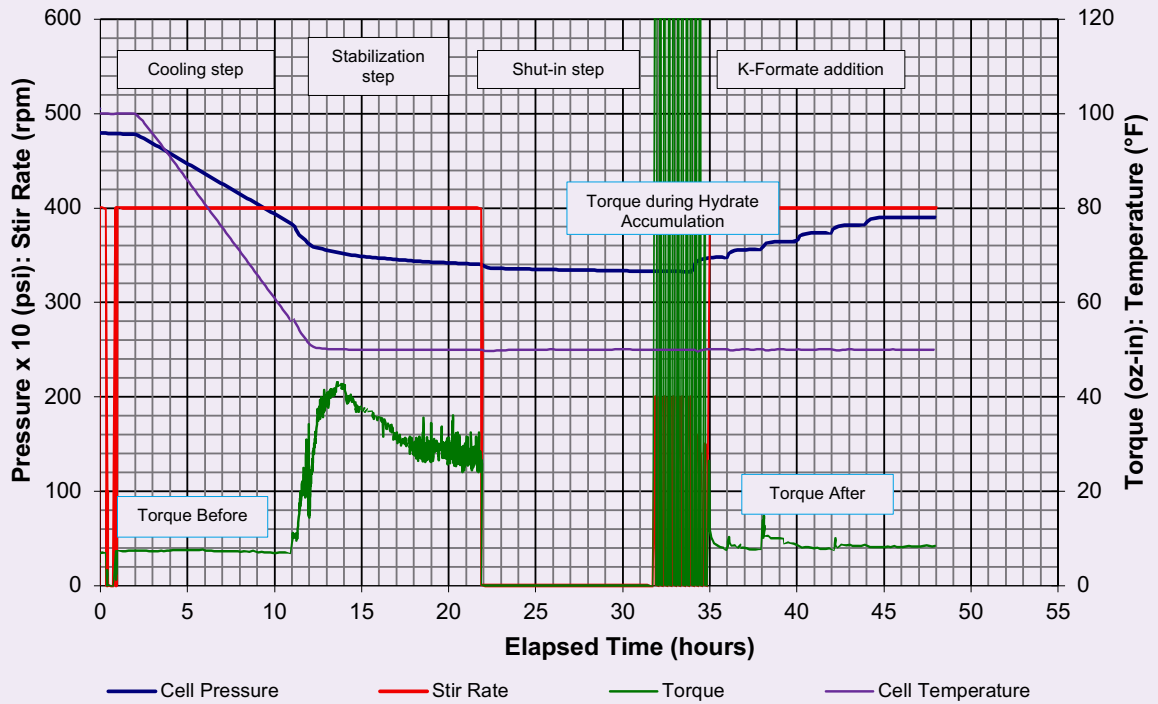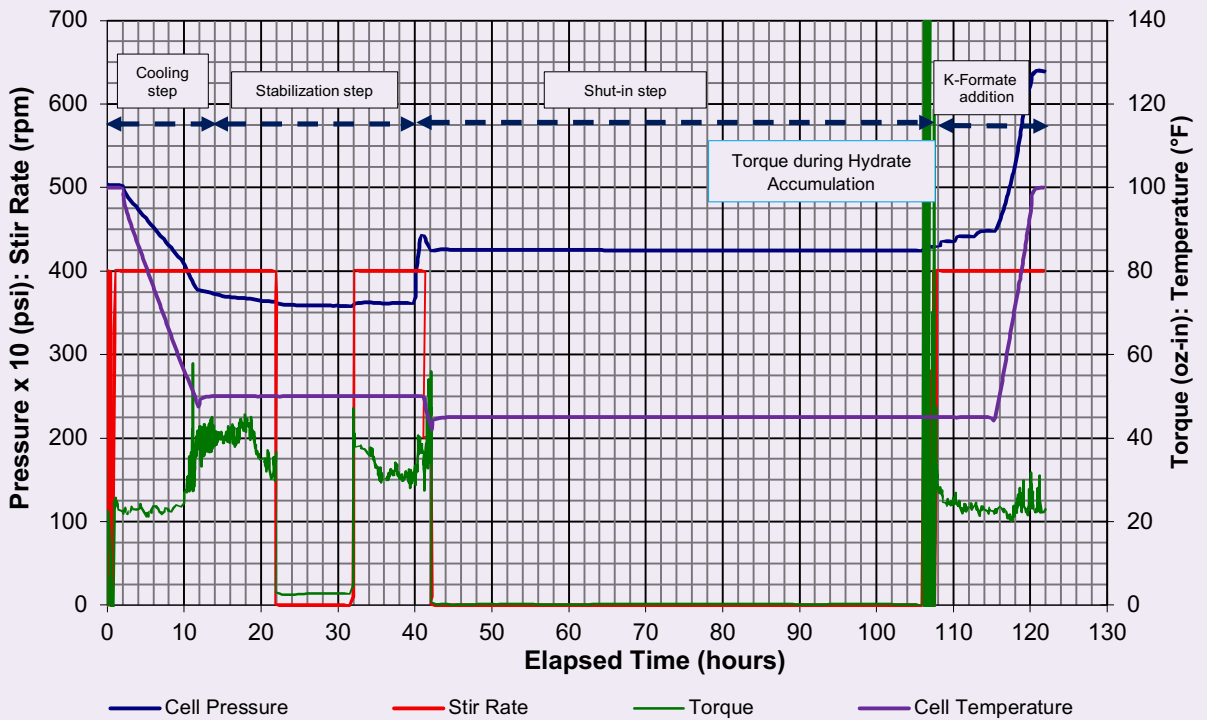


**Fig. 4** *The results of Test 3 performed using K-formate (at 250 °F) as a gas hydrate dissolver.*

was to evaluate the impact of using hot fluids on the acceleration of dissolving the gas hydrate plug.

Hydrates formed during the cooling ramp at a pressure of 4,095 psi and a temperature of 56 °F. The torque increased from approximately 22 oz-in up to 45 oz-in during the completion of the cooling ramp over a 10-hour mixing period at 50 °F. The stirring of the fluid mixture was stopped, and the cell was aged for an additional 10 hours. After the 10-hour hold period, mixing was restarted and a torque of 40 oz-in was recorded. The torque declined and stabilized at 30 oz-in to 32 oz-in over the next eight hours. Chemical injection was not performed at this stage due to the lack of a hydrate plug.

To achieve a hydrate plug, the cell pressure was increased by injecting additional gas where the pressure spiked from 3,620 psi to 4,400 psi. The cell temperature was lowered from 50 °F to 45 °F, and the system was held at these conditions over a period of 48 hours. The mixer was started and immediately over torqued, indicating the formation of a hydrate plug.

The first injection of 2.5 vol% K-formate at 250 °F was performed. For the first hour and 15 minutes, the mixer continued to over torque. After one hour and 30 minutes, the hydrate plug broke and mixing was established with a torque reading at 35 oz-in. The second injection was done after 30 minutes and torque dropped to 25 oz-in. The third injection of another 2.5 vol% of the heated K-formate lowered the torque to approximately 22 oz-in, matching the initial torque at the beginning of the test. A fourth injection of heated K-formate had no additional reduction in torque and the test was terminated. All injections were performed at 2.5 vol% stepwise.

### Test 4: Use of DEGEE

Figure 5 shows the results of Test 4 performed using DEGEE as a gas hydrate dissolver. The torque measured prior to the formation of hydrate was approximately 10 oz-in. Gas hydrates started forming at 60 °F and 4,060 psi. The hydrates never over torqued the mixer during the cool-down over a 10-hour mixing period at 50 °F. After the 10-hour shut-in period, the mixer was restarted and the hydrate plug over torqued the mixer during a one-hour period.

A 10% volume (12 ml) of DEGEE was injected and after 30 minutes, the mixer was able to move the hydrate plug with a torque of 17 oz-in to 18 oz-in. Five chemical loadings were injected starting at 10%, then in 5% increments thereafter for a total volume of 30%. Each additional injection lowers the torque and at the final step the torque equals the initial torque response prior to cooling. A complete dissolution of the gas hydrate plug was achieved after injecting between 10 vol% to 15 vol% of DEGEE.

### Test 5: Use of 2-BE

Figure 6 shows the results of Test 5 performed using 2-BE as a gas hydrate dissolver.

The same procedure was followed as in Test 4. The torque measured before the formation of hydrate was approximately 9 oz-in. During the cooling stage, gas hydrates formed at 4,189 psi and 68.3 °F. Torque response varied between 40 oz-in to 50 oz-in during the remaining

**Fig. 5** *The results of Test 4 performed using DEGEE as a gas hydrate dissolver.*
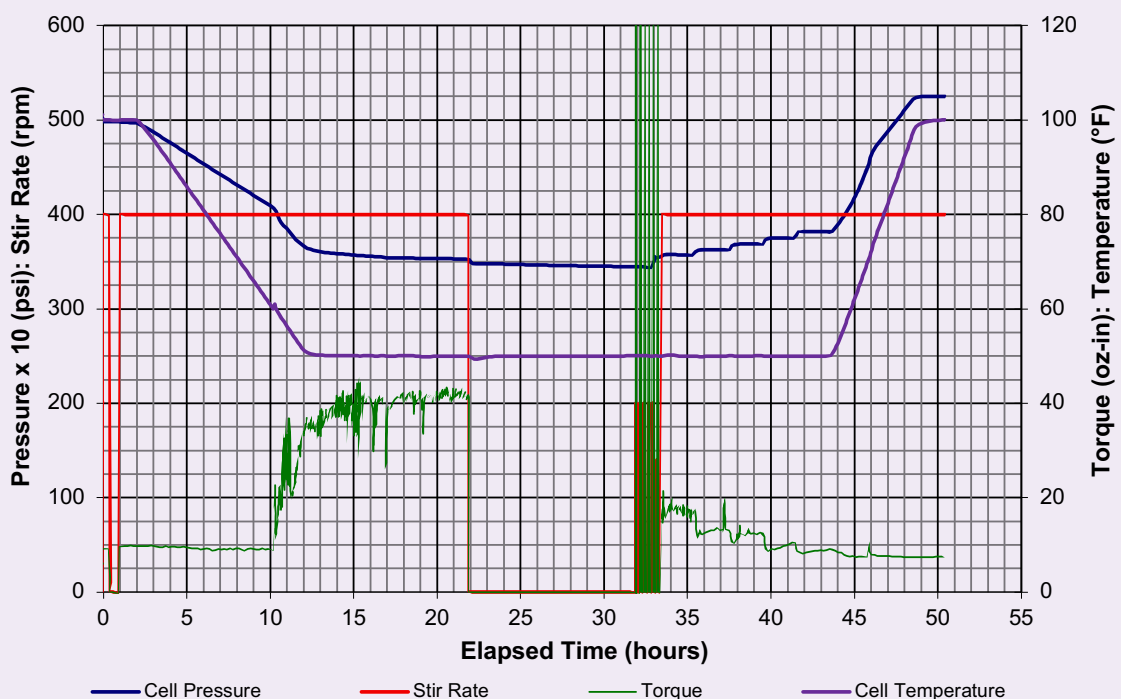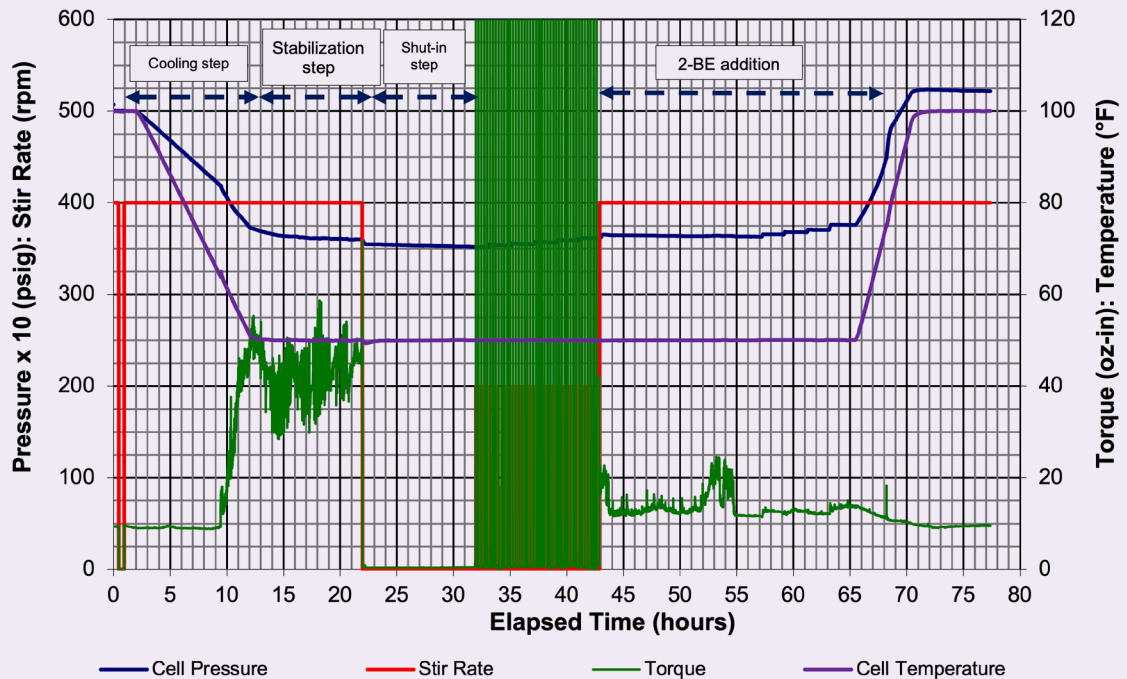
**Fig. 6** *The results of Test 5 performed using 2-BE as a gas hydrate dissolver.*



period of ramping and the 10-hour hold with mixing at 50 °F. After the 10-hour shut-in period, a hydrate plug was formed and the motor over torqued at restart of mixing.

After an hour of attempted restarts, the first chemical injection of 2.5% (3 ml) was introduced. At approximately 1.5 hours after the fifth injection (total of 12.5 vol%) the hydrate plug began to breakdown and the mixer established constant rotation at 400 rpm. The resulting torque averaged at 20 oz-in. After the sixth injection (total of 15 vol% of 2-BE) was performed, the torque dropped to 9 oz-in to 10 oz-in (pre-hydrate torque). The system was maintained at this condition overnight. Four additional chemical volumes of 2.5% each (for a total test volume of 25%) were injected with little effect on torque response.

### Summary of Results of the Experimental Studies

A visual cell equipped with a stirrer and torque measurement transducer was used to test the formation and dissolution of gas hydrate plugs. The experiments were performed at conditions similar to those encountered at the wellhead, with a pressure of approximately 4,000 psi to 5,000 psi and a temperature between 40 °F to 67 °F.

Alternative chemical formulations were tested and proved efficient in dissolving/melting the gas hydrate plug. These alternatives are K-formate at both ambient and high temperature (at 250 °F), 2-BE, and DEGEE. A summary of the dosage needed, and time required to dissolve/melt the hydrate plug is given in Table 4.

The proposed formulations were able to dissolve the gas hydrate plug in a time interval of less than two hours. The new formulations were able to dissolve hydrate by using lower or similar volumes compared to methanol.

In addition, to dissolve the hydrate in a shorter time, these formulations have a higher flash point temperature (> 50 °C). As a result, these formulations are safer than methanol when it comes to transportation, storage, and pumping, which will improve the operations in the field.

### Field Testing and Results of Field Trials

The K-formate formulation was trial tested in two different wells. The K-formate was selected for two main reasons; availability and it is easy to prepare in the field. The K-formate solution was prepared in the field and transported to the well location without encountering any problems. Before the actual field job, the density of the prepared fluid was measured to ensure it meets the requirements of preparing a saturated formulation that meets the melting point depression requirements (< -20 °C).

### Test Trial 1

A 500 HP pump was utilized with a minimum pumping rate of 11 gallons per minute (gpm). The pump was connected to gas a streamline utilizing a 2" line with a check valve and manual valve at the pipe end to avoid back flow.

Upstream pressure was 4,200 psi, and the well was flowed on choke 12/64". Upon flowing the well for 15 minutes, hydrate started to form in a shape of pipe icing with a dramatic temperature drop (35 °F). K-formate was then pumped into the downstream line (after the choke) with a slow reaction. A total of 550 gallons of chemical were pumped at a rate of 11 gpm. The temperature increased from 38 °F to 65 °F in one hour, indicating a complete

**Table 4** *The summary of the alternative chemical performance compared to methanol.*

| Chemical Name | Flash Point (°C) | Tested or Planned to be Tested | Can It Melt Hydrate? |
|---|---|---|---|
| Methanol** | 12 | Yes | Yes (10 - 30 vol%) |
| K-formate (50%) | No Flash | Yes | Yes (10 vol%) |
| Heated K-formate (50% at 250 °F) | No Flash | Yes | Yes (2.5 - 7.5 vol%) |
| DEGEE | 96 | Yes | Yes (10 - 15 vol%) |
| 2-BE | 67 | Yes | Yes (12.5 - 15 vol%) |

hydrate dissolution.

The experiment was repeated, and hydrate was generated using the same methodology; however, K-formate was pumped in the upstream side. The reaction was rapid, and the temperature increased from 34 °F to 69 °F in just 20 minutes. A total of 330 gallons was pumped at a rate of 16.5 gpm.

**Downstream Injection of (K-formate):** Initially, the pipe temperature was at an ambient temperature of 77 °F. Upon flowing the well, the temperature in the upstream and downstream pipe changed to 96 °F and 38 °F, respectively. Once the temperature dropped, ice started to form as an indication of hydrate formation inside the pipe, Fig. 7. The pumping rate initially was 11 gpm and changed based on pump capability to maintain the minimum rate. K-formate was injected in the downstream line and ice started to melt out after 17 minutes of pumping at a temperature of 62 °F, Fig. 8.

**Upstream Injection of (K-formate):** The experiment was repeated by generating the hydrate again and dropping the pipe temperature to 35 °F. The injection of K-formate was performed in the upstream section before the choke. The pumping rate was maintained at 22 gpm and continued until the end of the test. Ice was melted down within 6 minutes of pumping and the temperature increased rapidly to 58 °F, Fig. 9.

**Field Observation**

Several samples were collected during the flow back process. The samples collected showed the formation of emulsion along with suspended gas bubbles into the solution. The gas was segregating very slowly from the solution and complete separation took 30 minutes, Fig. 10.

**Test Trial 2**

Upon the success of K-formate in dissolving hydrate crystals, consistent pumping capability was a challenge. The outcome of the first field trial revealed one main outcome: using the backside pump with its high injection rate (11 gpm) was successful, but gas in brine emulsion was observed with some difficulties when it comes to flaring. Utilizing the backside pump to inject the chemical is not safe as a long-term solution.

In the second field trial, two pumps were tested to check the capability of the pumps and the minimum rate
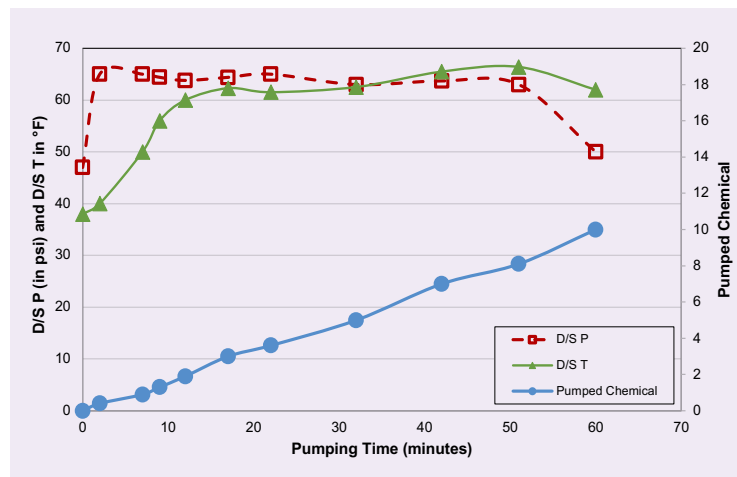
**Fig. 7** *Ice formed on the pipeline, indicating the formation of gas hydrate.*



**Fig. 8** *The summary of test results; pressure, temperature, and volume of treatment. The data indicates that after 17 minutes from the start of injection of K-formate at a rate of 11 gpm, the temperature increased from 38 °F to 62 °F, indicating full dissolution of the gas hydrate plug.*

**Fig. 9** *The summary of test results; pressure, temperature, and volume of treatment. The data indicates that after 6 minutes from the start of injection of K-formate at a rate of 22 gpm, the temperature increased from 34 °F to 58 °F, indicating full dissolution of the gas hydrate plug.*
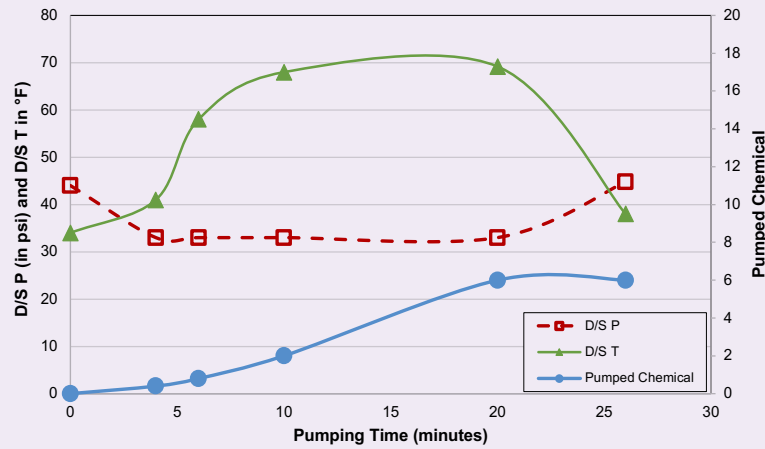


**Fig. 10** *The gas in treatment emulsion.*



required to raise the stream temperature to the hydrate dissolving temperature limit. The two pumps tested have plunger sizes of 28 mm and 40 mm with 0.12- and 0.25-liter volume per stroke, respectively. The flow rate range for the 28 mm plunger pump was between 3.1 to 16.0 liters/min, while for the 40 mm plunger pump the flow rate range was 6.6 to 32.5 liters/min. Both pumps were tested in this field trial.

**Positive Displacement Pump (28 mm plunger):** The well was shut-in for 4 hours to build up pressure, then it was opened to flow at choke size 12/64". With a pressure drop of almost 2,000 psi, the stream temperature dropped to 49 °F. At this temperature, gas hydrate started to form a plug inside the pipeline. K-formate feed was connected to the 28 mm plunger piston pump, and the treatment fluid was injected at an estimated rate of 2.4 gal/min.

After pumping 24 gallons of treatment, the stream temperature increased by 10° in 10 minutes. Injection of the K-formate continued for an interval of time of about 30 minutes, where 72 gallons of treatment were injected, and the temperature increased from 38 °F to 65 °F, indicating a complete hydrate dissolution.

## Conclusions

1. Visual cell equipped with a stirrer and torque measuring transducer was used to test the formation and dissolution of gas hydrate plugs.

2. Both field gas and formation brine composition were used in the tests.

3. The experiments were performed at conditions similar to field conditions.

4. Four alternatives with a higher flash point than methanol were tested and proved efficient in dissolving/melting the gas hydrate plug.

5. Two solvent-based, namely DEGEE and 2-BE, and two aqueous-based chemical formulations, namely K-formate and heated K-formate, were tested for dissolving gas hydrates.

6. All alternatives were able to dissolve hydrate at similar or lower dosage in comparison to methanol and in a shorter time.

7. Two field trials were performed to evaluate the performance of one of the developed formulations (K-formate). At similar injection rate to methanol, the K-formate was able to dissolve gas hydrate plugs in less time and smaller volume (30 minutes and 72 gallons pumped of K-formate) compared to methanol (120 minutes and 180 gallons of methanol).

8. The success of the field trials proved K-formate to be a safer and more efficient alternative to replace methanol as a gas hydrate dissolver.

# References

1. Sloan Jr., E.D. and Koh, C.A.: *Clathrate Hydrates of Natural Gases*, 3rd edition, Boca Raton, FL: CRC Press, 2007, 752 p.

2. Mokhatab, S., Wilkens, R.J. and Leontaritis, K.J.A.: "A Review of Strategies for Solving Gas-Hydrate Problems in Subsea Pipelines," *Energy Sources, Part A: Recovery Utilization and Environmental Effects*, Vol. 29, Issue 1, January 2017, pp. 39-45.

3. Majid, A.A., Lee, W., Srivastava, V., Chen, L., et al.: "Experimental Investigation of Gas-Hydrate Formation and Particle Transportability in Fully and Partially Dispersed Multiphase Flow Systems Using a High-Pressure Flow Loop," *SPE Journal*, Vol. 23, Issue 3, June 2018, pp. 937-951.

4. Zhao, H., Sun, M. and Firoozabadi, A.: "Anti-Agglomeration of Natural Gas Hydrates in Liquid Condensate and Crude Oil at Constant Pressure Conditions," *Fuel*, Vol. 180, September 2016, pp. 187-193.

5. Neto, E.T.: "A Mechanistic Computational Fluid Dynamic (CFD) Model to Predict Hydrate Formation in Offshore Pipelines," SPE paper 184491, presented at the SPE Annual Technical Conference and Exhibition, Dubai, UAE, September 26-28, 2016.

6. Dai, Z., Luo, D. and Liang, W.: "Gas Hydrate Prediction and Prevention during DST in Deep Water Gas Field in South China Sea," SPE paper 177629, presented at the Abu Dhabi International Petroleum Exhibition and Conference, Abu Dhabi, UAE, November 9-12, 2015.

7. Kamal, M.S., Hussein, I.A., Sultan, A.S. and von Solms, N.: "Application of Various Water-Soluble Polymers in Gas Hydrate Inhibition," *Renewable and Sustainable Energy Reviews*, Vol. 60, July 2016, pp. 206-225.

8. Fonte, S.S.D., Simonelli, G. and Santos, L.C.L.: "A Review of the Main Techniques to Avoid the Formation of Hydrate," *Brazilian Journal of Petroleum and Gas*, Vol. 12, Issue 1, 2018, pp. 61-73.

9. Stoisits, R.F., Lucas, D.C., Talley, L.D., Shatto, D.P., et al.: "Method for Managing Hydrates in Subsea Production Line," International Patent Application WO/2009/042319, 2009.

10. Harris, R.G. and Clapham, J.: "Britannia's Heated Bundles Inhibit Hydrate Formation," *Offshore*, Vol. 59, Issue 2, 1999.

11. Urdahl, O., Boernes, A.H., Kinnari, K.J. and Holme, R.: "Operational Experience by Applying Direct Electrical Heating for Hydrate Prevention," *SPE Production & Facilities*, Vol. 19, Issue 3, August 2004, pp. 161-167.

12. Ghazal, A.A., Gad, F.K., Aawad, M.S., Desouky, S.M., et al.: "Thermal Insulation for Hydrate Prevention in Pipeline Design," *Egyptian Journal of Chemistry*, Vol. 59, Issue 4, August 2016, pp. 465-479.

13. Kinnari, K.J., Labes-Carrier, C., Lunde, K. and Aaberge, L.: "Method of Inhibiting Hydrate Formation," International Patent Application WO/2006/027609, 2006.

14. Mokhatab, S., Poe, W.A. and Speight, J.G.: *Handbook of Natural Gas Transmission and Processing*, Gulf Professional Publishing, 2006, 628 p.

15. Motghare, P.D. and Musale, A.: "Unconventional Hydrocarbons: Gas Hydrates — Drilling Challenges and Suitable Technology," SPE paper 185424, presented at the SPE Oil and Gas India Conference and Exhibition, Mumbai, India, April 4-6, 2017.

16. Huff, T., Cook, S., Trebing, R., Glover, M., et al.: "Simple and Cost-Effective Hydrate Prevention for Flowback After Hydraulic Fracturing: Kinetic Hydrate Inhibitor (KHI)/Methanol Mixture," SPE paper 166364, presented at the SPE Annual Technical Conference and Exhibition, New Orleans, Louisiana, September 30-October 2, 2013.

17. Salmin, D.C., Majid, A.A., Wells, J., Sloan Jr., E.D., et al.: "Study of Anti-Agglomerant Low Dosage Hydrate Inhibitor Performance," OTC paper 27911, presented at the Offshore Technology Conference, Houston, Texas, May 1-4, 2017.

18. Tian, J. and Garza, T.Z.: "Method of Transitioning to Kinetic Hydrate Inhibitors in Multiple Tie-In Well Systems," International Patent Application WO/2010/011804, 2010.

19. Anderson, R., Chapoy, A., Tanchawanich, J., Haghighi, H., et al.: "Binary Ethanol-Methane Clathrate Hydrate Formation in the System $CH_4$-$C_2H_5OH$-$H_2O$: Experimental Data and Thermodynamic Modeling," paper presented at the 6th International Conference on Gas Hydrates Vancouver, British Columbia, Canada, July 6-10, 2008.

20. Awbrey, S.S. and Riney, H.C.: "Methods for Using Material from Biodiesel Production in Hydrocarbon Production and Refining," U.S. Patent Application 20090149683, 2009.

21. Kaasa, B. and Billington, P.H.: "Process for Hydrate Inhibitor Regeneration," International Patent Application WO/2010/084323, 2010.

22. Yousif, M.H.: "Effect of Under Inhibition with Methanol and Ethylene Glycol on the Hydrate Control Process, *SPE Production & Facilities*, Vol. 13, Issue 3, August 1998, pp. 184-189.

23. Li, X., Hemmingsen, P.V. and Kinnari, K.: "Use of Under-Inhibition in Hydrate Control Strategies," paper presented at the 7th International Conference on Gas Hydrates, Edinburgh, Scotland, U.K., July 17-21, 2011.

24. Falana, O.M., Morrow, M. and Zamora, F.G.: "Gas Hydrate Inhibitors and Methods for Making and Using Same," U.S. Patent Application 20130178399, 2013.

25. Carroll, J.: *Natural Gas Hydrates: A Guide for Engineers*, Amsterdam: Gulf Professional Publishing, 2014, 319 p.

26. Bavoh, C.B., Partoon, B., Lal, B. and Keong, L.K.: "Methane Hydrate-Liquid-Vapor-Equilibrium Phase Condition Measurements in the Presence of Natural Amino Acids," *Journal of Natural Gas Science and Engineering*, Vol. 37, January 2017, pp. 425-434.

27. Tomson, M.B., Kan, A.T. and Fu, G.: "Inhibition of Barite Scale in the Presence of Hydrate Inhibitors," *SPE Journal*, Vol. 10, Issue 3, September 2005, pp. 256-266.

28. Masoudi, R., Tohidi, B., Danesh, A., Todd, A.C., et al.: "Measurement and Prediction of Salt Solubility in the Presence of Hydrate Organic Inhibitors," *SPE Production & Operations*, Vol. 21, Issue 2, May 2006, pp. 182-187.

29. Rodríguez Gonzáles, R. and Djuve, J.: "Hydrate Inhibitors," International Patent Application WO/2010/101477, 2010.

30. Arjmandi, M., Tohidi, B., Danesh, A. and Todd, A.C.: "Is Subcooling the Right Driving Force for Testing Low-Dosage Hydrate Inhibitors?" *Chemical Engineering Science*, Vol. 60, Issue 5, March 2005, pp. 1313-1321.

31. Kelland, M.A., Moenig, K., Iversen, J.E. and Lekvam, K.: "Feasibility Study for the Use of Kinetic Hydrate Inhib-

itors in Deep-Water Drilling Fluids," *Energy & Fuels*, Vol. 22, Issue 4, 2008, pp. 2405-2410.

32. Nazeri, M., Tohidi, B. and Chapoy, A.: "An Evaluation of Risk of Hydrate Formation at the Top of a Pipeline," *Oil and Gas Facilities*, Vol. 3, Issue 2, April 2014, pp. 67-72.

33. Creek, J.L.: "Efficient Hydrate Plug Prevention," *Energy & Fuels*, Vol. 26, Issue 7, 2012, pp. 4112-4116.

34. Phillips, N.J. and Grainger, M.: "Development and Application of Kinetic Hydrate Inhibitors in the North Sea," SPE paper 40030, presented at the SPE Gas Technology Symposium, Calgary, Alberta, Canada, March 15-18, 1998.

35. Varma-Nair, M., Costello, C.A., Colle, K.S. and King, H.E.: "Thermal Analysis of Polymer-Water Interactions and Their Relation to Gas Hydrate Inhibition," *Journal of Applied Polymer Science*, Vol. 103, Issue 4, February 2007, pp. 2642-2653.

36. Long, J., Lederhos, J., Christiansen, R.L. and Sloan Jr., E.D.: "Kinetic Inhibitor of Natural Gas Hydrates," paper presented at the 73rd Annual GPA Convention, New Orleans, Louisiana, March 7-9, 1994.

37. Sloan Jr., E.D.: "Method for Controlling Clathrate Hydrates in Fluid Systems," U.S. Patent 5,420,370, 1995.

38. Szymczak, S., Sanders, K.B., Pakulski, M.K. and Higgins, T.D.: "Chemical Compromise: A Thermodynamic and Low Dose Hydrate Inhibitor Solution for Hydrate Control in the Gulf of Mexico," *SPE Project Facilities & Construction*, Vol. 1, Issue 4, December 2006, pp. 1-5.

39. Huang, B., Wang, Y., Zhang, S. and Ao, Y.: "Kinetic Model of Fixed Bed Reactor with Immobilized Microorganisms for Removing Low Concentration $SO_2$," *Journal of Natural Gas Chemistry*, Vol. 16, Issue 1, March 2007, pp. 81-91.

40. Klomp, U.C. and Mehta, A.P.: "Validation of Kinetic Inhibitors for Sour Gas Fields," IPTC paper 11374, presented at the International Petroleum Technology Conference, Dubai, UAE, December 4-6, 2007.

41. Mady, M.F., Bak, J.M., Lee, H-I. and Kelland, M.A.: "The First Kinetic Hydrate Inhibition Investigation on Fluorinated Polymers: Poly(fluoroalkylacrylamide)s," *Chemical Engineering Science*, Vol. 119, November 2014, pp. 230-235.

42. Da Silveira, K.C., Sheng, Q., Tian, W., Fong, C., et al.: "High Throughput Synthesis and Characterization of PNIPAM-Based Kinetic Hydrate Inhibitors," *Fuel*, Vol. 188, February 2017, pp. 522-529.

43. Davies, S.R., Boxall, J.A., Koh, C.A., Sloan Jr., E.D., et al.: "Predicting Hydrate Plug Formation in a Subsea Tieback," SPE paper 115763, presented at the SPE Annual Technical Conference and Exhibition, Denver, Colorado, September 21-24, 2008.

*About the Authors*

**Dr. Mohammed A. Sayed**

*Ph.D. in Petroleum Engineering, Texas A&M University*

Dr. Mohammed A. Sayed joined the Production Technology Team at the Aramco Research Center-Houston as a Research Scientist in 2013. In this role, he is working to develop new chemical treatments and fluids used in acidizing carbonate reservoirs (matrix acidizing and acid fracturing). Mohammed is also creating new fluids utilized for hydraulic fracturing in both conventional and unconventional reservoirs, acidizing additives and wettability alteration chemicals, and breakers for polymer systems used in fracturing fluids, as well as developing new solutions for gas hydrate removal and mitigation. He is also responsible for assisting in the preparation and follow-up on programs for workover operations, well testing, well acidizing and stimulation treatments, as well as preparing reports on assigned projects or programs in the oil field operations.

Mohammed is a contributor to technical papers and is a member of the Society of Petroleum Engineers (SPE) as well as the American Chemical Society (ACS). He has presented at various industry conferences, including the Offshore Technology Conference (OTC), Middle East Oil and Gas Show (MEOS), and the International Conference on Oil Field Chemistry, as well as publishing peer-reviewed papers in the *Canadian Journal of Petroleum Technology*, SPE *Production and Operation Journal* and *Advances in Water Resources*.

Mohammed received his Ph.D. degree in Petroleum Engineering from Texas A&M University, College Station, TX.

**Dr. Rajesh K. Saini**

*Ph.D. in Organic Chemistry,
Kurukshetra University*

Dr. Rajesh K. Saini is a Research Science Specialist in the Production Technology Team at the Aramco Research Center-Houston. He has more than 24 years of experience in the oil and gas industry, and chemical research. Rajesh is a subject matter expert in oil field stimulation, production and operations technology. He specializes in product development, scaling up, intellectual property, sales and commercialization of new products/processes for hydraulic fracturing, sand control, acidizing, production technology, oil field chemicals, and water conformance. Prior to joining Aramco in 2017, Rajesh played critical roles at Halliburton, Weatherford, and Lubrizol in the capacity from Research Scientist to R&D Manager.

He has served as a technical reviewer for major journals, including the *Journal of American Chemical Society,* and the *Journal of Organic Chemistry and Organic Letters.* Rajesh is a Technical Editor for the Society of Petroleum Engineers (SPE) *Production and Operations*

*Journal.* He is serving on the SPE Annual Technical Conference and Exhibition (ATCE) well stimulation committee. Rajesh holds 54 U.S. patents, 21 U.S. patent applications, and has published one book chapter and 48 peer-reviewed journal articles.

He served as the Distinguish Lecture's Program Chair and Director of the SPE-Southwest Oklahoma Section during 2009-2012. Rajesh received the Maximizing Value-Added Performance (MVP) award at Halliburton for developing environmental fracturing fluid (CleanStim®) and breaker for AquaLinear® fluid. In 2018, he was also awarded the SPE Gulf Coast Regional award for Production and Operations.

Rajesh received his MBA from Oklahoma State University, Stillwater, OK, and his Ph.D. degree in Organic Chemistry from Kurukshetra University, Haryana, India. He was a postdoctoral fellow at Rice University working with Prof. W.E. Billups and Richard E. Smalley (Nobel Laureate in Chemistry).

**Eyad A. Alali**

*B.S. in Petroleum Engineering,
University of Oklahoma*

Eyad A. Alali is a Petroleum Engineer working in the Production Technology Division (PTD) of Saudi Aramco's Exploration and Petroleum Engineering Center – Advanced Research Center (EXPEC ARC). He joined Saudi Aramco in 2015, and has since worked with gas reservoir management, gas production engineering, and a field trial team in the PTD. Eyad is currently working with the Productivity Enhancement Team in PTD.

Eyad's experience includes work in a portfolio of projects focused on developing new technologies in hydraulic fracturing and carbonate stimulation.

He is a member of the Society of Petroleum Engineers (SPE).

Eyad received his B.S. degree with distinction in Petroleum Engineering from the University of Oklahoma, Norman, OK.

**Dr. Rajendra A. Kalgaonkar**

*Ph.D. in Polymer Chemistry and
Nanotechnology,
University of Pune*

Dr. Rajendra A. Kalgaonkar is a Petroleum Scientist in the Productivity Enhancement Focus Area of the Production Technology Team at Saudi Aramco's Exploration and Petroleum Engineering Center – Advanced Research Center (EXPEC ARC). He has over 19 years of experience in Research and Development, out of which he spent 11 years in the upstream oil and gas industry. Prior to joining Saudi Aramco in May 2015, Rajendra worked as a Technology Leader with Halliburton. He has rich experience in areas of nanotechnology; polymer blends and composites while being associated with the National Chemical Laboratory, India, and the University of Western Sydney, Australia.

Rajendra's research is focused on developing

new fluids technologies for enhancing hydrocarbon production, including fracturing, sand control, conformance control and acidizing. He has successfully developed new chemistries based on nanomaterials for enhancing hydrocarbon production as well as for drilling fluids.

Rajendra has published 25 patents and patent applications, and 35 peer-reviewed articles, invited book chapters and conference proceedings. He has delivered presentations at Society of Petroleum Engineers (SPE) key advanced technology workshops and forums.

Rajendra received his B.S. degree in Chemistry, an M.S. degree in Polymer Science, and his Ph.D. degree in Polymer Chemistry and Nanotechnology, all from the University of Pune, Pune, India.

**Ahmed B. Al-Arnous**

*Management and Business
Administration,
King Faisal University*

Ahmed B. Al-Arnous is an Operation Excellence group leader working in Saudi Aramco's Southern Area Well Completion Operations Department, where he introduces more technologies and enhancements to well intervention safety and efficiency.

Ahmed has more than 10 years of experience in production engineering, unconventional gas

resources, and well intervention operations.

He received his B.S. degree in Petroleum Engineering from the University of Manchester, Manchester, U.K., and his M.S. degree in Management and Business Administration (MBA) from King Faisal University, Hofuf, Saudi Arabia.

## About the Authors

**Dr. Ping Zhang**

*Ph.D. in Geophysics,
Uppsala University*

Dr. Ping Zhang joined Schlumberger in 1999 as a Principal Geophysicist. He retired in 2021. Ping started his career as an Assistant Researcher at the University of Montreal, Montreal, Canada, from 1990 to 1994, and an Area Geophysicist for Inco Ltd., a mining company in Canada from 1995 to 1998.

His research focused on the application of electromagnetic (EM) technologies for geophysical exploration and characterization, with an emphasis on developing numerical techniques that are used for interpretation of EM data.

Ping worked on cross-well EM data quality control, processing, inversion and interpretation for petroleum applications. He was also actively involved in studies and development for reservoir monitoring and characterization.

Ping has published more than 50 peer-reviewed conference papers and holds 12 granted U.S. patents. He is a member of the Society of Petroleum Engineers (SPE), the Society of Petrophysicists and Well Log Analysts, and the Society of Exploration Geophysicists.

In 1989, Ping received his Ph.D. degree in Geophysics from Uppsala University, Uppsala, Sweden.

**Dr. Wael Abdallah**

*Ph.D. in Chemical Engineering,
University of Alberta*

Dr. Wael Abdallah joined Schlumberger in 2005 as a Research Scientist at the DBR Technology Center, Edmonton, Canada. He is currently the Managing Director of Schlumberger's Dhahran Carbonate Research Center in Saudi Arabia. Wael's research focuses on interfacial science for better downhole reservoir characterization, while also actively investigating better petrophysical reservoir characterization using multiphysics.

Prior to this assignment, he was the Program Manager for the geology, rock physics, and recovery research activities within the same center. Wael also managed commercial services related to reservoir fluids phase behavior and flow assurance. He also worked as an instructor with the NeXT technical training team on reservoir fluids.

In 2005, Wael received the Alberta Ingenuity Award.

He has published and coauthored more than 70 peer-reviewed conference papers, in addition to having 15 granted U.S. patents.

Wael is a member of the Society of Petroleum Engineers (SPE) and the Society of Petrophysicists and Well Log Analysts. He holds a professional Engineering Status in Canada.

Wael received both his B.S. and M.S. degrees in Chemical Engineering from the Jordan University of Science and Technology, Irbid, Jordan, majoring in fluid phase behavior and thermodynamics.

In 2005, he received his Ph.D. degree in Chemical Engineering from the University of Alberta, Edmonton, Canada, majoring in heterogeneous catalysis and surface science.

**Dr. Gong Li Wang**

*Ph.D. in Applied Geophysics,
China University of Petroleum*

Dr. Gong Li Wang is a Principal Modeling and Simulation Engineer at the Schlumberger Houston Formation Evaluation Center. He works on electromagnetic logging answering product development, and provides internal and external support on induction tools, including triaxial induction, array induction and through bit induction.

Gong was cited in the top 25 of all papers in the 2018 Society of Exploration Geophysicists (SEG) annual meeting for his work on induction logging in triaxially anisotropic formations. Prior to joining Schlumberger, he worked with the University of Illinois at Urbana-Champaign on computational electromagnetics and acoustics, and the University of Texas at Austin on electromagnetic logging and multiphysics inversion from 2002 to 2008.

Gong started his career with the China University of Petroleum, Shandong, China, where he worked on electromagnetic logging from 1993 to 2002.

In 1993, he received his B.S. degree in Borehole Geophysics, and a Ph.D. degree in Applied Geophysics in 2001 from the China University of Petroleum, Beijing, China.

**Dr. Shouxiang M. Ma**

*Ph.D. in Petroleum Engineering,
New Mexico Institute of Mining
and Technology*

Dr. Shouxiang M. "Mark" Ma is a Senior Petroleum Engineer Consultant overseeing research and development, subject matter technical support, and professional development in the Advanced Petrophysical Modeling Group of Saudi Aramco's Reservoir Description and Simulation Department. Prior to this, he was Supervisor of the Petrophysical Support & Study Unit, advisor at the Upstream Professional Development Center, and Lead Petrophysicist for logging operations.

Before joining Saudi Aramco in 2000, Mark worked at the Exxon Production Research Company, Wyoming Western Research Institute, New Mexico Petroleum Recovery Research Center, and China Yangtze University.

He served as a chairperson of the 2013 Society of Petroleum Engineers (SPE) Formation Evaluation Award Committee, the 2018 SPE Annual Technical Conference and Exhibition Formation Evaluation Committee, and on the 2019 International Petroleum Technology Conference Education Week Conference.

Mark was awarded the 2019 SPE MENA Formation Evaluation Award.

From 2015 to 2020, he served on the *JPT* Editorial Board where he was responsible for formation evaluation content. Mark is a Society of Petrophysicists and Well Log Analysts (SPWLA) Saudi Arabia Chapter vice president for technical events, and from 2018 to 2020, he was a SPWLA Director representing the Middle East and Africa region. Mark is also an Associate Editor for the *Journal of Petrophysics*, and Vice President of the SPWLA Saudi Arabia Chapter.

He received his B.S. degree from the China University of Petroleum, Shandong, China, and his M.S. and Ph.D. degrees from the New Mexico Institute of Mining and Technology, Socorro, NM, all in Petroleum Engineering.

# Photoacoustic Nanotracers for Subsurface Applications: Opportunities and Challenges

*Jesus M. Felix Servin, Hala A. AlSadeg and Dr. Amr I. Abdel-Fattah*

**Abstract /**

Tracers are practical tools used to gather information about the subsurface fluid flow in hydrocarbon reservoirs. Typical interwell tracer tests involve injecting and producing tracers from multiple wells to evaluate important parameters such as connectivity, flow paths, fluid-fluid and fluid-rock interactions, and reservoir heterogeneity, among others. The use of nanotechnology enables the development of novel nanoparticle-based tracers to overcome many of the challenges faced by conventional tracers. Among the advantages of nanoparticle-based tracers is the capability to functionalize their surface to yield stability and transportability through the subsurface. In addition, nanoparticles can be engineered to respond to a wide variety of stimuli, including light.

The photoacoustic effect is the formation of sound waves following light absorption in a material sample. The medical community has successfully employed photoacoustic nanotracers as contrast agents for photoacoustic tomography imaging. We propose that properly engineered photoacoustic nanoparticles can be used as tracers in oil reservoirs. Our analysis begins by investigating the parameters controlling the conversion of light to acoustic waves, and strategies to optimize such parameters.

Next, we analyze different types of nanoparticles that we deem potential candidates for our subsurface operations. Then, we briefly discuss the excitation sources and make a comparison between continuous wave and pulsed sources. We finish by discussing the research gaps and challenges that must be addressed to incorporate these agents into our operations.

At the time of this writing, no other study investigating the feasibility of using photoacoustic nanoparticles for tracer applications was found. Our work paves the way for a new class of passive tracers for oil reservoirs. Photoacoustic nanotracers are easy to detect and quantify, and are therefore suitable for continuous in-line monitoring, contributing to the ongoing real-time data efforts in the oil and gas industry.

## Introduction

Tracer technology has shown to be efficient in collecting underground information, which is important in the process of oil and gas development. Interwell tracer tests offer the most direct method for investigating fluid flow paths between injector and producer wells. These tracer tests allow us to obtain a better understanding of reservoir heterogeneity by identifying the wells contributing to oil production as opposed to the one's fluid cycling, which is critical for reservoir water management.

Until now, primarily fluorescent and chemical tracer signatures have been used to detect and quantify tracers in solution. While fluorescence measurements are relatively simple, some of the hydrocarbons and contaminants present in the produced fluids are fluorescent too, and that complicates an accurate detection and quantification. Chemically labeled tracers can be quantified accurately but require complex instrumentation and separation procedures, e.g., gas chromatography-mass spectrometry measurements, making it hard to develop a system for in-line detection.

In this article, we introduce nanomaterials that have been extensively studied and successfully implemented for biomedical imaging that we deem promising as a new class of tracers for use in the oil and gas sector. These nanoparticles generate sound upon illumination with light due to a well-described physical phenomenon known as the photoacoustic effect. While excitation is achieved via a light source, e.g., a laser, detection is accomplished by acoustic transducers — typically in the ultrasonic range. Therefore, this method retains the detection simplicity of fluorescent tracers while addressing the challenge associated with background fluorescence.

In the following sections, we present the theory behind the photoacoustic effect, the classes of nanoparticles that we consider relevant for oil and gas operations, as well as the available sources for illumination. Finally, we discuss the research gaps and challenges that need to be addressed to enable the incorporation of this technology into our operations.

## The Photoacoustic Effect

The photoacoustic effect is the formation of sound waves following light absorption by a material sample. Alexander

Graham Bell was the first to discover this phenomenon in the late 1800s while investigating the feasibility of speech transmission via light[1]. This approach was abandoned in favor of other methods, such as radio transmissions. It was in the 1960s, with the development of the laser, that the interest on the photoacoustic effect was revived. The initial interest focused on gas analysis but eventually expanded to solids and liquids as well.

The generation of sound upon illumination can be accomplished through multiple mechanisms, including:

- Radiation pressure: The mechanical pressure experienced by the sample due to the exchange of momentum of the light. The effects of this mechanism are considered weak for most applications, and are therefore ignored.

- Electrostriction: This refers to the change in shape of a dielectric material in the presence of an electric field. The deformation is due to the displacement of ions when exposed to an external electric field. Positive ions will move in the direction of the field, and negative ions will move in the opposite direction. The net result is an elongation of the sample in the direction of the field. This effect is only relevant in liquid samples with very weak optical absorption or with a high electrostrictive coefficient[2].

- Dielectric breakdown: This refers to the acoustic signal generated when samples are irradiated with high intensity light, resulting on the breakdown of the dielectric properties of the sample and plasma generation[3].

- Thermoelastic expansion: Upon illumination with a modulated light source, the sample momentarily stores some of the incident energy. In the absence of radiative methods, the energy is released in the form of heat, which causes an increase in volume.

- Vaporization: This occurs in liquids that are superheated due to the absorption of intense radiation. As a result, the sample abruptly changes from a liquid state to a gas state, generating a high amplitude acoustic signal in the process[4].

- Biological processes: Certain biological processes such as the photosynthesis in plant leaves[5] and the

Bacteriorhodopsin proton pump[6, 7] have been shown to generate photoacoustic signals.

In this work, we will focus on the thermoelastic expansion and explosive vaporization mechanisms, as we consider them the most applicable for subsurface characterization. Figure 1 shows a schematic representation of how photoacoustic signals are generated via these two mechanisms. We focus our efforts on the photoacoustic signals generated by liquid samples because they are the most relevant for oil and gas operations.

## Theory of Photoacoustic Signals in Liquid Samples

A simple, yet useful, theory of how photoacoustic signals are generated in liquids via thermoelastic expansion was provided by Patel et al. (1981)[8]. According to Beer's law, upon illumination, the amount of energy transmitted is described by Eqn. 1.

$$E_t = E_0 e^{-\alpha l} \qquad 1$$

where $E_t$ is the transmitted energy, $E_0$ is the incident energy, $\alpha$ is the optical absorption coefficient, and $l$ is the optical path length. Assuming no losses (reflective or scattering), the energy absorbed by the sample can be quantified using Eqn. 2.

$$\Delta E = E_0 - E_t \qquad 2$$

For the case of weak optical absorption ($\alpha l \ll 1$), Eqn. 2 can be simplified to the following expression:

$$\Delta E \approx E_0 \alpha l \qquad 3$$

The temperature rise, due to the absorbed energy, assuming no other energy release mechanisms are present, can be estimated using Eqn. 4.

$$\Delta T = \frac{E_0 \alpha l}{\rho c_p V} \qquad 4$$

where $\rho$ is the sample density, $C_\rho$ is the specific heat capacity, and $V$ is the absorbed volume. At this point, there are two possible scenarios depending on the duration of the light pulse ($\tau_p$) relative to the time it takes for an acoustic wave to travel across the illuminated volume ($\tau_a$).

When $\tau_p \gg \tau_a$, the illuminated volume has enough

---

**Fig. 1** *A schematic representation of the generation of photoacoustic signals via thermoelastic expansion (left) and vaporization (right).*
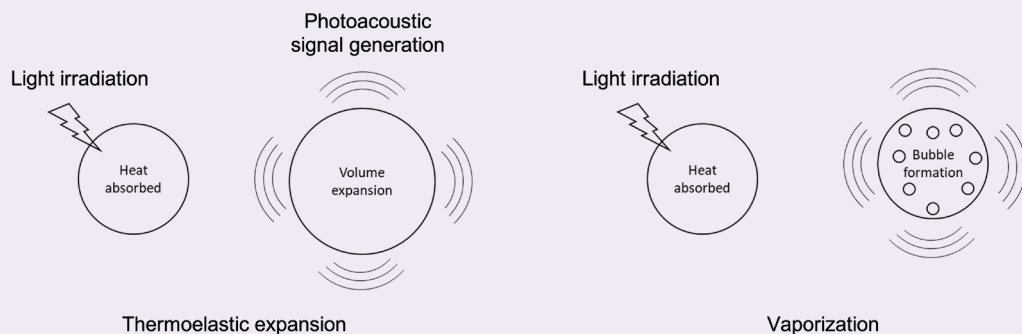
time to expand during the light pulse. In this case, the magnitude of the pressure pulse generated due to thermoelastic expansion can be approximated by Eqn. 5:

$$|p| \approx k \frac{\beta \alpha}{C_p} \left(\frac{v}{r}\right)^{\frac{1}{2}} E_0 \qquad 5$$

where $k$ is a system constant that includes temporal factors related to the pressure waveform generation, $\beta$ is the volumetric thermal expansion, $v$ is the speed of sound in the medium of interest, and $r$ is the radial distance.

If $\tau_p << \tau_a$, the illuminated volume does not have enough time to expand. Therefore, the pressure increase happens at the edge of the illuminated volume. Under this condition, the magnitude of the pressure pulse can be approximated by Eqn. 6:

$$|p| \approx \frac{1}{\pi R^{\frac{2}{3}}} \frac{\beta \alpha}{C_p} \frac{v^2}{r^{\frac{1}{2}}} E_0 \qquad 6$$

where $R$ is the radius of the optical beam.

The equations provided here are a good guide to qualitatively compare the magnitude of the acoustic signals generated under multiple conditions; however, the time dependence of the wave is ignored. The shape of the waveform has important implications on the design of the acoustic detector. Lai et al. (1982)[9] provided an understanding of the implications of the time dependence of the photoacoustic signal as follows:

$$|p(r,t)| \propto \frac{\beta \, \alpha \, E_0}{8 \sqrt{\pi} \, C_p} \left(\frac{v}{r}\right)^{\frac{1}{2}} \tau_e^{-3/2} \qquad 7$$

where $\tau_e$ is an effective time parameter that depends on the light pulse duration ($\tau_p$), and the acoustic transient time ($\tau_a$) as described by Eqn. 8.

$$\tau_e = \left(\tau_p^2 + \tau_a^2\right)^{1/2} \qquad 8$$

From the approximations presented, we can make important conclusions about how to maximize the amplitude of the photoacoustic signals. Materials with high volumetric expansion, optical absorption and acoustic velocity, and low specific heat capacity are desirable. The time dependence suggests that narrow beams and short pulses increase the amplitude of the photoacoustic signal. A second reason to use narrow beams is to prevent non-coherent contributions from different regions of the beam reaching the detectors simultaneously and altering the signal.

The equations previously presented are derived for liquids, but we think the most promising applications within the oil and gas industry are in the form of photoacoustic nanoparticles suspended in liquids that serve as tracers. It is reasonable to assume that some of the desirable properties for liquids apply to nanoparticles too. As such, nanoparticles with high volumetric expansion and optical absorption, and low specific heat capacity are desirable.

## Photoacoustic Nanoparticles

The use of photoacoustics in the oil and gas industry is rather limited, but there are some examples available. For instance, some prototypes have been developed to explore the feasibility of monitoring oil content in treated/separated water from oil-water separators[10, 11]. Monitoring the presence of biofilms in produced water pipelines via photoacoustic measurements has also been investigated[12]. At the moment of this writing, no literature was found evaluating the feasibility of using photoacoustic nanoparticles as tracers to improve subsurface characterization.

Tracers are practical tools to gather information about the subsurface fluid flow in hydrocarbon reservoirs. Typical interwell tracer tests involve injecting and producing tracers from multiple wells to evaluate important parameters such as connectivity, flow paths, fluid-fluid and fluid-rock interactions, and reservoir heterogeneity, among others. For this purpose, passive tracers are the preferable choice and include radioactive, inorganic elements, alcohols, fluorescent molecules and fluorinated benzoic acids, all bearing advantages and disadvantages.

Fluorescent tracers are appealing because conducting fluorescence measurements is relatively simple, and therefore, an in-line system for permanent monitoring could be developed. Subsequently, such tracers have two major disadvantages: the background fluorescence of the produced fluids interferes with the tracer detection, and fluorescent tracers are prone to photobleaching over time. Tracers based on photoacoustic nanoparticles have the potential to overcome both of these challenges, while offering a simple and reliable detection method. Nanoparticles can be engineered to have narrow absorption peaks, and therefore, avoid background noise by illuminating with a narrow spectra light source, such as a laser. In addition, the detection is based on the measurement of acoustic signals that, unlike fluorescent signals, are not affected by diffraction nor by photobleaching.

While photoacoustic nanoparticles have not been used in the past for subsurface applications, they have been extensively used in medical and biomedical applications as contrast agents for photoacoustic tomography imaging[13]. For nanoparticles to be used as subsurface tracers, there is a list of desired properties that include stability, transportability, cost-effectiveness, low limit of quantification, linear concentration dependence, and to a lesser extent multiplexing. By conducting a literature research, we have found two large categories of nanoparticles that appear to be good candidates for photoacoustic nanoparticle-based subsurface tracers.

### Solid Nanoparticles

Solid nanoparticles have been widely used as contrast agents in photoacoustic imaging for biological applications based on their high and stable signal, and because their surface can be functionalized. Metallic nanoparticles are most commonly used as photoacoustic contrast agents because of their high absorption cross section, which is a measure of the ability of the nanoparticle to absorb a photon of a specific wavelength and polarization[13]. In addition, their size and shape can be modified to tune the absorption peak for multiplexing.

Figure 2 shows the peak absorption of commercially available gold nanoparticles as a function of their size. It can be clearly seen that it is possible to tune their size to obtain nanotracers that respond to different excitation wavelengths. Other important considerations for

**Fig. 2** *The peak absorption wavelength of commercially available gold nanoparticles as a function of their diameter. The plot clearly shows how their size can be tuned to obtain nanotracers that are triggered by different wavelengths.*
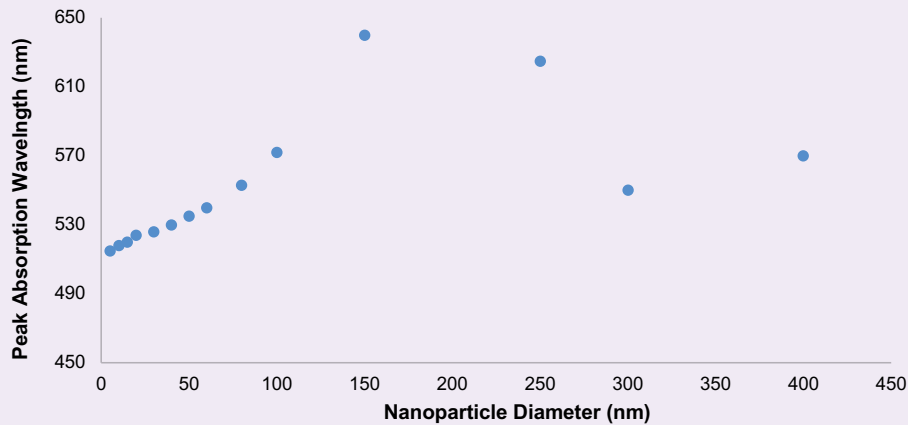


contrast agents include the lower limit of quantification, linear concentration dependence, high selectivity, and multimodality as a key parameter for verification and validation of signal reliability[14].

One of the commonly studied contrast agents to assist quantitative flow estimation in photoacoustic imaging is gold nanoparticles[15]. An advantage of using gold nanoparticles is that they exhibit strong photoacoustic response to invisible to near infrared ranges, depending on the size and the shape of the particle, allowing for signal enhancement[16-18]. In general, the absorption maximum of gold nanoparticles shifts toward the red spectrum as the size increases[17]. In addition, changing the shape of the nanoparticles changes their absorption properties. For example, spherical and irregular shaped gold nanoparticles of the same average size exhibit absorption maximum at different wavelengths due to an anisotropic distribution of the surface electron layers in the latter[15].

Other common metallic nanoparticles include plasmonic silver nanoparticles with sizes ranging from 20 nm to 150 nm[13]. Silver nanoparticles appear to have higher light absorptivity than gold, and potentially generate stronger photoacoustic signals[17]. Due to their reactivity and toxicity *in vivo*, they have not been studied as extensively as gold nanoparticles. Upconverting nanoparticles are also good candidates for photoacoustic contrast agents because they have narrow excitation/emission profiles. Upconverting nanoparticles are typically based on phosphors, e.g., NaYF4, doped with ytterbium (Yb3+), erbium (Er3+), and terbium (Tb3+). Copper and copper sulfide have also been used[19]. Specifically, copper sulfide is promising because it has a highly tunable absorption peak. Consequently, upconverting nanoparticles cannot be dispersible in an aqueous solution without post-synthetic modifications owing to the presence of hydrophobic surfactants[19].

Other materials include single-walled carbon nanotubes[20], silica coated iron oxide nanoparticles[18] and silica coated gold nanoparticles[21]. The advantage of silica coated nanoparticles is that their surface chemistry can be modified to allow for additional functionalization. In addition, it has been shown that silica coatings can increase the amplitude of the photoacoustic signal up to threefold and fourfold, and prevent optically induced nanoparticle deformation[21].

For our subsurface applications, the material choice will depend on the number of unique tracers required, the reservoir rock type, and other reservoir parameters such as salinity, temperature, and pH.

An alternative approach is to use solid nanoparticles to generate photoacoustic signals via vaporization. When the excitation energy reaches a certain level, the temperature of the area around the interface between the nanoparticle and liquid increases and starts to evaporate, generating what is known as photothermal bubbles. In general, smaller nanoparticles require higher energy levels to generate photothermal bubbles[22]. The advantage of this approach is an increase in the amplitude of the photoacoustic signal, as compared to the signal generated by thermoelastic expansion.

The contrast between the nanoparticles and the background can also be enhanced using dual wavelength systems that use the difference of optical absorption of gold nanoparticles at different wavelengths. This can further improve the sensitivity without having to increase the illuminated laser energy or increase the concentration of the gold nanoparticles injected[15].

The wide range of applications of nanoparticles resulted in the development of numerous methods of fabrication with various sizes and shapes. They can be synthesized as rods, shells, cubes, triangles, irregular structures, and other shapes, which has allowed for a relatively free choice of the wavelength. Due to the high temperature nature of our subsurface environment, it is important for us to consider the photothermal stability of the solid nanoparticles.

Various studies reported that the treatment of nanoparticles with the laser beam has been found to change their morphology toward a more spherical form, which is more

favorable from a thermodynamic point of view[25, 24]. Chen et al. (2010)[21] reported that surface coated nanorods can melt to form spheres below 100 °C to 250 °C, depending on their surface coating.

## Phase Changing Nanodroplets

So far, only solid nanoparticles that rely on thermoelastic expansion to generate photoacoustic signals have been discussed. Unfortunately, the conversion efficiency from optical to acoustic energy through thermoelastic expansion is usually low, e.g., $10^{-6}$. The use of photoacoustic agents in the form of nanodroplets that undergo phase change upon illumination, generating a strong photoacoustic signal in the process, has been previously explored in the biomedical context. The generation of acoustic signals via liquid to gas phase change typically results in signals with a peak amplitude several orders of magnitude higher than through thermoelastic expansion.

Phase changing nanodroplets for photoacoustic applications typically consist of optically absorbing elements (dyes or nanoparticles) suspended in a liquid droplet of a perfluorocarbon (PFC) compound stabilized with albumin, lipids, polymers, or a surfactant[25, 26]. The nanodroplets are vaporized when the encapsulated absorbing elements convert electromagnetic energy to heat, rising the local temperature above the vaporization temperature of the PFC in the nanodroplet form.

Multiple PFC compounds are available and the choice mostly depends on their boiling temperature. Most of the literature centers around low boiling temperature PFCs such as octafluoropropane (-39 °C), perfluorobutane (-2 °C), perfluoropentane (29 °C), and perfluorohexane (56 °C) because typical biomedical and biological applications do not involve high temperature. Subsequently, many oil and gas applications involve temperatures significantly higher, closer to 100 °C. Examples of PFCs with a higher boiling temperature include perfluorohexyl bromide (97 °C), perfluorooctyl bromide (142 °C), and perfluoro-15-crown-5-ether (146 °C). It should be noted that the likelihood of a droplet vaporizing depends on several factors, including droplet size, PFC boiling point, type of photoabsorber, local laser fluence, viscoelasticity of the medium, droplet shell composition, and ambient temperature[27, 28].

Wilson et al. (2012)[25] reports on 200 nm diameter nanodroplets of perfluoropentane (29 °C) reaching 50 °C before undergoing vaporization. Similarly, Hannah et al. (2014)[27] noticed that nanodroplets with a diameter average of 600 nm, of the same compound, remained in a liquid state at 37 °C. Sheeran et al. (2012)[29] has shown that droplets of octafluoropropane (-36.7 °C) remain stable at 22 °C. Phillips et al. (2013)[30] reports that nanodroplets with an average diameter of 240 nm made of a mixture of prefluorobutane (-2 °C) and perfluoropentane (29 °C) stable at 37 °C. This behavior can be partly explained by the Laplace pressure, which predicts that the pressure inside the nanodroplets is higher than outside, as shown by Eqn. 9.

The Clausiuse Clapeyron relation predicts that the temperature at which a substance undergoes a phase transition is inversely proportional to the pressure it is subjected to. As the droplet size decreases, the Laplace pressure, due to the radial curvature, increases. Therefore, it is possible to have a PFC nanodroplet in a liquid state well above the boiling temperature of the bulk material, resulting in PFC cores that are superheated:

$$\Delta P = P_{in} - P_{out} = \frac{2}{R}\gamma \qquad 9$$

where $R$ is the radius of the droplet and $\gamma$ is the interfacial tension. We can readily see from Eqn. 9 that the Laplace pressure becomes significant for smaller droplets and at higher interfacial tensions. For the case of nanodroplets, the pressure inside the droplet can be several atmospheres higher than outside. Solving Eqn. 9 for the pressure inside the droplet, we reach the following expression:

$$P_{in} = P_{out} + \frac{2}{R}\gamma \qquad 10$$

The Antoine equation can be used to estimate the temperature at which the droplet will vaporize given the increased pressure inside the droplet, as follows:

$$T = \frac{B}{A - \log_{10} p} - C \qquad 11$$

where $A$, $B$, and $C$ are component specific constants obtained empirically, and $p$ is the pressure inside the droplet.

For illustration purposes, Fig. 3 shows the vaporization temperature predicted by the Antoine equation as a function of droplet size for multiple PFC compounds. The vaporization temperature increases with decreasing droplet size, regardless of the compound. This behavior is explained by an increase in the pressure inside the droplet with a decreasing diameter, as predicted by Eqn. 10. As the droplet size is reduced, the change in boiling point becomes significant. For example, perfluorobutane (C4F10) as a bulk has a boiling temperature of -1.7 °C. The Antoine equation predicts that in the form of 100 nm droplets, it will boil at close to 80 °C.

There are many examples in the literature where the droplets vaporize well above the temperature predicted by Eqn. 11[31]. This suggests that the Laplace pressure is not the only mechanism preventing vaporization, and other factors, such as the viscoelasticity of the medium and droplet shell composition, seem to have a significant effect too[31]. It is also possible to tune the vaporization temperature by mixing different PFCs[32, 33].

The nanodroplets can also be designed to undergo vaporization upon excitation at very specific wavelengths by choosing the right absorbing elements. The most common absorbing elements are in the form of dyes or nanoparticles. Santiesteban et al. (2019)[26] developed laser activated PFC nanodroplets that respond to different wavelengths by embedding either Epolight 9151 (680 nm peak absorption) or Epolight 3832 (1,064 nm peak absorption), both commercially available dyes, into PFC nanodroplets. Similarly, Yoon et al. (2019)[28] encapsulated Epolight 9151 in liquid nanodroplets of perfluorohexane stabilized by a fluorosurfactant shell and obtained nanodroplets with a peak absorption at 760 nm. Hallam et al. (2018)[34] encapsulated Epolight 3072 dye within perfluorohexane droplets stabilized with Zonyl FSO fluorosurfactant to obtain nanodroplets with an
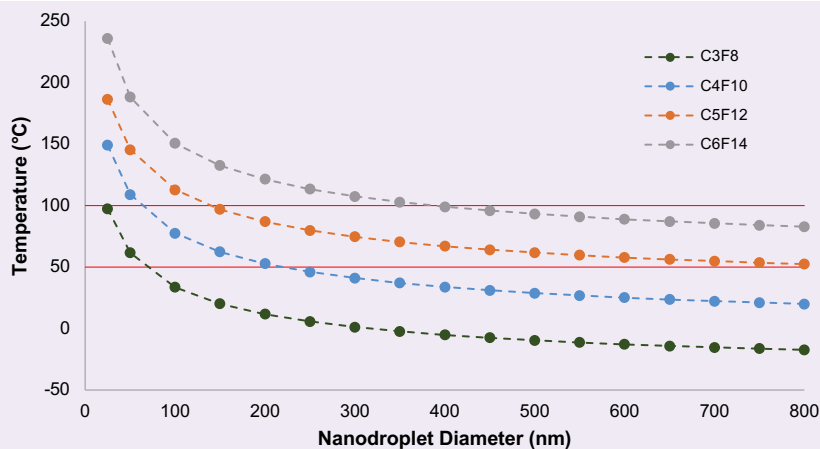
average diameter of 340 nm and peak optical absorption at 1,064 nm. Indocyanine green has also been used to activate nanodroplets in the near infrared region[27]. In a similar strategy, Zhang et al. (2019)[35] encapsulated PFC nanodroplets using a lipid shell that contains cyanine 7.5 to create photoacoustic nanodroplets with a peak absorption at 788 nm.

An alternative strategy is to encapsulate nanoparticles, rather than dyes, to act as optical absorbers. Common materials include gold, lead sulfide, iron oxide, and silver[25, 36]. As previously shown, Fig. 2, the size and shape of the nanoparticles can be tuned to shift their peak optical absorption. Therefore, it is possible to tune the wavelength at which the nanodroplets activate.

It has been shown that it is possible to recondense the nanodroplets after activation[28, 34]. The recondensation depends on multiple parameters, including the core type, droplet size, photoabsorber type, optical fluence, temperature, acoustic pressure, and viscoelasticity of the medium. In general, if the temperature of the medium containing the nanodroplet is above its boiling temperature, the nanodroplets will recondense and will undergo a gas-liquid phase change. This can be advantageous because it means the measurements are repeatable[34].

### Excitation Source

For a sample to emit a photoacoustic signal, it must be illuminated with light. The light sources can be classified based on their excitation mode as continuous wave or pulsed sources. Figure 4 shows a schematic representation of what the excitation and the generated photoacoustic signal look like for continuous wave and pulsed sources. In continuous wave mode, the duty cycle is typically 50%, and the signal is detected by a locked in amplifier and analyzed in the frequency domain[37]. Because of the large duty cycle, the boundary conditions of the cell containing the sample should be taken into consideration when analyzing the photoacoustic response[2]. The pulsed mode uses high peak intensity pulses of short duration with low duty cycles (usually less than $10^{-5}$), while the signal is detected by a transient digitizer and analyzed in the time domain[37]. Because of the low duty cycles, thermal diffusion effects can often be ignored, and in
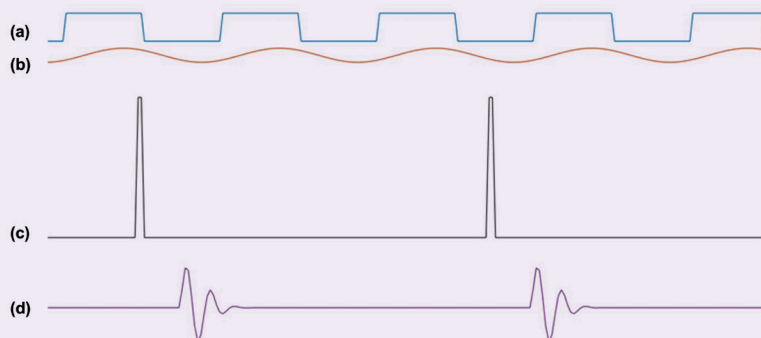
**Table 1** *The comparison between continuous wave and pulsed sources.*

|  | **Continuous Wave** | **Pulsed** |
|---|---|---|
| Duty cycle | High | Low |
| Sound generation efficiency | Low | High |
| Effect of boundaries | Important | Negligible |
| Main applications | Spectroscopy, estimation of material thermal properties, flaw detection | Flow cytometry, photoacoustic tomography and microscopy, material characterization |

most cases, the cell containing the sample has no effect on the received signal, because the pulse is smaller than the cell dimensions[2].

Table l summarizes the main differences between the continuous wave and pulsed modes as well as their main applications. For the same average optical power, the pulsed mode typically yields higher peak pressure, and therefore, a higher detection sensitivity. We will focus on the pulsed mode because it is the one that provides higher detection sensitivity.

When selecting the light source, it is important to consider the light pulse width, the energy of the pulse, the repetition rate, wavelength, and spectral width. A lot of the literature for pulsed excitation describes the use of high power Nd:YAG lasers with wavelengths in the near infrared region (600 nm to 1,200 nm), because in this range, biological tissues exhibit low absorption[38]. These sources typically generate ns-wide pulses with mJ energy levels and peak power of several kW to MW[38, 39]. The pulse repetition rate is usually low, between l0 Hz to 30 Hz. Consequently, the downside of lasers include their high cost, large size for portable applications, wavelength limitation, as well as the risk of exposure involved with its class-IV illumination[38, 39].

To overcome these limitations, the use of alternative light sources, such as laser diodes and light emitting diodes (LEDs) in photoacoustic applications has been recently explored. These systems are not only smaller and more cost-effective, but they are also more stable, require less maintenance and offer a much higher pulse repetition rate (up to several kHz). Unfortunately, their energy level is significantly lower than that of lasers (typically μJ to nJ) with typical peak powers of hundreds of watts, even when using an arrayed arrangement of LED elements to increase the energy level.

Therefore, significant signal averaging is required to achieve a signal-to-noise ratio (SNR) similar to that obtained by high power laser sources. Agrawal et al. (2020)[39] has shown that by averaging 2,560 signals obtained using an LED-based source, they can achieve a SNR comparable to that obtained by a single signal from a laser source.

## Gaps and Challenges

It appears clear that the photoacoustic effect offers new opportunities for the oil and gas industry, especially in the form of a new class of nanotracers for subsurface characterization. Moreover, important gaps and challenges must be addressed before incorporating this technology into routine operations. As mentioned before, most of the research found in the literature was conducted in the biological context. As such, the nanoagents have been tested and optimized for biological systems. The downhole environment is generally harsher than that considered in biological applications due to higher temperatures (often above 90 °C) and salinity (200,000 ppm or more). These conditions pose a challenge to the stability of the nanoagents.

The examples presented here have not been tested under reservoir-like conditions. It is very likely that at least some of the nanoagents will not be stable at reservoir conditions in their current form. Fortunately, significant research has been conducted to develop strategies to stabilize nanoparticles in solution for hydrocarbon reservoir applications. It is possible that some of these strategies can be applied to stabilize photoacoustic nanoagents.

The transportability of the nanoagents at reservoir conditions needs to be tested too. The transport requirements for which these agents have been tested have to do with transport in living organisms under passive and active biological processes. Therefore, it remains to be determined how well these agents can transport through porous subsurface media. There is a large amount of literature discussing the transport of nanoparticles through porous media, and over the years, multiple strategies have been developed to improve their transport properties. It is very likely that some of these approaches will be required to achieve the desired transport properties of potential photoacoustic nanoagents depending on the specific reservoir conditions. The compatibility of potential nanoagents with reservoir fluids must be evaluated as well, to prevent any potential damage to the reservoir upon injection.

Determining the lower detection limit for each of the potential nanoagents at operating conditions is also a requirement that will have an impact not only on the sensitivity of each nanotracer, but also on the economic viability. It is also important early on in the research phase to obtain the extinction spectrum for the produced fluids. This will help identify the wavelengths that will generate minimum background noise when exciting the photoacoustic nanoagents.

Some of the challenges that we can forecast include the photothermal stability when using solid nanoparticles. As discussed earlier, some nanoparticles change shape upon exposition to electromagnetic radiation. Therefore, their extinction spectrum may shift and no longer be triggered properly by the initial wavelength. In addition, if the extinction spectrum of the produced fluids is broad, that may limit the number of unique nanotracers that can be developed. The synthesis scale-up of each agent remains to be developed and may be challenging, depending upon the complexity of the nanotracers. While biological applications require only small amounts of material, our operations will require a significantly larger amount. Therefore, simple and inexpensive synthesis approaches are desirable.

## Conclusions

We have shown that properly engineered nanoparticles may serve as a new class of subsurface nanotracers detected and quantified via the photoacoustic effect to aid hydrocarbon reservoir characterization. From the theoretical analysis presented, we can conclude that nanoagents made of materials with high volumetric expansion and optical absorption, and low specific heat capacity increase the amplitude of the photoacoustic signal generated upon illumination. In addition, sources that generate narrow beams and short pulses increase the amplitude of the photoacoustic signal too. Therefore, these properties are desirable for a photoacoustic-based system.

By conducting a literature review, we identified two classes of nanoparticles that we deem potential candidates for subsurface operations. The first one is based on solid nanoparticles that generate photoacoustic signals via thermoelastic expansion. Multiple examples of solid nanoparticles for photoacoustic applications in the biological context are available. Their main advantages are that they can be tuned to respond to different wavelengths and their surface can be functionalized to improve their stability and transportability and to provide additional capabilities.

The second class of nanoparticles corresponds to phase changing nanodroplets. These agents consist of light absorbing elements encapsulated in liquid nanodroplets, typically made of a PFC compound. Upon illumination, the nanodroplets undergo a liquid to gas phase change and generate a strong photoacoustic signal. Their main advantages are that the amplitude of the photoacoustic signal generated through vaporization can be several orders of magnitude higher than through thermoelastic expansion. In addition, the vaporization temperature can be tuned by choosing the appropriate PFC compound or by mixing multiple compounds.

Most of the research on photoacoustic nanoparticles available in the literature was conducted for biological applications. As such, the nanoparticles have been designed and optimized to function in conditions relevant to biological systems. The high salinity and temperature typically present in hydrocarbon reservoirs poses a challenge for which such nanoparticles were not originally designed. Therefore, the qualification of the different photoacoustic nanoparticles for hydrocarbon reservoir applications remains an area of research. It is very likely that additional efforts will be required to make sure the nanoparticles are stable at high temperature and salinity, and that they can transport efficiently through the subsurface.

At the time of this writing, no other study investigating the feasibility of using photoacoustic nanoparticles for tracer applications was found. Our work paves the way for a new class of passive tracers for oil reservoirs. Photoacoustic nanotracers are easy to detect and quantify and are therefore suitable for continuous in-line monitoring, contributing to the ongoing real-time data efforts in the oil and gas industry.

## Acknowledgments

## References

1.  Manohar, S. and Razansky, D.: "Photoacoustics: A Historical Review," *Advances in Optics and Photonics*, Vol. 8, Issue 4, 2016, pp. 586-617.

2.  Hodgson, P.: "The Detection of Oil in Water by Near Infrared Pulsed Photoacoustic Spectroscopy," Ph.D. thesis, Heriot-Watt University, U.K., 1994, 116 p.

3.  Putri, K.Y., Yulianto, N. and Herbani, Y.: "Study on Acoustic Detections of Nd:YAG Laser Induced Breakdown at Different Wavelengths," *Journal of Physics: Conference Series*, Vol. 817, 2017.

4.  Samokhin, A., Il'ichev, N.N., Klimentov, S.M. and Pivovarov, P.A.: "Photoacoustic and Laser Induced Evaporation Effects in Liquids," *Applied Physics B*, Vol. 105, Issue 3, November 2011, pp. 551-556.

5.  Herbert, S.K., Han, T. and Vogelmann, T.C.: "New Applications of Photoacoustics to the Study of Photosynthesis," *Photosynthesis Research,* Vol. 66, 2000, pp. 13-31.

6.  Renard, M., Thirion, P. and Delmelle, M.: "Photoacoustic Spectroscopy of Bacteriorhodopsin Photocycle," *Biophysical Journal*, Vol. 44, Issue 2, November 1983, pp. 211-218.

7.  Legrange, J., Caplan, S.R. and Cahen, D.: "Simulations of Frequency Dependent Photoacoustic Magnitude Signals and their Implications for Bacteriorhodopsin Photocycle Energetics," *Biophysical Chemistry*, Vol. 20, Issue 3, October 1984, pp. 249-259.

8.  Patel, C.K.N. and Tam, A.C.: "Pulsed Optoacoustic Spectroscopy of Condensed Matter," *Reviews of Modern Physics*, Vol. 53, Issue 3, July-September 1981.

9.  Lai, H.M. and Young, K.: "Theory of the Pulsed Optoacoustic Technique," *The Journal of the Acoustical Society of America*, Vol. 72, Issue 6, 1982.

10. Freeborn, S.S., Hannigan, J. and MacKenzie, H.A.: "Application of Pulsed Photoacoustics in Water at High Pressure," *Applied Optics*, Vol. 38, Issue 24, 1999, pp. 5118-5121.

11. Schanke, T., Kjølberg, S.A. and Vogel, F.: "Oil in Water Monitoring for Subsea and Downhole Separators," SPE paper 66538, presented at the SPE/EPA/DOE Exploration and Production Environmental Conference, San Antonio, Texas, February 26-28, 2001.

12. Schmid, T., Panne, U., Haisch, C., Hausner, M., et al.: "A Photoacoustic Technique for Depth Resolved in Situ

Monitoring of Biofilms," *Environmental Science & Technology*, Vol. 36, Issue 19, August 2002, pp. 4135-4141.

13. Lemaster, J.E. and Jokerst, J.V.: "What is New in Nanoparticle-Based Photoacoustic Imaging?" *Wiley Interdisciplinary Reviews, Nanomedicine and Nanobiotechnology*, Vol. 9, Issue 1, January 2017.

14. Mokrousov, M., Novoselova, M., Nolan, J., Harrington, W., et al.: "Amplification of Photoacoustic Effect in Bimodal Polymer Particles by Self-Quenching of Indocyanine Green," *Biomedical Optics Express*, Vol. 10, Issue 9, 2019, pp. 4775-4788.

15. Wei, C-W., Liao, C-K., Tseng, H-C., Lin, Y-P., et al.: "Photoacoustic Flow Measurements with Gold Nanoparticles," *IEEE Transactions on Ultrasonics, Ferroelectrics, and Frequency Control*, Vol. 53, Issue 10, October 2006, pp. 1955-1959.

16. Link, S. and El-Sayed, M.A.: "Spectral Properties and Relaxation Dynamics of Surface Plasmon Electronic Oscillations in Gold and Silver Nanodots and Nanorods," *Journal of Physical Chemistry B*, Vol. 103, Issue 40, 1999, pp. 8410-8426.

17. Huang, X. and El-Sayed, M.A.: "Gold Nanoparticles: Optical Properties and Implementations in Cancer Diagnosis and Photothermal Therapy," *Journal of Advanced Research*, Vol. 1, Issue 1, January 2010, pp. 13-28.

18. Alwi, R., Telenkov, S., Mandelis, A., Leshuk, T., et al.: "Silica-Coated Super Paramagnetic Iron Oxide Nanoparticles (SPION) as Biocompatible Contrast Agent in Biomedical Photoacoustics," *Biomedical Optics Express*, Vol. 3, Issue 10, October 2012, pp. 2500-2509.

19. Maji, S.K., Sreejith, S., Joseph, J., Lin, M., et al.: "Upconversion Nanoparticles as Contrast Agent for Photoacoustic Imaging in Live Mice," *Advanced Materials*, Vol. 26, Issue 32, August 2014, pp. 5633-5638.

20. Pramanik, M., Swierczewska, M., Green, D., Sitharaman, B., et al.: "Single-Walled Carbon Nanotubes as a Multimodal Thermoacoustic and Photoacoustic Contrast Agent," *Journal of Biomedical Optics*, Vol. 14, Issue 3, 2009.

21. Chen, Y-S., Frey, W., Kim, S., Homan, K., et al.: "Enhanced Thermal Stability of Silica-Coated Gold Nanorods for Photoacoustic Imaging and Image Guided Therapy," *Optics Express*, Vol. 18, Issue 9, April 2010, pp. 8867-8878.

22. Wang, S., Fu, L., Xin, J., Wang, S., et al.: "Photoacoustic Response Induced by Nanoparticle-Mediated Photothermal Bubbles beyond the Thermal Expansion for Potential Theranostics," *Journal of Biomedical Optics*, Vol. 23, Issue 12, December 2018.

23. Vasa, P., Sharma, R., Singh, M., Dharmadhikari, A.K., et al.: "Generation of Stable Colloidal Gold Nanoparticles by Ultrashort Laser-Induced Melting and Fragmentation," *Materials Research Express*, Vol. 1, Issue 3, August 2014.

24. Warshavski, O., Minai, L., Bisker, G. and Yelin, D.: "Effect of Single Femtosecond Pulses on Gold Nanoparticles," *The Journal of Physical Chemistry C*, Vol. 115, Issue 10, 2011, pp. 3910-3917.

25. Wilson, K., Homan, K. and Emelianov, S.: "Biomedical Photoacoustics beyond Thermal Expansion Using Triggered Nanodroplet Vaporization for Contrast-Enhanced Imaging," *Nature Communications*, Vol. 3, January 2012.

26. Santiesteban, D.Y., Hallam, K.A., Yarmoska, S.K. and Emelianov, S.Y.: "Color-Coded Perfluorocarbon Nanodroplets for Multiplexed Ultrasound and Photoacoustic Imaging," *Nano Research*, Vol. 12, Issue 4, April 2019, pp. 741-747.

27. Hannah, A., Luke, G., Wilson, K., Homan, K., et al.: "Indocyanine Green-Loaded Photoacoustic Nanodroplets: Dual Contrast Nanoconstructs for Enhanced Photoacoustic and Ultrasound Imaging," *ACS Nano*, Vol. 8, Issue 1, 2014, pp. 250-259.

28. Yoon, H. and Emelianov, S.Y.: "Combined Multiwavelength Photoacoustic and Plane-Wave Ultrasound Imaging for Probing Dynamic Phase-Change Contrast Agents," *IEEE Transactions on Biomedical Engineering*, Vol. 66, Issue 2, February 2019, pp. 595-598.

29. Sheeran, P.S., Luois, S.H., Mullin, L.B., Matsunaga, T.O., et al.: "Design of Ultrasonically Activatable Nanoparticles Using Low Boiling Point Perfluorocarbons," *Biomaterials*, Vol. 33, Issue 11, April 2012, pp. 3262-3269.

30. Phillips, L.C., Puett, C., Sheeran, P.S., Wilson Miller, G., et al.: "Phase-Shift Perfluorocarbon Agents Enhance High Intensity Focused Ultrasound Thermal Delivery with Reduced Near Field Heating," *The Journal of the Acoustical Society of America*, Vol. 134, Issue 2, August 2013, pp. 1473-1482.

31. Mountford, P.A.C.: "Molecular Thermodynamics of Superheated Lipid-Coated Fluorocarbon Nanoemulsions," Ph.D. thesis, University of Colorado at Boulder, Colorado, 2015, 171 p.

32. Kawabata, K., Sugita, N., Yoshikawa, H., Azuma, T., et al.: "Nanoparticles with Multiple Perfluorocarbons for Controllable Ultrasonically Induced Phase Shifting," *Japanese Journal of Applied Physics*, Vol. 44, 2005, pp. 4548-4552.

33. Martin, A.L., Seo, M., Williams, R., Belayneh, G., et al.: "Intracellular Growth of Nanoscale Perfluorocarbon Droplets for Enhanced Ultrasound-Induced Phase-Change Conversion," *Ultrasound in Medicine & Biology*, Vol. 38, Issue 10, October 2012, pp. 1799-1810.

34. Hallam, K.A., Donnelly, E.M., Karpiouk, A.B., Hartman, R.K., et al.: "Laser Activated Perfluorocarbon Nanodroplets: A New Tool for Blood Brain Barrier Opening," *Biomedical Optics Express*, Vol. 9, Issue 9, September 2018, pp. 4527-4538.

35. Zhang, G., Wang, B., Shah, A., Bamber, J., et al.: "Contrast Enhanced Photoacoustic Imaging of Low Boiling Point Phase-Change Nanodroplets," paper presented at the IEEE International Ultrasonics Symposium, Glasgow, Scotland, U.K., October 6-9, 2019.

36. Strohm, E., Rui, M., Gorelikov, I., Matsuura, N., et al.: "Vaporization of Perfluorocarbon Droplets Using Optical Irradiation," *Biomedical Optics Express*, Vol. 2, Issue 6, June 2011, pp. 1432-1442.

37. Tam, A. and Coufal, H.: "Pulsed Opto-Acoustics: Theory and Applications," *Journal de Physique Colloques*, Vol. 44, October 1983, pp. C6-9–C6-20.

38. Allen, T.J. and Beard, P.C.: "Pulsed Near Infrared Laser Diode Excitation System for Biomedical Photoacoustic Imaging," *Optics Letters*, Vol. 31, Issue 23, 2006, pp. 3462-3464.

39. Agrawal, S., Singh, M.K.A., Yang, X., Albahrani, H., et al.: "Photoacoustic Imaging Capabilities of Light Emitting Diodes (LED) and Laser Sources: A Comparison Study," *Photons Plus Ultrasound: Imaging and Sensing 2020*, February 2020, Vol. 11240.

## About the Authors

**Jesus M. Felix Servin**

*M.S. in Chemical and Biological Engineering,*
*King Abdullah University of Science and Technology*

Jesus M. Felix Servin joined the Reservoir Engineering Technology Division of Saudi Aramco's Exploration and Petroleum Engineering Center – Advanced Research Center (EXPEC ARC) in February 2012. His focus is on the development of electromagnetic methods and nanoparticle-based contrast agents for reservoir characterization and monitoring. Jesus's role has been instrumental in the development and deployment of the Magnetic Nano-Mappers project, including hardware design and in-house fabrication, instrumentation, computer programming, and data processing.

Jesus' interests include the development of nanoscale strategies for reservoir illumination and electromagnetic methods for reservoir description and monitoring.

He received his B.S. degree in Engineering Physics from Instituto Tecnologico y de Estudios Superiores de Monterrey, Monterrey, Mexico, and an M.S. degree in Chemical and Biological Engineering from King Abdullah University of Science and Technology, Thuwal, Saudi Arabia.

**Hala A. AlSadeg**

*B.S. in Materials Science and Engineering,*
*Pennsylvania State University*

Hala A. AlSadeg is a Petroleum Scientist working with the Reservoir Engineering Technology Team of Saudi Aramco's Exploration and Petroleum Engineering Center – Advanced Research Center (EXPEC ARC). She works on several research projects aimed at utilizing nanotechnology for enhanced oil recovery and reservoir characterization applications.

In 2018, Hala received her B.S. degree (highest honors) in Materials Science and Engineering from the Pennsylvania State University, State College, PA. Her undergraduate research was focused on the fabrication and characterization of 2D heterostructures for sensing and electronic applications.

**Dr. Amr I. Abdel-Fattah**

*Ph.D. in Chemical Engineering,*
*University of New Mexico*

Dr. Amr I. Abdel-Fattah is a Petroleum Engineering Specialist and Team Leader of the In-Situ Sensing and Intervention focus area in Saudi Aramco's Exploration and Petroleum Engineering Center – Advanced Research Center (EXPEC ARC). He joined EXPEC ARC's Reservoir Engineering Technology Division in late 2012 after working 16 years with the Los Alamos National Laboratory in New Mexico, U.S., where he reached a Senior Scientist status. Amr is currently spearheading a number of research and technology development programs in EXPEC ARC geared at utilizing nanotechnology for upstream oil and gas applications.

He has over 30 years of experience in subsurface energy and environmental applications of nanotechnology, colloid and interface science, and electrokinetics. Amr is a Society of Petroleum Engineers (SPE) Distinguished Lecturer, a founding Board Member of the International Association of Electrokinetics, a U.S. Representative on the International Board of Electrokinetics, a Technical Member on the Science Advisory Board of the International Association of Colloid and Interface Scientists, and a Guest Editor for the international *Journal of Colloids and Surfaces A*.

He has published numerous papers in international journals, including some of the world's premier and most cited journals, and delivered numerous plenary and invited talks and lectures worldwide. Amr chaired the International Electrokinetics Conference in Santa Fe, NM, in 2008, in addition to several international workshops and conference sessions in the U.S., Canada, and Europe since 2005.

He received his B.S. degree in Civil Engineering and an M.Eng. in Geotechnical Engineering from Ain Shams University, Cairo, Egypt. Amr received his M.S. degree and his Ph.D. degree in Chemical and Nuclear Engineering from the University of New Mexico, Albuquerque, NM.

# Establishing and Estimating Gas-Liquid Performance Characteristics of Multiphase Pumps

*Dr. Chidirim E. Ejim*

**Abstract /**

Multiphase electric submersible pumps (ESPs) are used to produce gas and liquid in wells with high gas content. These pumps are operated at different speeds, and designed to handle flows with various gas volume fractions (GVFs). This study uses gas-liquid dimensionless parameters to obtain and compare the performance of conventional multiphase pumps. Knowledge of such techniques is important for production engineers, field operators, and application engineers to ascertain pump performance for given gas-liquid operating conditions.

The gas-liquid performance data for two multiphase pumps with 8.00" and 8.62" housing diameters were obtained from open literature. The inlet pressure, GVF and rotational speed ranges were 100 psig to 300 psig, and 0 to 0.57, and 3,000 revolutions per minute (rpm) to 3,600 rpm, respectively. The total flow rates varied from 15,000 barrels per day (bpd) to 60,000 bpd. The Euler turbomachinery principles for gas-liquid flows were applied to the data to obtain required dimensionless parameters and two-phase dimensionless performance curves for the pumps. The method was tested using dimensionless curves for a given operating condition to obtain pump performance at another operating condition.

The results showed that for each rotational speed, the difference in dimensionless pressure between the multiphase pump discharge and inlet decreased with an increasing mass-quality-weighted volume flow rate. For each of the weighted volume flow rates, the difference in pump discharge and inlet dimensionless pressures decreased with increasing GVF. The decrease in GVF can range between a factor of 3 and 4, depending on the magnitude of the weighted volume flow rate.

Using the 3,000-rpm data, a two-phase (gas-liquid) dimensionless performance curve was obtained for one of the multiphase pumps with intake GVFs and the dimensionless volume flow rate parameter the independent variables. The curve was used to estimate pump performance at 3,600 rpm for each GVF, and then compared with the actual reference test data. For the second multiphase pump, two data sets at different pressures were used to obtain the effects of intake pressure. The performance for this multiphase pump was a function of dimensionless volume flow rate, intake GVF and intake gas-liquid density ratio (DR). The maximum error in the estimated performance data was within 7%. Overall, the performance of multiphase pumps can be estimated using the technique in this study for the flow conditions analyzed.

This study highlights the importance of obtaining dimensionless two-phase performance characteristics of multiphase pumps. Given that these pumps are frequently used in oil field production operations, the capability to determine the pressure boosting performance of the pumps — for given operating conditions — is important to field operating personnel and design engineers. This knowledge benefits the operator to optimally produce hydrocarbons from high gas content wells and maximize the economic bottom line from the field asset.

## Introduction

Electric submersible pumps (ESPs) are artificial lift systems primarily used to lift pure liquids or low gas content liquids in downhole or surface operations. The pumping section of an ESP is comprised of a rotating rotor (or impeller) and a stationary diffuser. The rotor and diffuser assembly is called a pump stage. The rotors add kinetic energy to the fluid, and the diffusers convert the kinetic energy to pressure energy. The total pressure energy from the ESP is typically the sum of the pressure energy from each pump stage in the pumping section.

Gas typically comes out of a solution in production scenarios, where the pressure falls below the bubble point pressure. When this occurs, for a given ESP with rotors rotating at a given revolution per minute (rpm), the performance of the ESP is affected by the intake pressure and intake gas volume fraction (GVF). The GVF is defined as the volume of free gas to the total volume of free gas and liquid at a given temperature and pressure. Higher magnitudes of GVF degrades pump performance to a point where liquid cannot be transported by the pump. This condition is known as gas lock[1].

To facilitate production in high GVF conditions, multiphase pumps are one of the gas handling devices that may be installed upstream of a standard ESP. Multiphase pumps come in different designs, which include the centrifugal and helico-axial types. A split vane impeller pump (SVIP) is an example of a centrifugal type multiphase pump. Its rotors are constructed to prevent accumulation or formation of gas pockets within its vane cavities and also facilitate fluid pressure distribution. A helico-axial pump (HAP) is a type of multiphase pump. Its rotors are designed to reduce gas-liquid separation, and improve gas-liquid mixing to prevent gas lock. The GVF limits of the SVIP and HAP are up to 0.70 and 0.75, respectively[1].

Obtaining dimensionless performance curves for multiphase pumps is important to ascertain their behavior. Such performance curves follow affinity or scaling laws common in pumping applications for single-phase flows[2], which are fundamentally obtained from the Euler turbomachinery equation[3]. Patil et al. (2019)[4] presented work related to obtaining performance curves related to multiphase flows. They tested a four-stage, 8.62" outside diameter (OD) HAP at 3,000 rpm and 3,600 rpm using air and water, as well as air and a higher viscosity liquid. The pump intake pressures were between 40 psi to 300 psi, the water volume flow rate was in the range 10,000 barrels per day (bpd) to 45,000 bpd, and the range of intake GVF was from 0 to 0.5.

Flow coefficients were obtained using the total gas and liquid volume flow rates. Subsequently, they achieved collapse of test data points by introducing an exponent, which was a function of rotational speed and GVF. They cited analysis of two-phase data of other pump types, which was required for further improvement and development of their technique.

Morrison et al. (2014)[5] presented the performance evaluation of a multiphase pump by testing a three-stage 8" diameter SVIP using air and water. The SVIP was operated at 3,000 rpm, 3,300 rpm, and 3,600 rpm with water volume flow rates varying from 15,000 bpd to 50,000 bpd. The pump intake pressures were kept constant at 100 psig, 200 psig, and 300 psig, and the intake GVF varied from 0 to 0.57.

The results presented in their work included variation of pump pressure boost vs. volume flow rate, among other data. Subsequently, their results were not presented in dimensionless form to investigate the conformance of the test data with scaling or affinity laws related to a multiphase pump operating with gas and liquid as the working fluid.

This study involves obtaining the dimensionless relationship of multiphase pumps by revisiting the Euler turbomachinery equation to obtain dimensionless parameters that may be applied to multiphase flows. These dimensionless parameters will be computed using the SVIP and HAP test data from the reference literatures previously cited. Another goal of this work is to obtain a performance equation for the SVIP and HAP. Such equations are useful to determine the pump pressure boost for a given pump type and multiphase flow condition. These equations also aid in understanding parameters required to improve pump design and increase the operating envelope of a multiphase pump. This ultimately benefits the production engineer, operator, and other field asset stakeholders.

## Theory
### Original Form of Performance Equation

Obtaining the performance relationship of centrifugal machines requires applying the steady flow energy equation (or law of conservation of energy) and the law of conservation of momentum to the machine's control volume. The governing equations are subsequently determined by equating like terms from the above-mentioned equations, which gives the Euler turbomachinery equation. In developing the equation for the ideal (Euler) two-phase pump head, Poullikkas (1992)[6] applied the following assumptions to the steady flow energy equation:

- The flow is frictionless and steady.
- Liquid and gas trajectories are identical; therefore, the control volume is bounded by two streamlines.
- The gas phase is a perfect gas.
- The fluids are undergoing an isothermal process.
- The mixture is compressible and noncondensable, i.e., no mass transfer between gas and liquid.

Upon simplification, the ideal (Euler) two-phase pump head was derived, Eqn. 1:

$$H_{E\_2ph} = \left(\frac{P_2}{g\rho_{m2}} - \frac{P_1}{g\rho_{m1}}\right) + (1-x)\frac{(V_{L2}^2 - V_{L1}^2)}{2g} +$$

$$x\frac{(V_{G2}^2 - V_{G1}^2)}{2g} + x\frac{RT}{g}\ln\frac{P_2}{P_1} \qquad \text{1}$$

where $H_{E\_2ph}$ = Euler (or Ideal) two-phase pump head, $P$ = absolute mixture pressure, $g$ = acceleration due to gravity, $\rho_m$ = mixture density, $x$ = mixture quality, i.e., ratio of gas mass flow rate to total mass flow rate of gas and liquid, $V_L$ = liquid velocity, $V_G$ = gas velocity, $R$ = characteristic gas constant = (287 J/kgK for air), $T$ = absolute temperature of the gas, $GVF$ = ratio of gas volume flow rate to total volume flow rate of gas and liquid, and $\rho_L$ = liquid density.

For a homogeneous gas-liquid mixture,

$$\rho_{m1} = (1 - GVF_1)\rho_L + GVF_1\frac{P_1}{RT} \qquad \text{2}$$

$$\rho_{m2} = (1 - GVF_2)\rho_L + GVF_2\frac{P_2}{RT} \qquad \text{3}$$

where subscripts 1 and 2 denote pump intake and discharge conditions, respectively.

In addition to the previously highlighted assumptions, the following additional assumptions were applied by Poullikkas (1992)[6] to the rotor using the law of conservation of momentum:

- The trajectory of liquid and gas phases are parallel to the rotor blades, i.e., 1D flow.
- The rotor has an infinite number of blades with zero thickness.
- The liquid and gas phases enter and leave the rotor with identical relative angle or negligible difference in relative angles.

After simplification, the corresponding equation for the Euler (or Ideal) two-phase pump head was given by:

$$H_{E\_2ph} = \frac{1}{g}\left[\left(U_2^2 - \frac{U_2\{(1-x)Q_L - xQ_{G2}\}}{\pi D_2 b_2 \tan\beta_2}\right) + \right.$$

$$\left.\left(U_1^2 - \frac{U_1\{(1-x)Q_L - xQ_{G1}\}}{\pi D_1 b_1 \tan\beta_1}\right)\right]$$

        *4*

where, $U$ = rotor peripheral speed = $\left(\frac{D}{2}\frac{2\pi N}{60}\right)$, $N$ is the rotor's rpm, $Q_L$ = liquid volume flow rate, $Q_G$ = gas volume flow rate, $D$ = rotor diameter, $b$ = rotor blade height, and $\beta$ = rotor blade angle.

Equations 1 and 4 may be equated together to obtain an ideal performance equation for the multiphase pump.

### Reduced Form of Performance Equation

The form of Eqns. 1 and 4 has many parameters, which can render an analysis cumbersome. In this study, the parameters were reduced by applying approximations based on knowledge of pump design fluid hydraulics and typical pump test conditions as seen in practice.

In typical pump tests, inlet and discharge pipe diameters are typically of the same size. As such, at the pipe locations were pressure traps were made to measure pressure data across the pump, the liquid velocity head difference between the pump intake and discharge is negligible. Similarly, the gas velocity head difference between the pump intake and discharge is also negligible. Therefore, in Eqn. 1, $(V_{L2}^2 - V_{L1}^2) \approx 0$ and $(V_{G2}^2 - V_{G1}^2) \approx 0$.

In classical pump designs, fluid entry at the pump inlet is typically designed for zero or negligible inlet swirl velocity. Applying this to the liquid and gas phases, the second term on the right-hand side of Eqn. 4 is approximately zero. Applying these two approximations highlighted so far to Eqns. 1 and 4, equating them and then simplifying them provides the following:

$$\left(\frac{P_2}{\rho_{m2}U_2^2} - \frac{P_1}{\rho_{m1}U_2^2}\right) + x\frac{RT}{U_2^2}\ln\frac{P_2}{P_1} = \left[1 - \left\{\frac{(1-x)Q_L + xQ_{G2}}{U_2\pi D_2 b_2 \tan\beta_2}\right\}\right]$$   *5*

Equation 5 shows that the mass weighted flow rates of the gas and liquid are required to ascertain the performance of the two-phase pump. Note that substituting $x$ = 0 into Eqn. 5 reduces it to the Euler turbomachinery equation for single-phase flow.

For Eqn. 5:

$$P_2 = P_1 + \Delta P$$     *6*

where, $\Delta P$ is the pressure boost (or pressure rise) provided by the pump. As defined previously,

$$GVF = \frac{Q_G}{Q_L + Q_G}$$     *7*

From the ideal gas equation,

$$Q_{G2} = \frac{m_G RT}{P_2} = \frac{m_G RT}{P_1 + \Delta P}$$     *8*

where, $m_G$ is the gas mass flow rate.

From Eqns. 2 and 3, and 5 to 8, it is evident that implicit computations are required to obtain $\Delta P$ for a given flow condition of gas and liquid.

Equation 5 may be rewritten in the form as shown in Eqn. 9:

$$\Psi^* = 1 - \Phi^*$$     *9*

where,

$\Psi^*$ = Dimensionless pressure difference per stage,

$$\left[\left(\frac{P_2}{\rho_{m2}U_2^2} - \frac{P_1}{\rho_{m1}U_2^2}\right) + x\frac{RT}{U_2^2}\ln\frac{P_2}{P_1}\right]$$   *10*

$\Phi^*$ = Dimensionless volume flow rate,

$$\frac{(1-x)Q_L + xQ_{G2}}{U_2\pi D_2 b_2 \tan\beta_2}$$     *11*

## Procedure

To obtain the $\Psi^*$ vs. $\Phi^*$ performance curves, multiphase test data available from open literature was used. It is assumed that the gas and liquid in these multiphase pumps are thoroughly mixed in accordance with good gas handling capabilities. It is also assumed that this well mixed fluid undergoes an isothermal process during the pumping process because of the significantly higher heat capacity of the liquid compared to the gas. The different steps of the procedure used in this study are presented next.

### Data Gathering

One of the data sets used was from the SVIP tests performed by Morrison et al. (2014)[5]. For this study, the data obtained was for rotational speeds of 3,000 rpm, 3,300 rpm, and 3,600 rpm for liquid flow rates at 15,000, 20,000, 25,000, 30,000, 35,000, 40,000, 45,000, and 50,000 bpd. The data was also obtained for pump intake pressures at 100 psig, 200 psig, and 300 psig, and intake GVFs of 0, 0.04, 0.08, 0.10, 0.15, 0.20, 0.25, 0.30, 0.35, 0.40, 0.45, 0.50, 0.55, and 0.57. In all, there were a total of 510 data points.

A second data set was obtained from the HAP tests by Patil et al. (2019)[4], using air and water (with a viscosity of 1 mPa-s) as the operating fluid. The available data was only at 200 psig intake pressure and for rotational speeds at 3,000 rpm and 3,600 rpm. The volume flow rate data obtained varied from 10,000 bpd to about 45,300 bpd, and the intake GVFs obtained were at 0, 0.15, 0.30, and 0.35. There was a total of 40 test data points.

No specific intake temperature was cited by Patil et al. (2019)[4]. Moreover, given that the fluid used was water with absolute viscosity of 1 mPa-s, the corresponding water temperature (from fluid tables) is approximately 20 °C (68 °F). From their tests, the liquid (water) temperature was maintained below 38 °C (100.4 °F). It can be assumed that the range of the test temperature was between 20 °C and 38 °C. For analysis in this study, the intake temperature may be taken as the average of this range, i.e., 29 °C (84.2 °F). The corresponding water density at this temperature is about 996 kg/m³.

The test temperature was not cited in the work by Morrison et al. (2014)[5]. To analyze the test data in this study[5], the intake temperature and water density will be taken as 29 °C (84.2 °F) and 996 kg/m³, respectively. Note that overall, due to the small percentage change in water density at the low range of pump test temperatures, the difference in liquid density does not affect the outcome of this work.

## Determining Rotor and Blade Dimensions
### Rotor OD

The HAP rotor's OD[4] was cited as equal to 6.693". The rotor's OD was not explicitly stated in Morrison et al. (2014)[5]. To estimate the OD, single-phase test data for an SVIP tested by Morrison et al. (2018)[7] was used. In one of the 3,600 rpm test data using water of 1 cP absolute viscosity, the head coefficient and head per stage were read off as 0.315 and 146.2 ft, respectively. From pump hydraulics, the corresponding rotor's OD was computed to be 7.781".

### Rotor Tip Blade Angle ($\beta_2$) and Rotor Tip Blade Height ($b_2$)

From Eqn. 11, knowledge of $\beta_2$ and $b_2$ is required to compute $\Phi^*$. These geometric parameters were not stated in the work by Patil et al. (2019)[4] and Morrison et al. (2014)[5], and the information is not available in the public domain. It was possible to compute the product $b_2 tan\beta_2$ for each multiphase pump. This term is constant for each pump since it is a geometric parameter specific to that pump design. To determine the magnitudes of $b_2 tan\beta_2$, single-phase (liquid only) data for each multiphase pump test was used. For single-phase, x = 0 (i.e., no gas) was substituted into Eqns. 10 and 11. Based on Eqn. 9, a graph of $\dfrac{P_2 - P_1}{\rho_L U_2^2}$ was plotted against $\dfrac{Q_L}{U_2 \pi D_2}$, with the former and latter terms as the dependent and independent variables, respectively. The graphs for each multiphase pump showed a negatively sloping linear line. The reciprocal of the slope of this line gave the term $b_2 tan\beta_2$. The corresponding magnitudes of $b_2 tan\beta_2$ for the SVIP and HAP were estimated as 0.04032 m and 0.01033 m, respectively.
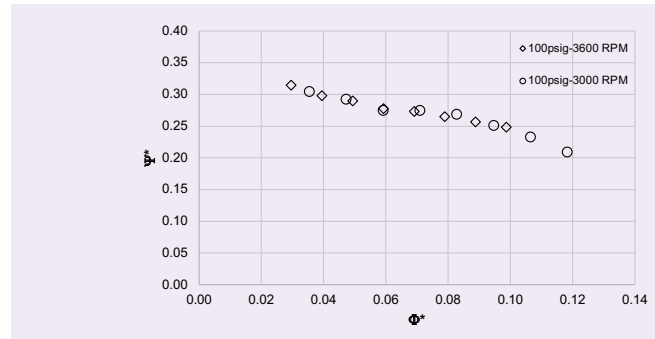
### Multiphase Pump Performance Curves

With the flow and geometric data obtained for both the SVIP and HAP, graphs of $\Psi^*$ vs. $\Phi^*$ were plotted using Eqns. 10 and 11. After comparing the plots for each multiphase pump, based on the data consistency, a representative performance curve for each multiphase pump was obtained using multiple linear regression analysis. The dependent variable was $\Psi^*$, and the independent variables were $\Phi^*$, $GVF_1$, and intake gas-liquid density ratio ($DR_1$). Here, $DR_1 = \dfrac{\rho_{G1}}{\rho_L} = \dfrac{P_1}{\rho_L RT}$, with $\rho_{G1}$ being the gas density at the pump intake.

For the SVIP, a data set at 3,000 rpm and 100 psig intake pressure, and a data set at 3,600 rpm and 300 psig intake pressure, were used to develop the representative performance curves. There was a total of 131 data points. The same procedure was performed for the HAP but using only the data at 3,000 rpm and 200 psig intake GVF, which were a total of 17 data points.

In all the analysis, the $p$-values of the regression coefficients were less than the required 5% significance level. This criterion indicated that the regression coefficients were not equal to zero, and were therefore statistically significant. The corresponding adjusted $R^2$ (coefficient of determination) were presented to show how much of the independent variables explains the change in the dependent variable. For both multiphase pumps, the performance curves were tested using the remaining test data (not used in obtaining the performance curve) to quantify how well the curves could estimate $\Psi^*$. The parameters used to ascertain this goodness of fit were the $R^2$ value and Root Mean Square Error (RMSE).
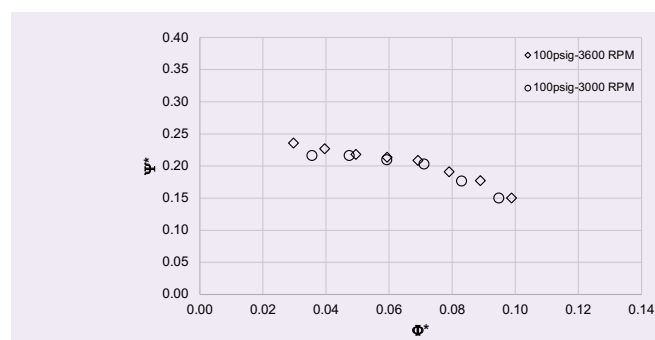
## Results
### SVIP — Multiphase Performance Curve Comparisons at 100 psig Intake

Figure 1 shows the variation of $\Psi^*$ vs. $\Phi^*$ for the liquid only test ($GVF_1 = 0$) at an intake pressure of 100 psig. Comparison is made for rotating speeds of 3,000 rpm and 3,600 rpm. The figure shows for each rotational speed, $\Psi^*$ decreases with increasing $\Phi^*$, which is typical of centrifugal machines. The trend is approximately linear. At 3,000 rpm, $\Psi^*$ decreases from about 0.30 to 0.21 with corresponding $\Phi^*$ from 0.04 to 0.12, respectively. For the 3,600 rpm data, the range of $\Psi^*$ was from 0.31 to 0.25, with corresponding $\Phi^*$ values of 0.03 to 0.10, respectively. The figure also shows that the plots for both operating speeds collapse on one another indicating that the pump obeys the classical pump scaling or affinity laws for single-phase flow.

Figure 2 shows data for $GVF_1 = 0.15$. The increase in



**Fig. 1** *The SVIP $\Psi^*$ vs. $\Phi^*$ plot at different speeds (intake pressure = 100 psig; $GVF_1 = 0$).*



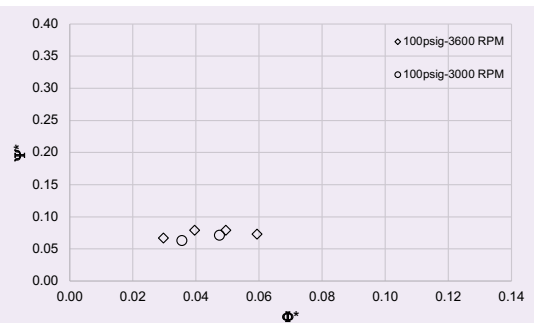**Fig. 2** *The SVIP $\Psi^*$ vs. $\Phi^*$ plot at different speeds (intake pressure = 100 psig; $GVF_1 = 0.15$).*

the amount of gas into the pump results in a decrease in $\Psi^*$ compared to the single-phase data $(GVF_1 = 0)$ in Fig. 1. The magnitude of $\Psi^*$ for the SVIP varied from approximately 0.24 to 0.15, for corresponding $\Phi^*$ of about 0.03 to 0.10, respectively. It is evident from the figure that the 3,000 rpm and 3,600 rpm data all still collapse on one another for $GVF_1 = 0.15$. This continues to indicate that the SVIP follows the affinity or scaling laws in accordance with the terms in Eqns. 10 and 11.

Figures 3, 4, and 5 show the results for $GVF_1$ of 0.30,

**Fig. 3** *The SVIP $\Psi^*$ vs. $\Phi^*$ plot at different speeds (intake pressure = 100 psig; $GVF_1 = 0.30$).*
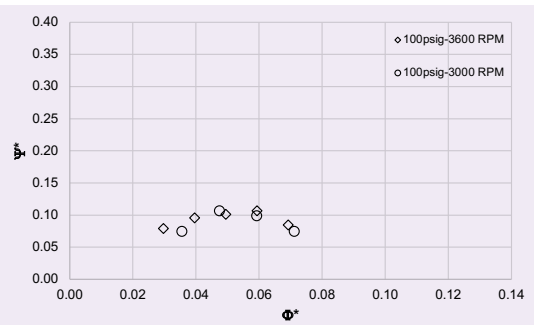


**Fig. 4** *The SVIP $\Psi^*$ vs. $\Phi^*$ plot at different speeds (intake pressure = 100 psig; $GVF_1 = 0.35$).*



**Fig. 5** *The SVIP $\Psi^*$ vs. $\Phi^*$ plot at different speeds (intake pressure = 100 psig; $GVF_1 = 0.45$).*
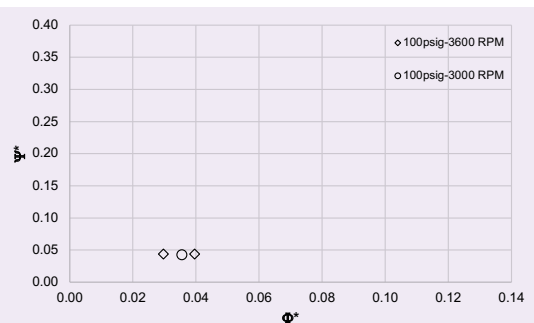


0.35 and 0.45, respectively. For each of the plots, $\Psi^*$ continues to decrease with increasing $GVF_1$. In addition, the range of $\Phi^*$ over which the SVIP can operate continues to decrease. For example, at $GVF_1 = 0.45$, $\Psi^*$ decreases to as low as 0.05 for $\Phi^*$ of about 0.03 to 0.04. This is more than six times less than the maximum value observed for the single-phase plot in Fig. 1.

The figures also show that for all these intake GVFs, the data at 3,000 rpm and 3,600 rpm all continue to collapse on one another. Therefore, for the entire intake GVF ranges from 0 to 0.45, which were the only available data for this study, the SVIP performance follows the scaling or affinity law using the terms in Eqns. 10 and 11. This was irrespective of the 3,000 rpm or 3,600 rpm rotational speed.

### SVIP — Multiphase Performance Curve Comparisons at 100 psig and 300 psig Intake Pressure

Figures 6 to 10 compare the plots of $\Psi^*$ vs. $\Phi^*$ at an intake pressure of 100 psig with those at an intake pressure of 300 psig for intake GVFs 0, 0.15, 0.30, 0.35, and 0.45. From Fig. 6, for $GVF_1 = 0$, the decreasing trend of $\Psi^*$ with increasing $\Phi^*$, is evident for the 300 psig intake pressure, similar to the plot in Fig. 1. There is a negligible difference in the magnitude of $\Psi^*$ for the same values of $\Phi^*$ for both intake pressures. Overall, the data for the 300 psig intake pressure for both rotational speeds shows the collapse on one another, similar to the data in Fig. 1.

Figure 7 shows the comparison at $GVF_1 = 0.15$. The plots for the intake pressure at 300 psig again collapse on one another. The magnitude of $\Psi^*$ at an intake pressure of 300 psig and $GVF_1 = 0.15$ were less than those of the same intake pressure and $GVF_1 = 0$, just as observed for the data at an intake pressure of 100 psig. There is, however, a difference in the magnitude of $\Psi^*$ between the intake pressures of 100 psig and 300 psig at the same rotational speed and the same range of $\Phi^*$. For example, at 3,600 rpm and an intake pressure of 300 psig, the range of $\Psi^*$ is from approximately 0.25 to 0.18. Subsequently, for the 3,600 rpm and 100 psig intake pressure, $\Psi^*$ varies from approximately 0.23 to 0.15. This plot indicates that for the same rotational speed and intake GVF, a higher intake pressure increases the magnitude of $\Psi^*$ for a given range of $\Phi^*$.

The $\Psi^*$ vs. $\Phi^*$ plots in Figs. 8 to 10 for the test data at an intake pressure of 300 psig all show similar comparison trends as previously discussed. The magnitude of $\Psi^*$ decreases as the intake GVF increases. The magnitude of $\Psi^*$ at $GVF_1 = 0.45$ was approximately 0.07 for the 300 psig intake pressure test compared to a maximum value of about 0.31 for the same intake pressure and $GVF_1 = 0$. This reduction was more than a factor of 4. In each case, the corresponding $\Psi^*$ for the tests at an intake pressure of 300 psig were higher than those for the 100 psig intake pressure. Overall, it shows that for a given rotational speed, intake GVF, and a range of $\Phi^*$, having a higher intake pressure increases the value of $\Psi^*$ from the pump. Furthermore, with the collapse of the test data on one another for the 300 psig intake pressure, the SVIP also follows the scaling or affinity laws using the terms in Eqns. 10 and 11.

**Fig. 6**  *The SVIP Ψ\* vs. Φ\* plot at different speeds and intake pressures (GVF₁ = 0).*
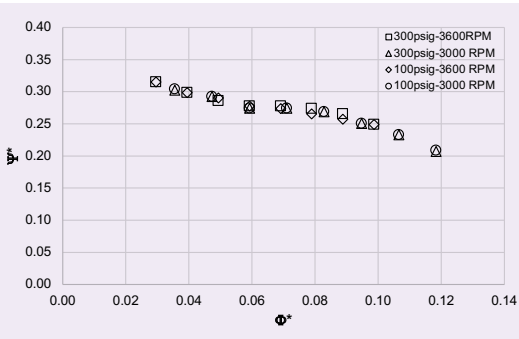


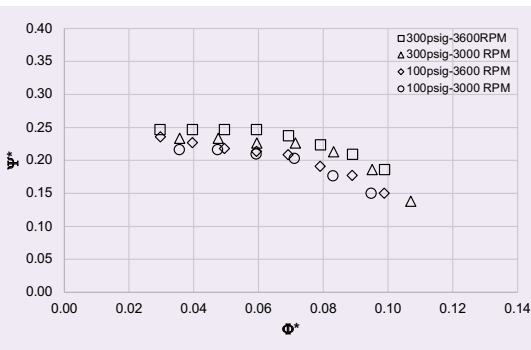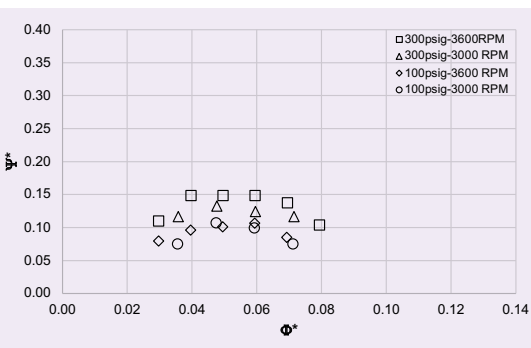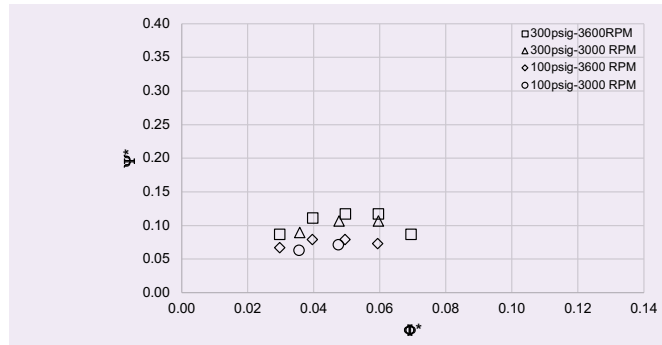**Fig. 7**  *The SVIP Ψ\* vs. Φ\* plot at different speeds and intake pressures (GVF₁ = 0.15).*



**Fig. 8**  *The SVIP Ψ\* vs. Φ\* plot at different speeds and intake pressures (GVF₁ = 0.30).*



**Fig. 9**  *The SVIP Ψ\* vs. Φ\* plot at different speeds and intake pressures (GVF₁ = 0.35).*



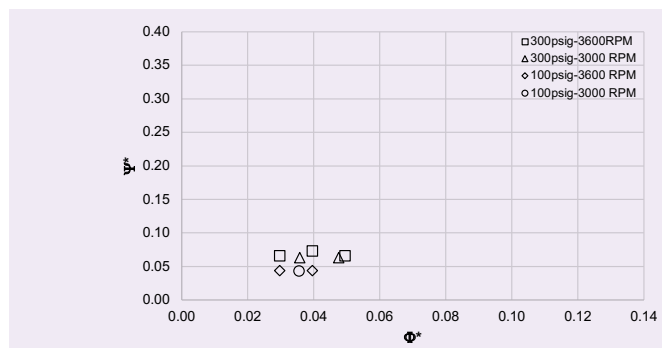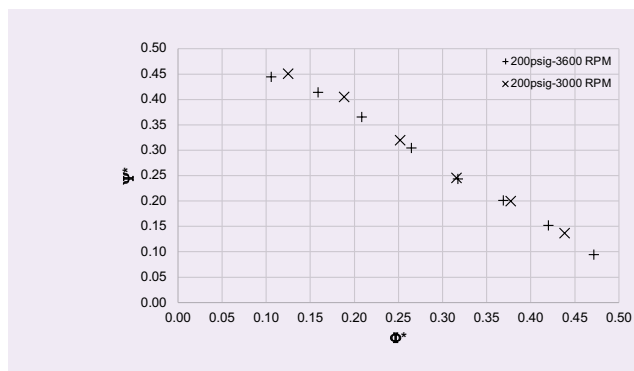**Fig. 10**  *The SVIP Ψ\* vs. Φ\* plot at different speeds and intake pressures (GVF₁ = 0.45).*



**Fig. 11**  *The HAP Ψ\* vs. Φ\* plot at different speeds (intake pressure = 200 psig; GVF₁ = 0).*



The data at 3,300 rpm, as well as the data at an intake pressure of 200 psig were not presented in this article for brevity. The same trends seen in the results previously discussed were also observed. Therefore, the scaling law behavior of the SVIP was consistent at rotational speeds of 3,000 rpm, 3,300 rpm, and 3,600 rpm, for each of the 100 psig, 200 psig, and 300 psig intake pressures and for the GVFs analyzed in this study.

## HAP — Multiphase Performance Curve Comparisons at 200 psig Intake Pressure

Figures 11 to 14 compares the plots of Ψ\* vs. Φ\* at an intake pressure of 200 psig for GVF₁ = 0, 0.15, 0.30, and 0.35 for the HAP. The data trend in Fig. 11 shows a nearly linear decrease in Ψ\* as Φ\* increases. This was also a similar trend for the SVIP at GVF₁ = 0. From Fig. 11, the range of Ψ\* was from 0.44 to 0.09 for the

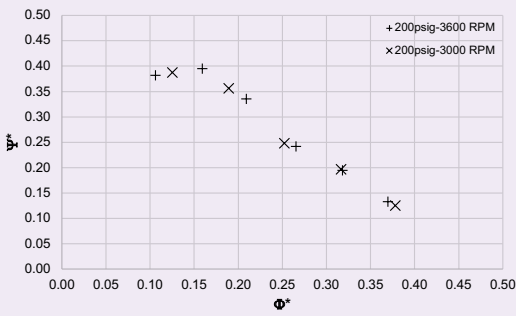**Fig. 12**  *The HAP Ψ\* vs. Φ\* plot at different speeds (intake pressure = 200 psig; GVF₁ = 0.15).*



**Fig. 13**  *The HAP Ψ\* vs. Φ\* plot at different speeds (intake pressure = 200 psig; GVF₁ = 0.30).*
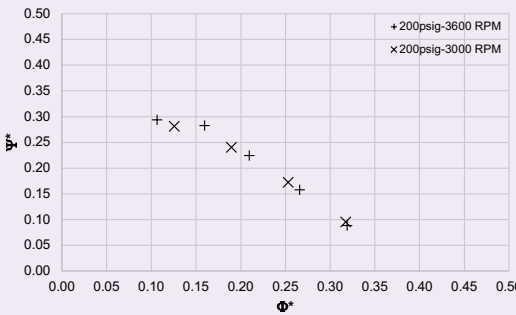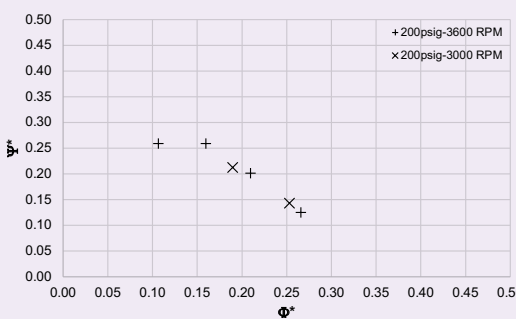


**Fig. 14**  *The HAP Ψ\* vs. Φ\* plot at different speeds (intake pressure = 200 psig; GVF₁ = 0.35).*



corresponding $\Phi^*$ range of 0.11 to 0.47. The collapsing of the test data for 3,000 rpm and 3,600 rpm at $GVF_1$ = 0 shows that the HAP obeys the scaling or affinity laws for single-phase flow (x = 0) in Eqns. 10 and 11.

Figure 12, for $GVF_1$ = 0.15, also shows a collapse of data for the rotating speeds of 3,000 rpm and 3,600 rpm. For the most part, $\Psi^*$ decreases linearly with an increasing $\Phi^*$. The maximum magnitude of $\Psi^*$ is about 0.40, which is less than the results of 0.44 obtained for $GVF_1$ = 0 in

Fig. 11. The decrease in the magnitude of $\Psi^*$ is due to the corresponding increase in $GVF_1$.

Figures 13 and 14 show a further decrease in the magnitude of $\Psi^*$. At $GVF_1$ = 0.30, the maximum value was approximately 0.30, and then decreases to about 0.26 at $GVF_1$ = 0.35. In this case, the reduction in the value of $\Psi^*$ was more than 1.5 times the value at $GVF_1$ = 0. Overall, for all the $GVF_1$, the data at rotational speeds of 3,000 rpm and 3,600 rpm all collapse on one another. This indicates that the HAP at an intake pressure of 200 psig also follows the scaling or affinity laws according to the terms in Eqns. 10 and 11.

### SVIP — Representative Performance Curve and Comparative Tests

From the SVIP results discussed previously, it was ascertained that for a given intake pressure and intake GVF, $\Psi^*$ varied with $\Phi^*$, and the test data all collapsed on one another irrespective of the rotational speed. This implies overall that $\Psi^*$ is a function of $\Phi^*$, $GVF_1$, and $P_1$. To capture the effect of intake pressure in a dimensionless form, requires using the $DR_1$ $(\frac{P_1}{\rho_L RT})$, as one of the independent variables.

As previously highlighted, multiple linear regression was applied on 131 data points consisting of the 100 psig-3,000 rpm, and 300 psig-3,600 rpm. The resulting performance equation obtained for the SVIP is presented in Eqn. 12, with the corresponding coefficients in Table 1.

$$\Psi^* = A + B(\Phi^*) + C(\Phi^*)^2 + D(GVF_1) + E(GVF_1)^2 + F(GVF_1)^3 + G(DR_1) + H(DR_1)^2 \qquad 12$$

The goodness of fit for Eqn. 12 showed that the adjusted $R^2$ value was 0.9794. To gauge the accuracy of Eqn. 12, it was tested using 379 SVIP test data points, which were not used in obtaining Eqn. 12.

The comparison is presented in Fig. 15, and shows that a high majority of the data estimated falls on the 45° sloping line. The $R^2$ value of the comparison plot was 0.9757, whereas the RMSE was 0.0118. Typically, the lower the RMSE value the better the equation is able to estimate the actual magnitude of a parameter. This indicates that the magnitude of $\Psi^*$ computed from Eqn. 12, matches well with the actual magnitudes of $\Psi^*$ obtained from the SVIP test. Therefore, Eqn. 12 is able to predict the $\Psi^*$ performance for the SVIP for the test conditions studied.

### HAP — Representative Performance Curve and Comparative Tests

A similar procedure as for the SVIP was also performed for the HAP data. Since the available test data from literature was only at one intake pressure, analysis to ascertain intake pressure effects could not be performed. For the HAP, multiple linear regression was applied on 17 data points from the 200 psig-3,000 rpm data set to obtain the performance curve for the range of flow conditions in the HAP tests. Equation 13 shows the relationship.

$$\Psi^* = 0.5863 - 1.0377\Phi^* - 3.6835(GVF_1)^2 + 6.3684(GVF_1)^3 \qquad 13$$

The goodness of fit for Eqn. 13 gave an adjusted $R^2$

**Table 1** *The regression coefficients from the SVIP data analysis.*

| A | B | C | D | E | F | G | H |
|---|---|---|---|---|---|---|---|
| 0.2694 | 1.2761 | -15.5848 | -0.2135 | -2.1310 | 3.0705 | -2.7020 | 129.6344 |

value of 0.9861. Equation 13 was tested using 23 actual data points from the HAP test operating at 3,600 rpm. These data were not used to develop Eqn. 13.

Figure 16 shows the comparison plots, which also indicate that a high majority of the estimated data fall on the 45° sloping line. The corresponding $R^2$ value for the comparison plot was 0.9686, with a RMSE of 0.0184. This implies that Eqn. 13 is able to predict the performance of the HAP for the test conditions studied.

**Field Application of the Representative Performance Curves**

Application of either Eqns. 12 and/or 13 to determine $\Delta P (= P_2 - P_1)$ in field operations is highlighted here for the benefit of operators or asset stakeholders. The basic steps are as follows for a given $D_2$ and $b_2 tan\beta_2$ of a specific multiphase pump.

Step 1: Determine flow parameters $Q_1, \rho_L, m_G, P_1, T$, and $R$ and operating rotational speed, $N$.

Step 2: Select an initial $\Delta P$ value.

Step 3: Compute $x$, $\rho_{G1}$, $\rho_{G2}$, $Q_{G1}$, $Q_{G2}$, $\rho_{m1}$, $\rho_{m2}$, $GVF_1$, $GVF_2$, $U_2$, $DR_1$, $\Phi^*$, and $\Psi^*$.

Step 4: Substitute the required dimensionless parameters into Eqns. 12 or 13.

Step 5: Compare magnitudes of the left-hand side and right-hand side of Eqns. 12 or 13. If different, return to Step 2 and increase or decrease $\Delta P$.

Step 6: (as required): Repeat Steps 3 to 5, until the magnitudes of the left-hand side and right-hand side of Eqns. 12 or 13 are equal. The corresponding value of $\Delta P$ when this condition is met is the pressure boost of the multiphase pump for the flow conditions being analyzed.

An alternate computation of dimensionless pressure difference and dimensionless flow parameters may also be used to arrive at the main objective of this work. This is presented in the Appendix for brevity.

## Summary and Conclusions

This study was about applying the Euler turbomachinery equation to obtain the performance characteristics of multiphase pumps. Test data for an SVIP and HAP obtained from literature were used to test the effectiveness of the performance relationship. The range of test conditions were intake pressures of 100 psig to 300 psig, 0 to 0.57 intake GVF, rotational speeds of 3,000 rpm to 3,600 rpm, and a liquid volume flow rate of 10,000 bpd to 50,000 bpd.

The results showed that for the dimensionless pressure difference and mass weighted dimensionless flow parameters used, given intake pressure and intake GVF, the data

**Fig. 15** *Comparing the actual and the calculated Ψ\* using SVIP test data.*
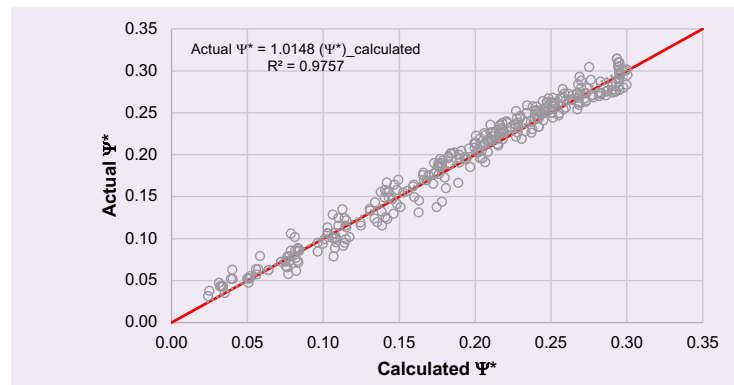


**Fig. 16** *Comparing the actual and the calculated Ψ\* using HAP test data.*
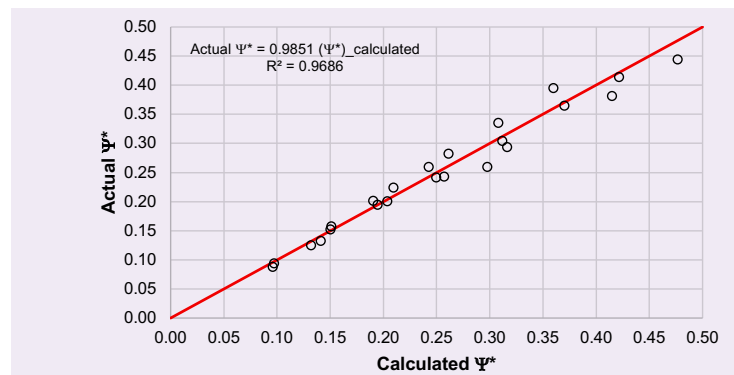


points for the different speeds collapsed on one another. This indicated that the performance of the multiphase pumps matches the scaling or affinity law based on the dimensionless terms presented in this study. The data also showed that for a given rotational speed, intake GVF and range of mass weighted dimensionless flow rates, higher intake pressures resulted in a higher dimensionless pressure difference from the multiphase pumps.

Based on the consistent trend and data collapse in the dimensionless parameters, a performance equation was developed for the SVIP and HAP by performing multiple linear regression analysis. The dimensionless pressure difference was a function of the dimensionless volume flow rate, intake GVF, and intake DR. The performance equations had a high goodness of fit with adjusted $R^2$ values of 0.9794 and 0.9861 for the SVIP and HAP

equations, respectively.

After obtaining the performance equation for each multiphase pump, the equations were tested by comparing the computed dimensionless pressure difference with those from actual test data. About 379 test data points were used for the comparison for SVIP, and 23 test data points were used for the HAP. In all, the computed dimensionless pressure difference matched up well with the dimensionless pressure difference from the actual test. The $R^2$ value and RMSE of the comparison plots for the SVIP was 0.9757 and 0.0118, respectively. The corresponding values for the HAP were 0.9686 and 0.0184, respectively.

Finally, a step-by-step procedure of using the performance equations for the multiphase pumps was presented. It required performing iterative computations, to determine the pressure boost of the multiphase pump for any given flow condition. This is because the pump discharge pressure is an implicit function of the gas volume flow rate and the dimensionless pressure difference developed by the pump.

Using dimensional analysis to obtain performance relationships for multiphase pumps is important in field operations. It may be used to determine different operating conditions of the pump for a given set of pump operating parameters. A further advantage of dimensionless parameters is that it helps to understand the different parameters that may be optimized during design to improve the pumping operation. Overall, these benefit the stakeholders of the field asset, facilitates efficient production from high gas content wells, and increases the economic bottom line for the operator.

## Acknowledgments

## References

1. Hua, G., Falcone, G., Teodoriu, C. and Morrison, G.L.: "Comparison of Multiphase Pumping Technologies for Subsea and Downhole Applications," *Oil and Gas Facilities*, Vol. 1, Issue 1, February 2012, pp. 36-46.

2. Timar, P.: "Dimensionless Characteristics of Centrifugal Pump," *Chemical Papers – Slovak Academy of Sciences*, Vol. 59, Issue 6b, January 2005, pp. 500-503.

3. Douglas, J.F., Gasiorek, J.M. and Swaffield, J.A.: *Fluid Mechanics*, 3rd edition, Singapore: Longman, 1995, 642 p.

4. Patil, A., Gudigopuram, S., Ayyildiz, B.C., Delgado, A., et al.: "Performance Evaluation and Dimensional Analysis of Multistage Helicoaxial Pump for Two-Phase Flow," *International Journal of Turbomachinery Propulsion and Power*, Vol. 4, Issue 3, July 2019, pp. 22-36.

5. Morrison, G., Pirouspanah, S., Kirland, K., Scott, S.L., et al.: "Performance Evaluation of a Multiphase Electric Submersible Pump," OTC paper 25080, presented at the Offshore Technology Conference, Houston, Texas, May 5-8, 2014.

6. Poullikkas, A.: "Two Phase Flow and Cavitation in Centrifugal Pump: A Theoretical and Experimental Investigation," M.S. thesis, Loughborough University, Loughborough, Leicestershire, 1992.

7. Morrison, G., Yin, W., Agarwal, R. and Patil, A.: "Development of Modified Affinity Law for Centrifugal Pump to Predict the Effect of Viscosity," *Journal of Energy Resources Technology*, Vol. 140, Issue 9, September 2018.

## Nomenclature

$b$ = Rotor blade height, L, m

$D$ = Rotor diameter, L, m

$g$ = Acceleration due to gravity, m/t$^2$, m/s$^2$

$H$ = Head, L, m

$m$ = Mass flow rate, m/t, kg/s

$N$ = Rotational speed (rpm), 1/s

$P$ = Absolute mixture pressure, m/Lt$^2$, Pa

$Q$ = Volume flow rate, L$^3$/t, m$^3$/s

$R$ = Characteristic gas constant, L$^2$/t$^2$T, J/kg K

$T$ = Absolute gas temperature, K

$U$ = Rotor peripheral speed, L/t, m/s

$V$ = Velocity, L/t, m/s

$x$ = Mixture quality

$\beta$ = Rotor blade angle (°)

$\Delta P$ = Differential pressure, m/Lt$^2$, Pa

$\Phi^*$ = Dimensionless volume flow rate

$\rho$ = Density, m/L$^3$, kg/m$^3$

$\Psi^*$ = Dimensionless pressure difference per stage

## Subscripts

$E$ = Euler

$G$ = Gas phase

$L$ = Liquid phase

m = Mixture

1 = Intake

2 = Discharge

2ph = Two-Phase

# Appendix

All terms presented are as defined in the main article. It was stated previously that:

$\Psi^*$ = Dimensionless Pressure Difference per stage,

$$\left[\left(\frac{P_2}{\rho_{m2}U_2^2} - \frac{P_1}{\rho_{m1}U_2^2}\right) + x\frac{RT}{U_2^2}\ln\frac{P_2}{P_1}\right] \qquad A1$$

$\Phi^*$ = Dimensionless volume flow rate,

$$\frac{(1-x)Q_L + xQ_{G2}}{U_2\pi D_2 b_2 \tan\beta_2} \qquad A2$$

The following definition was presented for the rotor peripheral speed, $U$:

$$U = \left(\frac{D}{2}\frac{2\pi N}{60}\right) \qquad A3$$

Substituting Eqn. A3 into Eqns. A1 and A2, assuming geometrically similar machines, collecting constant terms and simplifying gives the following terms:

$$(\Psi^*)' = \frac{\left[\left(\frac{P_2}{\rho_{m2}} - \frac{P_1}{\rho_{m1}}\right) + xRT\ln\frac{P_2}{P_1}\right]}{N^2 D_2^2} \qquad A4$$

$$(\Phi^*)' = \frac{(1-x)Q_L + xQ_{G2}}{ND_2^3} \qquad A5$$

For a given multiphase pump, $D_2$ is constant. Equations A4 and A5 reduce to:

$$(\Psi^*)'' = \frac{\left[\left(\frac{P_2}{\rho_{m2}} - \frac{P_1}{\rho_{m1}}\right) + xRT\ln\frac{P_2}{P_1}\right]}{N^2} \qquad A6$$

$$(\Phi^*)'' = \frac{(1-x)Q_L + xQ_{G2}}{N} \qquad A7$$

Equations A8 to A12 can be used to substitute into Eqns. A4, A5, A6, or A7:

$$P_2 = P_1 + \Delta P \qquad A8$$

$$\rho_{m1} = (1 - GVF_1)\rho_L + GVF_1\frac{P_1}{RT} \qquad A9$$

$$\rho_{m2} = (1 - GVF_2)\rho_L + GVF_2\frac{P_2}{RT} \qquad A10$$

$$GVF = \frac{Q_G}{Q_L + Q_G} \qquad A11$$

$$Q_{G2} = \frac{m_G RT}{P_2} = \frac{m_G RT}{P_1 + \Delta P} \qquad A12$$

Graphs of $(\Psi^*)''$ vs. $(\Phi^*)''$ may be plotted for different intake GVFs and intake pressures. A set of performance curves, similar to Eqns. 12 and 13 in the main article, can be obtained, but with different regression coefficients. The step-by-step procedure highlighted in the main article can also be applied to these new sets of performance equations. Estimating $\Delta P$ requires the field engineer to only enter flow/operating parameters without needing to know the $D_2$ and $b_2 \tan\beta_2$ of the specific multiphase pump.

---

**About the Author**

**Dr. Chidirim E. Ejim**

*Ph.D. in Mechanical Engineering, University of Alberta*

Dr. Chidirim E. Ejim is a Petroleum Engineering Specialist working in the artificial lift focus area within the Production Technology Division of Saudi Aramco's Exploration and Petroleum Engineering Center – Advanced Research Center (EXPEC ARC). Prior to joining Saudi Aramco in 2014, Chidirim spent over 7 years with Schlumberger's Artificial Lift Segment, working on surface horizontal pumping systems; downhole pump design, development and testing; multi-phase production systems; as well as downhole gas separator/gas handler testing and analysis.

He received his B.Eng. degree (Honors) from the University of Malta, Msida, Malta; his M.S. degree from the University of Waterloo, Ontario, Canada; and his Ph.D. degree from the University of Alberta, Edmonton, Canada, all in Mechanical Engineering.

Chidirim is a Registered Professional Engineer in Alberta, Canada.